UNIVERSITÀ DEGLI STUDI DI PADOVA

Sede Amministrativa: Università degli Studi di Padova
Dipartimento di Ingegneria Industriale

SCUOLA DI DOTTORATO DI RICERCA IN: Scienze, Tecnologie e Misure Spaziali

INDIRIZZO: Scienze e Tecnologie per Applicazioni Satellitari e Aeronautiche (STASA)
XXX CICLO

On the coupling of peridynamics with the classical theory of continuum mechanics in a meshless framework

Direttore della Scuola: *Ch.mo Prof. Giampiero Naletto*
Coordinatore d'indirizzo: *Ch.mo Prof. Giampiero Naletto*

Supervisore: *Ch.mo Prof. Ugo Galvanetto*
Co-Supervisore: *Ch.mo Prof. Mirco Zaccariotto*

Dottorando: *Arman Shojaei Barjoui*

To my parents,

without whom none of my success would be possible

SUMMARY

The classical theory of solid mechanics employs partial derivatives in the equation of motion and hence requires the differentiability of the displacement field. Such an assumption breaks down when simulation of problems containing discontinuities, such as cracks, comes into the picture. peridynamics is considered to be an alternative and promising nonlocal theory of solid mechanics that is formulated suitably for discontinuous problems. Peridynamics is well designed to cope with failure analysis as the theory deals with integral equations rather than partial differential equations. Indeed, peridynamics defines the equation of motion by substituting the divergence of the stress tensor, involved in the formulation of the classical theory, with an integral operator. One of the most common techniques to discretize and implement the theory is based on a meshless approach. However, the method is computationally more expensive than some meshless methods based on the classical theory. This originates from the fact that in peridynamics, similar to other nonlocal theories, each computational node interacts with many neighbors over a finite region. To this end, performing realistic numerical simulations with peridynamics entails a vast amount of computational resources. Moreover, the application of boundary conditions in peridynamics is nonlocal and hence it is more challenging than the application of boundary conditions adopted by methods based on the classical continuum theory. This issue is well-known to scientists working on peridynamics.

Therefore, it is reasonable to couple computational methods based on classical continuum mechanics with others based on peridynamics to develop an approach that applies different computational techniques where they are most suited for. The main purpose of

this dissertation is to develop an effective coupled nonlocal/local meshless technique for the solution of two-dimensional elastodynamic problems involving brittle crack propagation. This method is based on a coupling between the peridynamic meshless method, and other meshless methods based on the classical continuum theory. In this study, two different meshless methods, the Meshless Local Exponential Basis Functions and the Finite Point Method are chosen as both are classified within the category of strong form meshless methods, which are simple and computationally cheap. The coupling has been achieved in a completely meshless scheme. The domain is divided in three zones: one in which only peridynamics is applied, one in which only the meshless method is applied and a transition zone where a transition between the two approaches takes place. The coupling adopts a local/nonlocal framework that benefits from the full advantages of both methods while overcoming their limitations. The parts of the domain where cracks either exist or are likely to propagate are described by peridynamics; the remaining part of the domain is described by the meshless method that requires less computational effort. We shall show that the proposed approach is suited for adaptive coupling of the strategies in the solution of crack propagation problems. Several static and dynamic examples are performed to demonstrate the capabilities of the proposed approach.

ACKNOWLEDGEMENTS

Firstly, I would like to express my sincere gratitude to my supervisor Prof. Ugo Galvanetto and my co-supervisor Prof. Mirco Zaccariotto for the continuous support of my Ph.D study and related research, for their patience, motivation, and immense knowledge. Their guidance helped me in all the time of research and writing of this thesis. I could not have imagined having a better advisor and mentor for my Ph.D study.

I am deeply grateful to Prof. Timon Rabczuk for giving me the possibility to spend six months in his research group at Bauhaus University Werimar, Germany, and for his brilliant comments and suggestions on my work.

I must express my gratitude to Prof. Farshid Mossaiby for his useful suggestions especially during his stay here in Italy. His helps played a key role in some parts of my research.

A special thanks to Prof. Pablo Seleson and Prof. Erkan Oterkus for their time and effort in reviewing the dissertation and their useful suggestions.

A special thanks to my family. Words cannot express how grateful I am to my father, mother, and my brother for all of the sacrifices that they have made on my behalf. They have regularly encouraged me to believe in myself.

I would also like to thank all of my friends Giulia, Angela, Daniele, Teo, Soheil, Milad and Siavash who supported me in writing, and incented me to strive towards my goal.

Finally, I would like to thank the University of Padua, not only for providing the funding which allowed me to undertake this research, but also for giving me the opportunity to attend conferences and meet so many interesting people.

PUBLICATIONS

Articles:

- Zaccariotto, M., Mudric, T., Tomasi, D., Shojaei, A. and Galvanetto, U., 2018. Coupling of FEM meshes with Peridynamic grids. Computer Methods in Applied Mechanics and Engineering, 330, pp.471-497.

- Shojaei, A.,Zaccariotto, M. and Galvanetto, U., 2017. Coupling of 2D discretized Peridynamics with a meshless method based on classical elasticity using switching of nodal behaviour.Engineering Computations, 34(5), 1334-1366.

- Shojaei, A., Mudric, T., Zaccariotto, M. and Galvanetto, U., 2016. A coupled meshless finite point/Peridynamic method for 2D dynamic fracture analysis. International Journal of Mechanical Sciences, 119, pp.419-431.

- Galvanetto, U., Mudric, T., Shojaei, A. and Zaccariotto, M., 2016. An effective way to couple FEM meshes and Peridynamics grids for the solution of static equilibrium problems. Mechanics Research Communications, 76, pp.41-47.

- Shojaei, A., Mossaiby, F., Zaccariotto, M. and Galvanetto, U., 2017. The meshless finite point method for transient elastodynamic problems. Acta Mechanica, 228(10), pp.3581-3593.

- Mossaiby, F., Shojaei, A., Zaccariotto, M. and Galvanetto, U., 2017. OpenCL implementation of a high performance 3D Peridynamic model on graphics accelerators. Computers & Mathematics with Applications, 74(8), pp.1856-1870.

- Zaccariotto, M., Sarego, G., Dipasquale, D., Shojaei, B. Bazazzadeh, A., Mudric, T., Duzzi, M. and Galvanetto, Discontinuous mechanical problems studied with a peridynamics-based approach, Aerotecnica Missili & Spazio, The Journal of Aerospace Science, Technology and Systems (2017), In press.

Proceedings:

- Shojaei, A., Zaccariotto, M. and Ugo Galvanetto. On the Coupling of Peridynamics With a Meshless Method Based on Classical Elasticity. ASME 2016 International Mechanical Engineering Congress and Exposition. American Society of Mechanical Engineers, Phoenix, Arizona, USA.

- Zaccariotto, M., Sarego, G., Dipasquale D., Shojaei, A., Mudric T., Duzzi M. and Galvanetto U. Discontinuous mechanical problems studied with a peridynamics-based approach, AIDAA2015, Italy, 2015.

- Shojaei, A., Mossaiby, F., Zaccariotto, M. and Galvanetto, U. An extended finite point method for problems with singularities, International Conference on Boundary Element and Meshless Techniques, Spain, 2015.

Abstract:

- Shojaei A., Zaccariotto M. and Galvanetto, U. A hybrid nonlocal-local meshless approach for dynamic crack propagation, 16th International Conference on New Trends in Fatigue and Fracture (NT2F16), Croatia, 2016.

- Dipasquale D., Sarego G., Shojaei A., Zaccariotto, M. and Galvanetto, U. Addressing grid sensitivity in Peridynamics: an adaptive refinement approach, CFRAC 2015, France, 2015.

- Galvanetto U., Zaccariotto M., Mudric T., Shojaei A., Bazazzadeh S. and Tomasi D. A Simple Way to Couple Peridynamic Grids to FEM meshes for the Solution of Static Problems, IMECE2016, International Mechanical Engineering Congress and Exposition, Phoenix, Arizona, USA, 2016.

Awards:

- Author winner of 2015 A.I.D.A.A. “Premio in memoria del Prof. Teodoro Merlini” prize for best paper in XXIII AIDAA Conference in Turin, Italy, 17-19 November 2015.

CONTENTS

LIST OF FIGURES

LIST OF TABLES

1. Introduction

In this chapter, a brief review on the literature of different subjects, related to the main goals of the present dissertation, is presented. Then, the merits and difficulties of several major approaches, in particular those aimed at modelling brittle fracture phenomena, are discussed.

1.1 Failure analysis in the framework of the classical local theory

Accurate modeling of damage and fracture phenomena is still an open issue for the community of computational mechanics [1]. Failure analysis is one of the most challenging problems when it is modeled in the frame-work of the classical theory of mechanics.

Many different concepts have so far been developed in the literature for prediction of crack initiation and growth in materials. However, the main difficulty is originated in the mathematical formulation on which the classical continuum mechanics is based. The theory assumes that as a body deforms it remains continuous; therefore, it becomes undefined whenever a discontinuity appears in the body. From a mathematical point of view, the classical continuum theory is formulated based on partial differential equations, yet spatial derivatives lose their meaning when a discontinuity (singularity), such as a crack, exists in a body.

Solution of the state of stress at crack tips, in the framework of the classical theory, results in infinite (or singular) stresses. This conclusion was obtained in the early studies

of Griffith [2], and it underpinned the concept of Linear Elastic Fracture Mechanics (LEFM). On the basis of LEFM, the presence of a pre-existing crack is essential to consider crack initiation and growth in a material. Furthermore, it adds additional criteria to the theory, such as a critical energy release rate, to equip the theory for the solution of crack propagation problems. However, simulation of important phenomena such as nucleation of crack requires special/ad hoc criteria in LEFM.

In LEFM, accurate calculation of the added criteria, such as stress intensity factor, are highly dependent on the mechanical and geometrical properties as well as the numerical solution method. As a consequence, failure analysis along with consideration of other complex issues such as, dislocations, presence of micro cracks, and anisotropy within LEFM is extremely difficult.

Despite the fact that the classical theory is incapable of distinguishing among different length scales, due to its local nature, it can still be applied to a wide range of engineering problems. Simulation of a certain failure processes by applying the Finite Element Method (FEM) as the numerical solution is achievable by the classical theory.

FEM is the most popular computational technique for structural computations. It is robust and has been thoroughly developed for static, dynamic, linear and nonlinear mechanical systems. However, modeling of problems with evolving discontinuities by the conventional FEM is a challenge, and special techniques have to be devised. This originates again from the continuum theory from which the governing equations of FEM are derived. Therefore, FEM suffers from the presence of undefined spatial derivatives at crack tips and along the crack surface.

Adoption of LEFM into the FEM requires introduction of particular elements to capture the singular behavior at the crack tip correctly; of course such a treatment contributes to imposition of mathematical artifacts in a model. In the traditional FEM, a crack is defined as a boundary with free traction. As a result, solving problems with crack propagation requires the redefinition of the body in time.

One of the main viable options to cope with moving cracks in a simulation using FEM is to update the mesh during each step of analysis in such a way that the element edges coincide with the cracks during all steps. Even though re-meshing approaches have so far been developed to address these limitations, for instance in [3], they are often applicable only to 2D cases. Moreover, such remeshing processes are affected by numerical difficulties, complexity in computer programing and often lead to degradation of solution accuracy [4].

With the aim of eliminating remeshing techniques, over the past decades, meshless methods have attracted the attention of many researchers. Unlike conventional FEM, in meshless methods the adaptive scheme can be easily developed as there is no mesh and thus no so called *a priory* connectivity is required between the nodes. This fact culminates in providing a flexible computational tool and, particularly in the case of crack propagation, the burdensome remeshing required by conventional FEM models is avoided. Fundamentally in meshless methods, only a scattered set of nodal points is required, not necessarily a structured mesh, to represent the domain of interest. In the case of stress analysis in solid mechanics, there are often areas of stress concentration. One may conveniently add nodes in the stress concentration area without worrying about their relationship with other nodes. Such an appealing feature presents significant

implications for modeling crack propagation. A variety of meshless methods have been proposed by researchers; for instance, references [5]–[8].

Despite the progress made in developing meshless methods, the aforementioned difficulties again emerge because their governing equations are derived from the classical theory [9]. Therefore, any numerical method (both meshless or mesh-based) based on the classical theory inherits this difficulty for modeling singular problems as well as crack propagation. They also require additional relations that govern the initiation of the crack, their direction and their growth velocity. These kinetic relations must be provided for the analysis to determine when a crack should initiate, how fast a crack should propagate, when it should turn, branch, oscillate, etc. To recap, by using the conventional methods it is very problematic to solve problems which include multiple crack interactions, and those which deal with crack propagation in a complex manner.

1.1.1 Remedies and numerical methods

Significant efforts have been made by the studies documented in the literature to improve the shortcomings of traditional FEM within the realm of LEFM. Ad-hoc modifications have been added to different classical models to equip them with necessary tools for handling crack propagation.

The cohesive finite element method uses the cohesive zone model (cohesive law) applied to finite elements. The concept of cohesive zone was introduced by Dugadle [10] and Barenblatt [11], and the introduction of cohesive zone elements for application to FEM models was done in [12], [13]. Cohesive zone elements are usually placed between continuum elements. The cohesive zone elements can open whenever a damage growth takes place, including initiation and propagation of crack. In this approach, a prior

knowledge of actual crack path is necessary; since in the simulation, crack can only propagate in the parts where cohesive zone elements are placed. However, usually advanced knowledge of crack path in practice is not available, due to the complexity of the problem, is not available. Mesh dependency is another important issue which restricts the use of cohesive zone FEM models [14].

The eXtended finite element method (XFEM) was developed in an effort to address the difficulties of the cohesive zone element models. XFEM was introduced as a technique to model crack growth without any sort of remeshing [15]. XFEM adds enrichment functions (i.e., additional degrees of freedom) to the approximation which are singular, and they contain a discontinuous displacement field. Such a treatment, allows cracks to pass through elements rather than along the element boundaries, and hence solves the problem of mesh dependency. It is remarkable that XFEM has so far been employed to analyze dynamic propagation of cracks as in [16]. On the other hand, for the sake of integration, subdivision of the cut elements contributes to complexity and an increasing computational cost [17]. In addition, branching and phenomenological damage criteria are still required in XFEM. In the case of fragmentation and when a couple of cracks start developing in the material XFEM might not be an option. In conclusion, XFEM cannot cope with problems in which multiple interaction of cracks is of concern. Moreover, its use in 3D problems turns out to be very cumbersome [18].

More recently, the phase field theory [19] has received a widespread attention by the scientists. It has the ability of predicting spontaneous emergence and propagation of cracks. In this method, cracks are represented using an additional scalar field variable called phase field which is used to distinguish between damaged and undamaged parts of

the solution domain. The evolution equation of the phase field is coupled with the governing momentum balance equations in the classical continuum mechanics. Hence the solution of a coupled system of PDEs computes displacements, stresses and phase field parameters. However, gradients/divergence terms in the governing equation of the phase field could be a source of inconsistency with the onset of material discontinuity [20].

The difficulties which arise from computational models utilizing the classical continuum mechanics can be overcome by performing molecular dynamics simulations or atomistic lattice studies. One of the most realistic and detailed models for the investigation of material fracture is atomistic simulation [21]. Some important features of dynamic fracture based on atomistic simulations are explained in [22]. In this way, by using inter-atomic forces crack initiation and propagation can be modeled. Molecular dynamic models have the capability of reproducing some phenomena observed in experiments (see [23], [24]). In the past decades, the large scale problems that could be modeled by researchers using molecular dynamics were restricted to about one billion atoms [25], [26]. This originated from a limitation in computational resources. More recently, due to advancements in computer architectures simulation of larger scale problems with molecular dynamic is possible. Molecular dynamic models can be performed with 19 billion atoms [27]. However, there are two important issues about molecular dynamics which have not been addressed yet. Firstly, modelling the original geometry of a real problem is too difficult as the length scale is too small. Secondly, the time scales are very small too. To overcome such a difficulty, one way is to accelerate the simulation by using load conditions of higher rate in comparison to those seen in practice. An important conclusion is that atomistic studies are more suitable for fundamental understanding of

the physical process of fracture rather than being used for dynamic crack prediction and failure analysis [28].

1.2 Peridynamics

Recently, in order to overcome the restrictions related to the differential formulation of methods based on the classical theory as well as nonlocal theories developed in the past, the peridynamics nonlocal theory has been proposed by Silling [29] and Silling et al. [30]. Peridynamics is considered to be an alternative and promising nonlocal theory of solid mechanics that is formulated suitably for discontinuous problems such as crack propagation. peridynamics is well designed to cope with failure analysis as the theory deals with integral equations rather than spatial differentiation. peridynamics defines the equation of motion by substituting the divergence of the stress tensor, involved in the formulation of the classical theory, with an integral operator. These equations are valid even in the presence of discontinuities in the displacement field. Since damage and material failure are invoked through the material response in peridynamics, fracture occurs as a natural result of the equation of motion and constitutive models. The peridynamic governing equations are defined at crack surfaces and there is no longer a need to use special numerical techniques such as interface elements and singular basis functions to treat fracture. Another important feature of peridynamics is the introduction of a length parameter, the so called horizon. The horizon is a definition introduced in the formulation of peridynamics, and it specifies the size of the region where nonlocal interactions of a material point with other points take place. The horizon length can be linked to a characteristic length-scale of the material and the considered phenomenon

[31]. In this way, it is feasible to investigate the material response at different length scales, from macroscale to nanoscale, as the horizon size can be controlled.

Peridynamic models can easily predict crack nucleation, multiple branching, and propagation. The first introduced and most commonly used peridynamic formulation, in the case of failure analysis, is the bond-based peridynamic formulation. The main concept proposed by Silling is the assumption that material points can interact with each other provided that they are located inside a finite region. Indeed, due to this concept, the Greek roots of the words *near* and *force* were proposed to call this theory "*peridynamics*".

It is worth noting that the theory has already been applied in a meshless style for the modeling of impact damage [32] and for brittle dynamic crack growth [33], [34] that reproduces well the crack path experimentally observed in brittle materials. Thanks to these features, peridynamics has attracted widespread interest among researchers, and the number of studies on the application of the method to different challenging applications is growing fast; see for instance [35]–[45] and the references cited in [46].

1.3 Outlines of the present study

In spite of all the appealing features of peridynamic models, they are most often computationally much more expensive than the methods based on the classical theory of mechanics such as the finite element method (FEM). Moreover, capturing more realistic numerical solutions with peridynamics which resemble experimental observation entails a vast amount of computational resources [47]. In general, simulation of fully nonlocal models is computationally much more expensive than that based on the classical (local)

continuum mechanics. This originates from the fact that in nonlocal theories each integration point interacts with many neighbors. Consequently, the meshless methods based on peridynamics are computationally more expensive than the majority of meshless methods based on the classical theory.

It is therefore reasonable to couple computational methods based on classical continuum mechanics with others based on peridynamics to develop an approach that applies different computational techniques where they are most suited for. The challenge is *gluing* these two different models with an efficient and simple technique without introducing numerical artifacts. That is the main objective of the present dissertation.

Several studies have been conducted by many researchers to reach a suitable nonlocal-local continuum coupling. For instance, Han and Lubineau [48] proposed an approach based on the Arlequin method in which the coupling conditions are enforced by the introduction of Lagrange multipliers, but in this way the size of the system to be solved largely increases. Seleson et al. [49] introduced a force conservation technique in one dimension, and then the work was extended to higher dimensions in [50]. Lubineau et al. [51] developed the morphing method based on the conservation of the strain energy density over the overlapping coupling region, and then the method was applied to static fracture problems in [52]. Agwai et al. [53] used the submodeling approach for the sake of coupling peridynamics with FEM. In their approach, first the global analysis is performed by FEM, and then peridynamics is employed for submodeling.

In the literature one can find some studies regarding *concurrent* coupling of peridynamics with FEM. Macek and Silling [54] implemented the peridynamic model in the framework of conventional FEM using truss elements. In their work the FEM mesh is coupled with a

peridynamic truss mesh by using embedded elements. In the overlapping region, the elastic modulus of the host elements must be tuned to very small values to avoid excessive stiffness. On the other hand, close to the overlapping region the peridynamic part of the domain may be characterised by a softer response in comparison to that of other parts of the domain (this issue is related to the surface effect to be discussed in the next chapter). In order to address this shortcoming, there are some other studies which present a direct approach to couple peridynamics with FEM. Liu and Hong [55] comprehensively investigated a direct coupling, based on force partitioning at the discretized level, by introducing interface elements. However, this approach requires an iterative solution of a nonlinear system in the case of irregular discretization of FEM meshes. Furthermore, dispersion effects and spurious reflection of waves are common in FEM - peridynamics couplings due to severe distortion of elements and to the adoption of non-uniform grids in peridynamics [36], [56], [57]. It should be pointed out that the majority of the works in the literature are based on the coupling of a peridynamic model with FEM with a fixed partitioning of the domain. Also one can find the works in [58], [59] concerning the solution of soil fragmentation problems by the coupling of a peridynamic model with the smoothed particle hydrodynamic method (SPH) as a meshless method.

Moreover, the way of applying boundary conditions in peridynamics is nonlocal and hence it is more challenging than the way adopted by methods based on the classical continuum theory. This issue is well-known to scientists working in peridynamics, and several suggestions in the literature can be found on how to apply boundary conditions in a more accurate way; for instance, see [46], [60]. It is worthwhile to mention as well,

based on the comprehensive studies conducted in [61], that the meshfree discretization in peridynamics leads directly to an approximation of the derivatives that can be obtained from the moving least squares reproducing kernel particle method (MLS/RKPM) [62], [63]. Therefore, based on the demonstration presented in [61], adopting some other compatible meshless approaches for the parts close to the boundaries can also be a way to apply the boundary conditions effectively.

Coupling of peridynamics with a meshless method based on classical continuum mechanics may be a way to avoid the aforementioned problems. One can find a variety of studies in which the main focus is about coupling meshless methods with other types of methods like FEM for instance [64]–[66]. This brings the idea of applying peridynamics only to the parts where mechanisms such as damage and fracture strongly influence the solution, while the rest of the domain, where the solution is smooth, is simulated with a computational model based on the local theory that reduces computational cost and satisfies classical conditions.

The main purpose of the present study is to develop an effective nonlocal/local meshless coupling technique for the solution of two-dimensional elastodynamic problems involving brittle crack propagation. This method is based on a coupling between the peridynamic meshless method, introduced in [32] and two other meshless methods based on the classical continuum theory. In the present study two different meshless methods, the Meshless Local Exponential Basis Functions (MLEBF) [67] and the Finite Point Method (FPM) [68] are chosen to develop the coupling approach. Such a selection is due to the fact that MLEBF and FPM are classified within the category of strong form meshless methods which are simple and computationally cheap. As we will show in the

subsequent chapters, for meshless nodes (MLEBF or FPM nodes) supporting sizes much smaller than that of peridynamic nodes are employed. In this way, a significant increase in efficiency for the coupled method in comparison to a peridynamic-only approach will be obtained.

We shall show that the present coupling method offers some advantages. Its basic appealing features are:

- The coupling is done in a complete meshless style without introducing any blending function, particular shape functions, or extra numerical artifacts.
- It benefits from the full advantages of both theories preserving the originality of their discretized form.
- It is free of ghost forces.
- It can be used not only for a fixed partitioning but also for an adaptive partitioning of the solution domain to reduce the computational effort.

An approach similar to the one proposed in the present work can be found in [69], where it is called a *splice model*. However, the present contribution has been developed independently and focuses in a more detailed way on the coupling of peridynamic grids with meshless methods and on the many practical issues related to the implementation.

The chapters of the thesis are organized as follows: In Chapter 2 an overview of the bond-based peridynamic formulation and its discretization by a meshless approach is presented. In Chapter 3 the MLEBF will be explained and a switching approach to couple it with peridynamics is presented. In Chapter 4 we recall the solution strategy of the FPM in the solution of elasticity problems and then we extend it for the solution of elastodynamic problems and describe the time integration used in the present study.

Chapter 5 is devoted to give a comprehensive explanation of the introduced coupling approach in the case of dynamic problems, and the way how to apply it in an adaptive style. The work will be concluded in Chapter 6.

2. Overview of the peridynamic theory

2.1 Equations of motion

Suppose that a body occupies a spatial region Ω in a reference configuration. Reference configuration stands for a set including the initial positions of all material points of the body, i.e., the body configuration at $t = 0$. In peridynamics, it is assumed that the body is composed of material points located at generic positions $\mathbf{X}$ to which infinitesimal volumes $dV_{\mathbf{X}}$ are associated. It is assumed that a material point with a position $\mathbf{X}$ (hereinafter referred to as point $\mathbf{X}$) interacts with other surrounding points even if they are not in contact, provided that the distance between them is less than a threshold value δ called the *horizon*. For bond-based peridynamics, the acceleration of a material point $\mathbf{X}$, in the reference configuration, at time instant $t > 0$ is [29]:

$$\rho(\mathbf{x})\ddot{\mathbf{u}}(\mathbf{X},t) = \int_{H_{\mathbf{X}}} \mathbf{f}[\mathbf{u}(\mathbf{X}',t) - \mathbf{u}(\mathbf{X},t), \mathbf{X}' - \mathbf{X}]dV_{\mathbf{X}'} + \mathbf{b}(\mathbf{X},t), \quad \forall \mathbf{X}' \in H_{\mathbf{X}} \tag{2.1}$$

Hereinafter the bold letters represent vectors, one dot and two dots over a letter represent first order and second order time derivatives, respectively. In Eq (2.1) $H_{\mathbf{X}}$ is the neighborhood of points of material point $\mathbf{X}$ (see Figure 2.1), $\mathbf{u}$ is the displacement vector field, $\mathbf{b}$ is a body force density field which represents the external force per unit of reference volume, ρ is the mass density, and $\mathbf{f}$ is the paiwise peridynamic force function, with the dimension of force per unit volume squared, that the material point $\mathbf{X}'$ exerts on point $\mathbf{X}$. In fact $\mathbf{f}$ is referred to as an interactive nonlocal *response function*

force, also called *bond force* in the peridynamic terminology [29]. It depends on the initial relative position and relative displacement of two interacting points, and it includes all the constitutive information of the material. We shall show that no assumptions on the continuity of the displacement field is required in Eq (2.1).

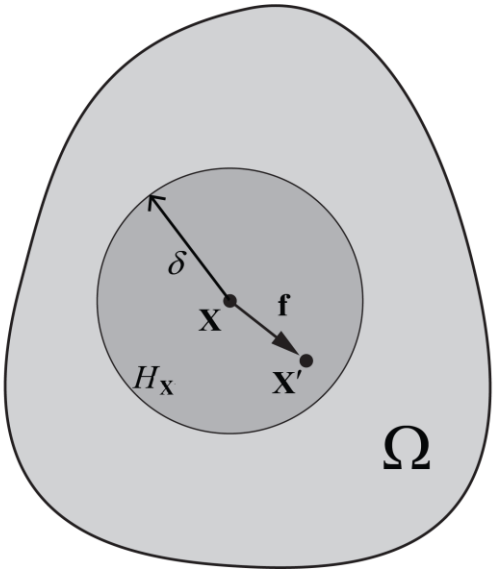

Figure 2.1. Neighborhood of a generic material point $\mathbf{X}$.

It should be remarked that the governing equation of motion in peridynamics shares some similarities with that of traditional molecular dynamics as a summation of interactions between neighboring material points/particles are involved in both. In molecular dynamics, a material is viewed as a collection of individual particles of finite size; however, from the peridynamic view-point a material is a collection of material points of infinitesimally small size. Therefore, peridynamics is a continuum theory.

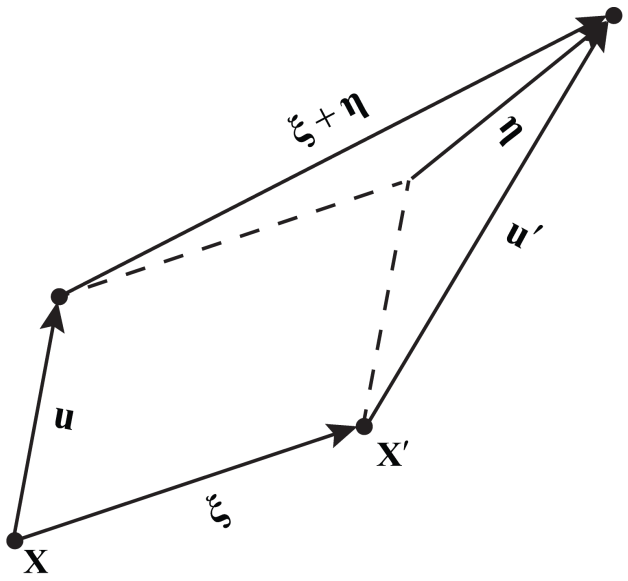

Figure 2.2. Definition of relative position $\boldsymbol{\xi}$ *and relative displacement* $\boldsymbol{\eta}$ *between two material points.*

To proceed with the formulation of peridynamics two frequently used terms are defined. Considering two generic material points, $\mathbf{X}$ and $\mathbf{X}'$, as shown in Figure 2.2, the *relative position* or *bond* of these two material points with respect to the reference configuration is defined as:

$$\boldsymbol{\xi} = \mathbf{X}' - \mathbf{X} \tag{2.2}$$

also for the relative displacement of these two material points we have:

$$\boldsymbol{\eta} = \mathbf{u}(\mathbf{X}', t) - \mathbf{u}(\mathbf{X}, t) \tag{2.3}$$

Therefore, based on the given definitions, $\|\boldsymbol{\xi}\|$ is the undeformed bond length and $\|\boldsymbol{\xi} + \boldsymbol{\eta}\|$ is the deformed bond length; see Figure 2.2.

As a consequence of the integration domain assumed in Eq (2.1), the equation of motion of peridynamics is restricted to the integration of the forces in $H_{\mathbf{x}}$ which is a spherical neighborhood (in 3D) centered at the material point $\mathbf{X}$, defined by:

$$H_{\mathbf{x}} = \left\{ \mathbf{X}' \in \mathbb{R}^3 \,\middle|\, \left\| \mathbf{X}' - \mathbf{X} \right\| < \delta \right\} \tag{2.4}$$

for two-dimensional and one-dimensional problems $H_{\mathbf{x}}$ becomes a circle or a line, respectively.

In view of Newton's third law, the force function $\mathbf{f}$, for conservation of linear momentum, should satisfy the following condition:

$$\mathbf{f}(-\boldsymbol{\eta}, -\boldsymbol{\xi}) = -\mathbf{f}(\boldsymbol{\eta}, \boldsymbol{\xi}) \tag{2.5}$$

also conservation of angular momentum requires:

$$(\boldsymbol{\eta} + \boldsymbol{\xi}) \times \mathbf{f}(\boldsymbol{\eta}, \boldsymbol{\xi}) = \mathbf{0} \tag{2.6}$$

in this sense, the force vector between two material points must be parallel to their current relative position $\boldsymbol{\eta} + \boldsymbol{\xi}$.

As a consequence, in view of Eqs (2.5) and (2.6), a general form of $\mathbf{f}(\boldsymbol{\eta}, \boldsymbol{\xi})$ can be expressed as [29]:

$$\mathbf{f}(\boldsymbol{\eta}, \boldsymbol{\xi}) = F(\boldsymbol{\eta}, \boldsymbol{\xi})(\boldsymbol{\eta} + \boldsymbol{\xi}), \quad \forall \boldsymbol{\eta}, \boldsymbol{\xi} \tag{2.7}$$

where $F(\boldsymbol{\eta}, \boldsymbol{\xi})$ is an appropriate scalar valued function.

2.2 Elasticity

In bond-based peridynamics elastic behavior (elasticity) of a material is considered by defining the concept of *microelasticity*. A material is called microelastic if it fulfills the following condition [29]:

$$\oint_{\Gamma} \mathbf{f}(\boldsymbol{\eta}, \boldsymbol{\xi}) \cdot d\boldsymbol{\eta} = 0, \quad \forall \text{closed curve } \Gamma, \quad \forall \boldsymbol{\xi} \neq \mathbf{0} \tag{2.8}$$

in which $d\boldsymbol{\eta}$ is the differential vector path length along Γ. From this condition, similar to elasticity in the classic theory, it can be inferred that the line integral is path independent

so that the net work done by the response force along any closed curve is zero. On the basis of Stoke's Theorem, if $\mathbf{f} = (f_1, f_2, f_3)$ is continuously differentiable with respect to $\boldsymbol{\eta} = (\eta_1, \eta_2, \eta_3)$, then a necessary condition for Eq (2.8) to hold is:

$$\nabla_\eta \times \mathbf{f}(\boldsymbol{\eta}, \boldsymbol{\xi}) = (\frac{\partial f_3}{\partial \eta_2} - \frac{\partial f_2}{\partial \eta_3})\vec{\mathbf{i}} + (\frac{\partial f_1}{\partial \eta_3} - \frac{\partial f_3}{\partial \eta_1})\vec{\mathbf{j}} + (\frac{\partial f_2}{\partial \eta_1} - \frac{\partial f_1}{\partial \eta_2})\vec{\mathbf{k}} = \mathbf{0}, \quad \forall \boldsymbol{\xi} \neq \mathbf{0} \tag{2.9}$$

Another consequence of Stoke's theorem, since the force field is conservative and irrotational, is that the peridynamic force can be derived from a scalar-valued differentiable function w called *micropotential* as:

$$\mathbf{f}(\boldsymbol{\eta}, \boldsymbol{\xi}) = \frac{\partial w}{\partial \boldsymbol{\eta}}(\boldsymbol{\eta}, \boldsymbol{\xi}), \quad \forall \boldsymbol{\eta}, \boldsymbol{\xi} \tag{2.10}$$

It can be shown that the micropotential depends only on the relative displacement vector, $\boldsymbol{\eta}$, through the scalar distance between the deformed points [32]. Therefore, for isotropic microelastic peridynamic models one can define a scalar-valued function $\hat{w}$ such that:

$$w(\boldsymbol{\eta}, \boldsymbol{\xi}) = \hat{w}(\|\boldsymbol{\eta} + \boldsymbol{\xi}\|, \boldsymbol{\xi}), \quad \forall \boldsymbol{\eta}, \boldsymbol{\xi} \tag{2.11}$$

By substitution of the above equation in Eq (2.10), and considering Eq (2.7) a general peridynamic force function, aligned with the relative position vector, for microelastic material is obtained:

$$\mathbf{f}(\boldsymbol{\eta}, \boldsymbol{\xi}) = H(\|\boldsymbol{\eta} + \boldsymbol{\xi}\|, \boldsymbol{\xi})(\boldsymbol{\eta} + \boldsymbol{\xi}), \quad \forall \boldsymbol{\eta}, \boldsymbol{\xi} \tag{2.12}$$

where H is a scalar-valued even function:

$$H(p, \boldsymbol{\xi}) = \frac{\partial \hat{w}}{\partial p}(p, \boldsymbol{\xi}), \quad p = \|\boldsymbol{\eta} + \boldsymbol{\xi}\|, \quad \forall \boldsymbol{\eta}, \boldsymbol{\xi} \tag{2.13}$$

In fact the above equation is similar to that in Eq (2.7); however, here the dependence of the scalar part of the expression on the relative distance is concluded.

2.3 Linearization

The main focus of this thesis is on the elastic response of materials. In the general framework of peridynamics large deformation is allowed. This theory can be applied to a wide range of problems considering large deformations. By making the assumption of a small deformation, such that $(\|\boldsymbol{\eta}+\boldsymbol{\xi}\|-\|\boldsymbol{\xi}\|)/\|\boldsymbol{\xi}\| \ll 1$ for all $\boldsymbol{\xi}$. A Taylor expansion on $\boldsymbol{\eta}$ of first order to Eq (2.7) a peridynamic force function can be achieved as:

$$\mathbf{f}(\boldsymbol{\eta},\boldsymbol{\xi}) = \mathbf{C}(\boldsymbol{\xi})\boldsymbol{\eta} + \mathbf{f}(\mathbf{0},\boldsymbol{\xi}) \tag{2.14}$$

where $\mathbf{C}$ is a second-order tensor , called *micromodulus*, of the peridynamic force, and thus it can be computed as:

$$\mathbf{C}(\boldsymbol{\xi}) = \frac{\partial \mathbf{f}}{\partial \boldsymbol{\eta}}(\mathbf{0},\boldsymbol{\xi}) \tag{2.15}$$

the above equation can be rewritten as:

$$\mathbf{C}(\boldsymbol{\xi}) = \frac{\partial \mathbf{f}}{\partial \boldsymbol{\eta}}(\mathbf{0},\boldsymbol{\xi}) = \begin{bmatrix} \frac{\partial f_1}{\partial \eta_1}(\mathbf{0},\boldsymbol{\xi}) & \frac{\partial f_1}{\partial \eta_2}(\mathbf{0},\boldsymbol{\xi}) & \frac{\partial f_1}{\partial \eta_3}(\mathbf{0},\boldsymbol{\xi}) \\ \frac{\partial f_2}{\partial \eta_1}(\mathbf{0},\boldsymbol{\xi}) & \frac{\partial f_2}{\partial \eta_2}(\mathbf{0},\boldsymbol{\xi}) & \frac{\partial f_2}{\partial \eta_3}(\mathbf{0},\boldsymbol{\xi}) \\ \frac{\partial f_3}{\partial \eta_1}(\mathbf{0},\boldsymbol{\xi}) & \frac{\partial f_3}{\partial \eta_2}(\mathbf{0},\boldsymbol{\xi}) & \frac{\partial f_3}{\partial \eta_3}(\mathbf{0},\boldsymbol{\xi}) \end{bmatrix} \tag{2.16}$$

Also with respect to Eq (2.7), the micromodulus tensor can be obtained as:

$$\mathbf{C}(\boldsymbol{\xi}) = \boldsymbol{\xi} \otimes \frac{\partial F}{\partial \boldsymbol{\eta}}(\mathbf{0},\boldsymbol{\xi}) + F(\mathbf{0},\boldsymbol{\xi})\mathbf{I} \tag{2.17}$$

where $\mathbf{I}$ is an identity matrix and $\otimes$ is the dyadic or tensor product between two vectors which yields a tensor of second order. The condition expressed in Eq (2.9) for a microelastic material implies that:

$$\frac{\partial f_i}{\partial \eta_j} = \frac{\partial f_j}{\partial \eta_i}, \quad \text{for } i, j = 1,2,3 \tag{2.18}$$

Therefore, for a linear microelastic material, by introducing the above condition to Eq (2.15), one can conclude the micromodulus must be symmetric as:

$$\mathbf{C}(\boldsymbol{\xi}) = \mathbf{C}^T(\boldsymbol{\xi}), \quad \forall \boldsymbol{\xi} \tag{2.19}$$

A necessary and sufficient condition for the satisfaction of the above expression is that there should be a scalar-valued even function $\lambda(\boldsymbol{\xi})$ through which [29]:

$$\boldsymbol{\xi} \otimes \frac{\partial F}{\partial \boldsymbol{\eta}}(\mathbf{0}, \boldsymbol{\xi}) = \lambda(\boldsymbol{\xi}) \boldsymbol{\xi} \otimes \boldsymbol{\xi} \tag{2.20}$$

where

$$\lambda(\boldsymbol{\xi}) = \frac{\boldsymbol{\xi}}{\|\boldsymbol{\xi}\|^2} \frac{\partial F}{\partial \boldsymbol{\eta}}(\mathbf{0}, \boldsymbol{\xi}) \tag{2.21}$$

As a result, for a symmetric micromodulus we have:

$$\mathbf{C}(\boldsymbol{\xi}) = \lambda(\boldsymbol{\xi}) \boldsymbol{\xi} \otimes \boldsymbol{\xi} + F(0, \boldsymbol{\xi}) \mathbf{I} \tag{2.22}$$

Consequently, the linearized bond-based peridynamic force function can be explicitly reformulated in a general form as:

$$\mathbf{f}(\boldsymbol{\eta}, \boldsymbol{\xi}) = \left[\lambda(\boldsymbol{\xi}) \boldsymbol{\xi} \otimes \boldsymbol{\xi} + F(\mathbf{0}, \boldsymbol{\xi}) \mathbf{I} \right] \boldsymbol{\eta} + \mathbf{f}(\mathbf{0}, \boldsymbol{\xi}) \tag{2.23}$$

For a microelastic material, using $F(\boldsymbol{\eta}, \boldsymbol{\xi}) = H(p, \boldsymbol{\xi})$ [29], presents:

$$\lambda(\boldsymbol{\xi}) = \frac{1}{\|\boldsymbol{\xi}\|} \frac{\partial H}{\partial p}(\|\boldsymbol{\xi}\|, \boldsymbol{\xi}), \quad p = \|\boldsymbol{\xi} + \boldsymbol{\eta}\| \tag{2.24}$$

In a nutshell, the linearized peridynamic force function for a microelastic material is obtained as:

$$\mathbf{f}(\boldsymbol{\eta},\boldsymbol{\xi}) = \left[\frac{1}{\|\boldsymbol{\xi}\|}\frac{\partial H}{\partial p}(\|\boldsymbol{\xi}\|,\boldsymbol{\xi}) + H(\mathbf{0},\boldsymbol{\xi})\mathbf{I}\right](\boldsymbol{\xi}\otimes\boldsymbol{\xi})\boldsymbol{\eta} + \mathbf{f}(\mathbf{0},\boldsymbol{\xi}) \tag{2.25}$$

2.4 Areal force density

There is a concept called *force per unit area* that establishes a link between the bond-based peridynamics and the classic theory of elasticity. Assume that an infinite body Ω undergoes a homogeneous deformation. One may choose a point $\mathbf{X}$ in Ω and a unit vector $\mathbf{n}$ passing through the point. A plane normal to the vector can be considered to divide the body into two parts Ω^- and Ω^+ (Figure 2.3):

$$\Omega^+ = \{\mathbf{X}' \in \Omega : (\mathbf{X}' - \mathbf{X})\cdot\mathbf{n} \geq 0\}, \quad \Omega^- = \{\mathbf{X}' \in \Omega : (\mathbf{X}' - \mathbf{X})\cdot\mathbf{n} \leq 0\} \tag{2.26}$$

Let $\Im$ be a set of collinear points in Ω^- defined as follows:

$$\Im = \left\{\hat{\mathbf{X}} \in \Omega^- : \hat{\mathbf{X}} = \mathbf{X} - \bar{s}\mathbf{n}, 0 \leq \bar{s} < \infty\right\} \tag{2.27}$$

In the direction of $\mathbf{n}$ the *areal force density*, $\boldsymbol{\tau}(\mathbf{X},\mathbf{n})$, at $\mathbf{X}$ is defined [29]:

$$\boldsymbol{\tau}(\mathbf{X},\mathbf{n}) = \int_{\Im}\int_{\Omega^+} \mathbf{f}(\mathbf{u}' - \hat{\mathbf{u}}, \mathbf{X}' - \hat{\mathbf{X}})dV_{\mathbf{X}'}d\hat{l} \tag{2.28}$$

in which $d\hat{l}$ indicates the differential path length over $\Im$.

As the assumption of homogenous deformation is made, independent of $\mathbf{X}$, one can propose a meaningful representation of a stress tensor as:

$$\boldsymbol{\tau}(\mathbf{X},\mathbf{n}) = \boldsymbol{\sigma}\mathbf{n}, \quad \forall\mathbf{n} \tag{2.29}$$

Due to the calculation of the force per unit area $\boldsymbol{\tau}$ with respect to the reference configuration, the proposed stress tensor is a Piola-Kirchhoff stress tensor.

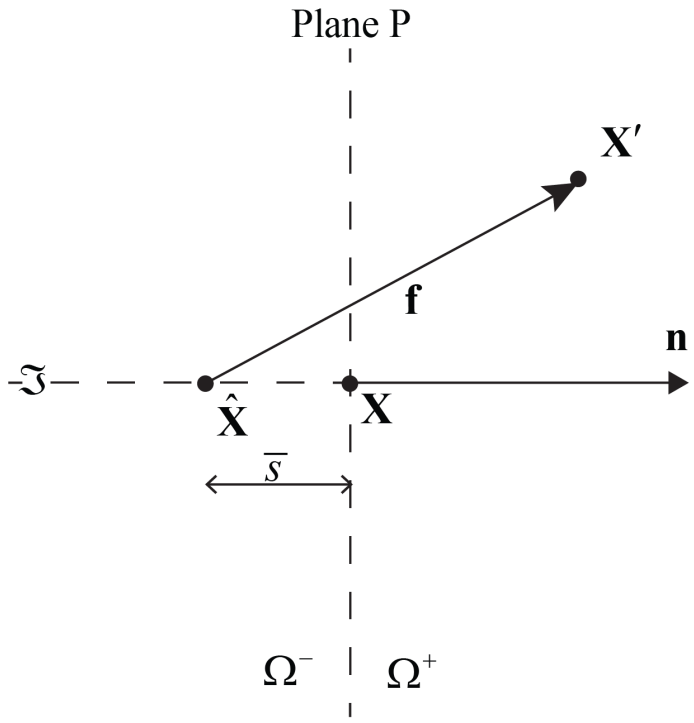

Figure 2.3. Definition of areal force density.

2.5 Unstressed configuration

Assuming an unstressed configuration of a body leads to a restriction on the scalar-valued function F discussed in this section. A configuration is defined to be unstressed if the following condition is observed [29]:

$$\boldsymbol{\tau}(\mathbf{X},\mathbf{n}) = \mathbf{0}, \quad \forall \mathbf{n} \tag{2.30}$$

Considering a set of orthonormal basis vectors as $\{\mathbf{e}_1, \mathbf{e}_2, \mathbf{e}_3\}$, setting $\mathbf{X} = 0$, and taking $\mathbf{n} = \mathbf{e}_1$, in Eq (2.27) gives:

$$\hat{\mathbf{X}} = -\bar{s}\mathbf{e}_1 \tag{2.31}$$

and we have:

$$\boldsymbol{\xi} = \mathbf{X}' - \mathbf{X} = \mathbf{X}' + \bar{s}\mathbf{e}_1 \tag{2.32}$$

another consequence, on the basis of Eq (2.7), is that for $\boldsymbol{\eta} = 0$:

$$\mathbf{f}(\boldsymbol{\eta},\boldsymbol{\xi}) = \mathbf{f}(\mathbf{0},\boldsymbol{\xi}) = F(\mathbf{0},\boldsymbol{\xi})\boldsymbol{\xi} \tag{2.33}$$

Likewise, the areal force density, by Eq (2.28), in the direction of $\mathbf{e}_1$ can be calculated as:

$$\boldsymbol{\tau}(\mathbf{0},\mathbf{e}_1) = \int_0^\infty \int_{\Omega^+} F(\mathbf{0},\mathbf{X}' + \bar{s}\mathbf{e}_1)(\mathbf{X}' + \bar{s}\mathbf{e}_1) dV_{X'} d\bar{s} \tag{2.34}$$

For the sake of simplicity, the integration variables can be converted into spherical coordinates as (see Figure 2.4):

$$\xi_1 = r\cos(\theta), \quad \xi_2 = r\sin(\theta)\cos(\phi), \quad \xi_3 = r\sin(\theta)\sin(\phi) \tag{2.35}$$

where $r = \|\boldsymbol{\xi}\|$. Therefore, Eq (2.34) can be written as:

$$\tau(\mathbf{0},\mathbf{e}_1) = \int_0^\infty \int_0^r \int_0^{\cos^{-1}(\bar{s}/r)} \int_0^{2\pi} F(0,r)(r\cos\theta) r^2 \sin\theta \, d\phi \, d\theta \, d\bar{s} \, dr = \frac{2\pi}{3}\int_0^\infty F(0,r) r^4 dr \tag{2.36}$$

and, on the basis of Eq (2.30), one may conclude:

$$\psi = \frac{2\pi}{3}\int_0^\infty F(0,r) r^4 dr = 0 \tag{2.37}$$

The above expression represents the aforementioned restriction on F. As Eq (2.36) is expressed in spherical coordinate system, the corresponding arguments are not vectors as in Eq (2.34).

2.6 Poisson's ratio in bond-based peridynamics

The assumptions of the bond-based Peridynamic theory impose a fixed value of the Poisson's ratio. Such a limitation lies in the nature of bonds that are characterized based on only pairwise interactions. This restriction has been addressed in the state-based version of peridynamics [30], yet that version is computationally much more expensive than the bond-based one. In this section, we shall show that such a fixed value for

Poisson's ratio can be determined by equating the stress tensor of the areal force density concept with that obtained by the classical stress tensor. The two stress tensors are compared considering the same strain in a homogeneous linear elastic body.

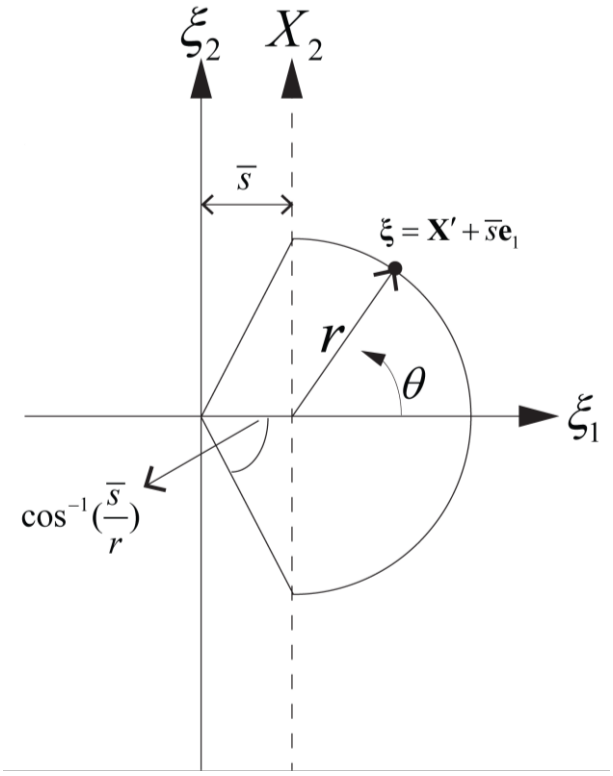

Figure 2.4. Change of variables.

Let an orthonormal basis be given by $\{\mathbf{e}_1, \mathbf{e}_2, \mathbf{e}_3\}$, and assume an infinite linear microelastic body, which is unstressed in the reference configuration and undergoes a homogeneous deformation given by $u_1 = c_{11}X$ and $u_2 \equiv u_3 \equiv 0$. Noting that $\{u_1, u_2, u_3\}$ are the components of the displacement field **u** [29]. Substitution of the displacement components in Eqs (2.2) and (2.3) yields $\eta_1 = c_{11}\xi_1$, $\eta_2 \equiv \eta_3 \equiv 0$. By replacing the obtained relative displacements into Eq (2.23) we have:

$$\mathbf{f}(\boldsymbol{\eta},\boldsymbol{\xi}) = \left\{ \lambda(\boldsymbol{\xi}) \begin{bmatrix} \xi_1^{\,2} & \xi_1\xi_2 & \xi_1\xi_3 \\ \xi_2\xi_1 & \xi_2^{\,2} & \xi_2\xi_3 \\ \xi_3\xi_1 & \xi_3\xi_2 & \xi_3^{\,2} \end{bmatrix} + F(\mathbf{0},\boldsymbol{\xi}) \begin{bmatrix} 1 & 0 & 0 \\ 0 & 1 & 0 \\ 0 & 0 & 1 \end{bmatrix} \right\} \begin{Bmatrix} \eta_1 \\ \eta_2 \\ \eta_3 \end{Bmatrix} = \begin{Bmatrix} c_{11}[\lambda(\boldsymbol{\xi})\xi_1^{\,3} + F(\mathbf{0},\boldsymbol{\xi})\xi_1] \\ c_{11}\lambda(\boldsymbol{\xi})\xi_1^{\,2}\xi_2 \\ c_{11}\lambda(\boldsymbol{\xi})\xi_1^{\,2}\xi_3 \end{Bmatrix} \tag{2.38}$$

Likewise, the nine components of the stress tensor $\boldsymbol{\sigma}$ can be obtained with respect to Eq (2.28) as follows:

$$\sigma_{ij} = \tau_j(\mathbf{e}_i) = \int_{\Im}\int_{\Omega^+} f_j dV_{\mathbf{X}'} d\hat{l}, \quad \text{for } i, j = 1,2,3 \tag{2.39}$$

Derivation of the first three components, using the change of variable rule, explained for Eq (2.35), gives:

$$\begin{aligned} \sigma_{11} &= \tau_1(\mathbf{e}_1) = \int_{\Im}\int_{\Omega^+} f_1 dV_{X'} d\hat{l} \\ &= c_{11}\int_0^{\infty}\int_0^{r}\int_0^{\cos^{-1}(\bar{s}/r)}\int_0^{2\pi} [\lambda(r)(r\cos\theta)^3 + F(0,r)(r\cos\theta)] r^2 \sin\theta d\phi d\theta d\bar{s} dr \\ &= c_{11}\left[\frac{2\pi}{5}\int_0^{\infty}\lambda(r)r^6 dr + \frac{2\pi}{3}\int_0^{\infty} F(0,r)r^4 dr\right] = c_{11}(\Lambda + \psi) \end{aligned} \tag{2.40}$$

$$\begin{aligned} \sigma_{12} &= \tau_2(\mathbf{e}_1) = \int_{\Im}\int_{\Omega^+} f_2 dV_{\mathbf{X}'} d\hat{l} \\ &= c_{11}\int_0^{\infty}\int_0^{r}\int_0^{\cos^{-1}(\bar{s}/r)}\int_0^{2\pi} [\lambda(r)(r\cos\theta)^2 r\sin\theta\cos\phi] r^2 \sin\theta d\phi d\theta ds dr \\ &= 0 \end{aligned} \tag{2.41}$$

$$\begin{aligned} \sigma_{13} &= \tau_3(\mathbf{e}_1) = \int_{\Im}\int_{\Omega^+} f_3 dV_{\mathbf{X}'} d\hat{l} \\ &= c_{11}\int_0^{\infty}\int_0^{r}\int_0^{\cos^{-1}(\bar{s}/r)}\int_0^{2\pi} [\lambda(r)(r\cos\theta)^2 r\sin\theta\sin\phi] r^2 \sin\theta d\phi d\theta ds dr \\ &= 0 \end{aligned} \tag{2.42}$$

where on the basis of Eq (2.37) $\psi = 0$, and Λ is defined by:

$$\Lambda = \frac{2\pi}{5}\int_0^{\infty}\lambda(r)r^6 dr \tag{2.43}$$

A similar calculation can be performed for the other six components of $\boldsymbol{\sigma}$. To exemplify, for the components in the direction of $\mathbf{e}_2$ the variables in Eq (2.35) should be changed to:

$$\xi_1 = r\sin(\theta)\sin(\phi),\quad \xi_2 = r\cos(\theta),\quad \xi_3 = r\sin(\theta)\cos(\phi) \tag{2.44}$$

then we obtain:

$$\boldsymbol{\sigma} = c_{11}\begin{bmatrix} \Lambda & 0 & 0 \\ 0 & \dfrac{\Lambda}{3} & 0 \\ 0 & 0 & \dfrac{\Lambda}{3} \end{bmatrix} \tag{2.45}$$

The stress tensor on the basis of the same given assumptions can be calculated by the classical theory of isotropic linear elasticity as:

$$\boldsymbol{\sigma} = \begin{bmatrix} \bar{\lambda}+2\bar{\mu} & \bar{\lambda} & \bar{\lambda} \\ \bar{\lambda} & \lambda+2\bar{\mu} & \bar{\lambda} \\ \bar{\lambda} & \bar{\lambda} & \bar{\lambda}+2\bar{\mu} \end{bmatrix}\begin{Bmatrix} c_{11} \\ 0 \\ 0 \end{Bmatrix} \tag{2.46}$$

which can be simplified as:

$$\boldsymbol{\sigma} = c_{11}\begin{bmatrix} \bar{\lambda}+2\bar{\mu} & 0 & 0 \\ 0 & \bar{\lambda} & 0 \\ 0 & 0 & \bar{\lambda} \end{bmatrix} \tag{2.47}$$

where $\bar{\lambda}$ and $\bar{\mu}$ are the Lame's first parameter and the shear modulus, respectively. Equating Eq (2.45) with Eq (2.47) gives the following results:

$$\nu = \frac{1}{4},\quad E = \frac{5\Lambda}{6},\quad \bar{\mu} = \frac{\Lambda}{3} \tag{2.48}$$

where ν and E stand for the Poisson's ratio and Young's modulus, respectively. In the final analysis, the obtained results reveal that for an isotropic linear microelastic bond-based peridynamic material undergoing a homogenous deformation, the value of the

Poisson's ratio is fixed to 0.25. The unknown term Λ, which is not directly measurable, is also linked to ν and E [29].

2.7 The prototype microelastic brittle (PMB) material model

In peridynamics, the simplest material model that has been the subject of many studies is the *prototype microelastic brittle* (PMB) constitutive model introduced in [32]. The interaction in that peridynamic model is similar to mechanical springs with the following features:

- The peridynamic force $\mathbf{f}$ is a linear function of the *bond stiffness* c, and this relationship is established through the bond elongation, or stretch, s defined as:

$$s = \frac{\|\boldsymbol{\xi} + \boldsymbol{\eta}\| - \|\boldsymbol{\xi}\|}{\|\boldsymbol{\xi}\|} \tag{2.49}$$

- Insertion of failure in such a peridynamic model is an easy task. It suffices to consider that peridynamic bonds can break when their stretch exceeds a predefined limit value s_0, called the *critical stretch* [32] The details on how to compute it will be presented in Section 2.8.
- Failure is an irreversible phenomenon. In this sense, once the bond fails it cannot be recovered. Moreover, the bond does not fail in compression. In principle, healing and compression can be modeled in peridynamics.

For materials of PMB type, the scalar valued function H, defined in Eq (2.12), is a linear function of the bond stiffness and the bond stretch:

$$H(\|\boldsymbol{\eta} + \boldsymbol{\xi}\|, \boldsymbol{\xi}) = \frac{c(\boldsymbol{\xi})\mu(\boldsymbol{\xi})s}{\|\boldsymbol{\eta} + \boldsymbol{\xi}\|} \tag{2.50}$$

where μ is a history dependent scalar-valued function that takes either a value of 0 or 1 depending on the status of the bond as:

$$\mu(\boldsymbol{\xi}) = \begin{cases} 1 & \text{if} \quad s(\boldsymbol{\xi}, t') < s_0, \quad 0 < t' < t \\ 0 & \text{else} \end{cases} \tag{2.51}$$

In turn, μ represents the status of the bonds in the solution domain. Therefore, the peridynamic force function for a PMB material takes the following form:

$$\mathbf{f}(\boldsymbol{\eta}, \boldsymbol{\xi}) = c(\boldsymbol{\xi}) s \mu(\boldsymbol{\xi}) \frac{\boldsymbol{\eta} + \boldsymbol{\xi}}{\|\boldsymbol{\eta} + \boldsymbol{\xi}\|} \tag{2.52}$$

As the assumption of "small displacement" is made, also by taking $c(\boldsymbol{\xi})$ as a constant function, the above equations can be simplified by:

$$\mathbf{f}(\boldsymbol{\eta}, \boldsymbol{\xi}) = cs\mu(\boldsymbol{\xi}) \frac{\boldsymbol{\xi}}{\|\boldsymbol{\xi}\|} \quad \text{if} \quad \|\boldsymbol{\eta}\| \ll \|\boldsymbol{\xi}\| \tag{2.53}$$

The last parameter in Eq (2.52) that has to be specified is the bond stiffness c and $s = \|\eta\| / \|\xi\|$ in the linearized form. Using the concept of force areal density, described in Section 2.4, can be a strategy to express c in terms of known material properties. In this way, one may assume an infinite body that undergoes an isotropic deformation so that all the bonds have the same stretch equal to s. For the sake of simplicity, let us take $\xi = \|\boldsymbol{\xi}\|$ and $\eta = \|\boldsymbol{\eta} + \boldsymbol{\xi}\|$. Based on the definition of stretch it can be concluded that $\eta = s\xi$ and thus with respect to Eq (2.50) we have:

$$H = c\xi = \frac{c\eta}{\xi} \tag{2.54}$$

According to Eq (2.10) the micropotential of a single bond, or the potential energy density of a bond, can be computed as:

$$\hat{w} = \int H d\eta = \int \frac{c\eta}{\xi} d\eta = \frac{c\eta^2}{2\xi} = \frac{cs^2\xi}{2} \tag{2.55}$$

Integrating the above micropotential over all the bonds within the neighborhood of a given point results in finding the total elastic potential energy W at that point as:

$$W = \frac{1}{2}\int_{H_X} w(\boldsymbol{\eta}, \boldsymbol{\xi}) dV_{X'} \tag{2.56}$$

The factor $1/2$ before the integral is due to the fact that the potential energy of a bond is shared between its two interacting points. Then, introduction of Eq (2.55) into Eq (2.56) and using spherical coordinates concludes:

$$W = \frac{1}{2}\int_0^{\delta} (\frac{cs^2\xi}{2}) 4\pi\xi^2 d\xi = \frac{\pi c s^2 \delta^4}{4} \tag{2.57}$$

It is also possible to calculate the strain energy density of a point in the framework of the classical theory of elasticity using the following given tensors:

$$\boldsymbol{\varepsilon}_{ij} = \delta_{ij} s \tag{2.58}$$

$$\sigma_{ij} = 2\bar{\mu}\boldsymbol{\varepsilon}_{ij} + \bar{\lambda}\delta_{ij}\boldsymbol{\varepsilon}_{kk} \tag{2.59}$$

The above equations can be rewritten in a matrix form as:

$$\boldsymbol{\varepsilon} = \begin{bmatrix} s & 0 & 0 \\ 0 & s & 0 \\ 0 & 0 & s \end{bmatrix} \tag{2.60}$$

$$\boldsymbol{\sigma} = \begin{bmatrix} (2\bar{\mu}+3\bar{\lambda})s & 0 & 0 \\ 0 & (2\bar{\mu}+3\bar{\lambda})s & 0 \\ 0 & 0 & (2\bar{\mu}+3\bar{\lambda})s \end{bmatrix} \tag{2.61}$$

The strain energy density in the classical theory of elasticity can be computed as follows:

$$W = \frac{1}{2}\sigma_{ij}\varepsilon_{ij} = \frac{3}{2}(2\bar{\mu}+3\bar{\lambda})s^2 = 3Es^2 = \frac{9Ks^2}{2}, \quad \nu = 1/4 \tag{2.62}$$

where K is the bulk modulus of the material. Recalling the restriction of $\nu = 1/4$ according to the restriction explained in Section 2.6 the rest of the parameters can be stated as follows:

$$\bar{\mu} = \frac{E}{2(1+\nu)} = \frac{2E}{5} \tag{2.63}$$

$$\bar{\lambda} = \frac{E\nu}{(1-2\nu)(1+\nu)} = \frac{2E}{5} \tag{2.64}$$

$$K = \frac{E}{3(1-2\nu)} = \frac{2E}{3} \tag{2.65}$$

Equating Eq (2.57) with Eq (2.62) leads to find the bond/spring constant c as:

$$c = \frac{18K}{\pi\delta^4} \tag{2.66}$$

For a two-dimensional peridynamic model the same procedure to find the restricted Poisson's ratio and to determine the bond constant can be followed. In this way, the elastic energy can be computed for both plane stress and plane strain conditions. Then the following results can be achieved [39]:

$$c = \frac{12E}{\pi \bar{t}\,\delta^3(1+\nu)} \quad \begin{cases} \text{plane stress} & \nu = 1/3 \\ \text{plane strain} & \nu = 1/4 \end{cases} \tag{2.67}$$

where $\bar{t}$ is the plate thickness. Moreover, for the 1D case one can obtain [57]:

$$c = \frac{2E}{A\delta^2} \tag{2.68}$$

where A is the cross section area.

2.8 Failure criterion

This section is devoted to a brief discussion on the introduction of failure into a bond-based peridynamic model. As discussed earlier for a PMB material the failure criterion is based on a maximum stretch (or critical stretch) s_0 that a bond can withstand during its performance. A schematic diagram of the peridynamic force versus the bond stretch for a PMB material is illustrated in Figure 2.5. To determine s_0 we follow the procedure introduced in [32]. The critical bond stretch s_0 can somehow be linked to known macroscopic quantities such as the critical energy release rate of the material G_0.

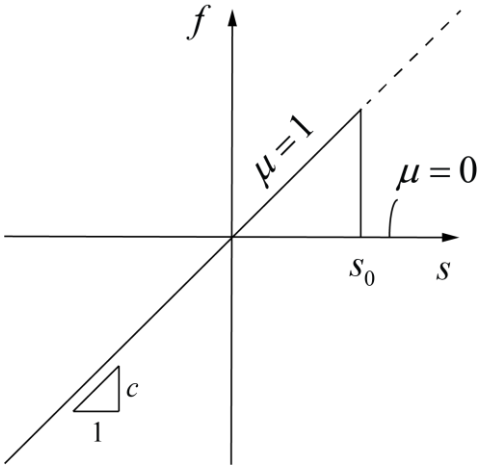

Figure 2.5. peridynamic force versus bond stretch.

It can be interpreted as the dissipated energy per unit area of fracture surface during the growing of a crack. In peridynamics separation of a body into two parts can be perceived as the breakage of all the bonds (across a fracture surface) that initially connected the points on the opposite sides. The connection between s_0 and G_0 can be established by assuming a complete separation of the fracture surface and neglecting the other dissipative mechanisms [32].

For a PMB material the required work to break a single bond can be calculated as follows:

$$w_0 = \int_0^{s_0} H(s)d\eta = \int_0^{s_0} H(s)\xi ds = \frac{cs_0{}^2\xi}{2} \tag{2.69}$$

For creation of a new fracture surface, it is required to break all the bonds crossing the mentioned surface. The energy per unit surface area, required to break all the bonds, is taken to be equal to the critical energy release rate G_0 derived from Griffith's theory [2]. Since the Griffith's criterion is based on the energy balance of the whole material surrounding the crack, it is a nonlocal criterion. The mentioned released energies, due to propagation of crack, can be related as:

$$G_0 = \int_0^{2\pi}\int_0^{\delta}\int_z^{\delta}\int_0^{\arccos(\frac{z}{\xi})} (\frac{cs_0{}^2\xi}{2})\xi^2 \sin\phi d\phi d\xi dz d\theta = \frac{\pi cs_0{}^2\delta^5}{10} \tag{2.70}$$

where the domain of integration and the variables are illustrated in Figure 2.6.

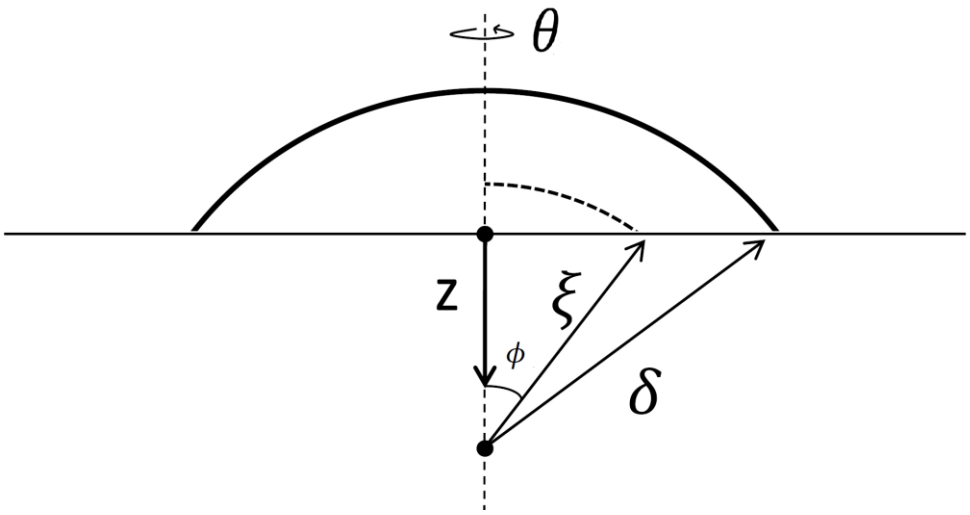

Figure 2.6. Variables involved in the computation of the critical stretch value.

From Eq (2.70) s_0 can be evaluated for three-dimensional problems as:

$$s_0 = \sqrt{\frac{10G_0}{\pi c \delta^5}} = \sqrt{\frac{5G_0}{9K\delta}} \tag{2.71}$$

while for two-dimensional problems it gets the following form:

$$s_0 = \sqrt{\frac{4\pi G_0}{9E\delta}} \tag{2.72}$$

For the mode I of crack (opening), the energy release rate can be related to the *fracture toughness* K_I through the following equation [32]:

$$G_0 = \frac{K_I^{\,2}}{E'} \tag{2.73}$$

where $E' = E$ for plane stress and $E' = E/(1-\nu^2)$ for plane strain.

The damage level $\bar{\phi}$ in a material point $\mathbf{X}$ at time t is defined by [32]:

$$\bar{\phi}(\mathbf{X},t) = 1 - \frac{\int_{H_X} \mu(\xi) dV_X}{\int_{H_X} dV_X} \tag{2.74}$$

and it takes a value between 0 and 1. The above equation considers the ratio of the number of broken bonds to the total number of bonds originally connected to point $\mathbf{X}$.

It should be noted that $\bar{\phi} = 0$ and $\bar{\phi} = 1$ respectively represent the undamaged state and the complete separation of a single material point from all surrounding points within its neighborhood.

2.9 Numerical discretization in bond-based peridynamics

Peridynamic models can be discretized using different numerical methods; a discussion on some types of discretization can be found in [70]. In the present study, we use the meshless approach introduced in [32] as it is simple and commonly used for problems involving failure.

2.9.1 Spatial integration

The numerical approximation of the peridynamic equation begins with the discretization of the solution domain with a set of grid points called *nodes* (see Figure 2.7).

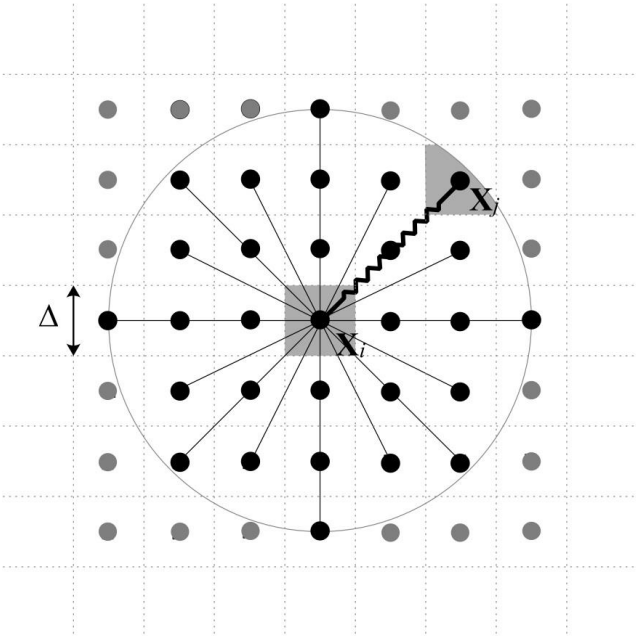

Figure 2.7. A spatial discretization for a peridynamic model.

The majority of works in the literature deal with uniform distribution of nodes for the sake of simplicity and convenience related to spatial integration. Hereinafter, the distance between two nearest neighboring nodes $\Delta x = \Delta y = \Delta$ is called the *grid spacing*. A cube (or a square cell in 2D) of material with a side length equal to one grid spacing is associated to each node called *node volume*. The node of interest at which the volume is centered is referred to as the *source node*. The union of all node volumes should appropriately cover the problem domain and represent well the border. Accordingly the time is discretized into instants as $t_1, t_2, \ldots, t_n$.

For a source node $\mathbf{X}_i$ the following discretized form of Eq (2.1) can be considered:

$$\rho\ddot{\mathbf{u}}_i^n = \sum_j \mathbf{f}(\mathbf{u}_j^n - \mathbf{u}_i^n, \mathbf{X}_j - \mathbf{X}_i)\beta_j V_j + \mathbf{b}_i^n, \quad \forall \mathbf{X}_j \in H_{X_i} \tag{2.75}$$

where n stands for the time step, and subscripts denote the node number (e.g., $\mathbf{u}_i^n = \mathbf{u}(\mathbf{x}_i, t^n)$). $\mathbf{u}_j^n$ is the displacement vector of a family node within the neighborhood of $\mathbf{X}_i$, V_j is the volume associated to $\mathbf{X}_j$. β_j is a volume correction factor that determines the portion of V_j that falls within the horizon of $\mathbf{X}_i$. In the present study, we apply the factor as recommended in [71]:

$$\beta = \begin{cases} 1 & \text{for} \quad \|\boldsymbol{\xi}\| \le \delta - 0.5\Delta x \\ \dfrac{\delta + 0.5\Delta x - \|\boldsymbol{\xi}\|}{\Delta x} & \text{for} \quad \delta - 0.5\Delta x < \|\boldsymbol{\xi}\| \le \delta + 0.5\Delta x \\ 0 & \text{otherwise} \end{cases} \tag{2.76}$$

The above equation takes into account the fact that the volume of nodes close to the boundary of the neighborhood H_X falls only partially within the horizon of the source node.

2.9.2 Time integration

To proceed in time, based on the suggestion in [32], an explicit central difference formula for the acceleration can be adopted:

$$\ddot{\mathbf{u}}_i^n = \frac{\mathbf{u}_i^{n+1} - 2\mathbf{u}_i^n + \mathbf{u}_i^{n-1}}{\Delta t^2} \tag{2.77}$$

where Δt is the time step size.

For the sake of consistency with most existing publications about peridynamics, the time integration adopted for all the dynamic simulations in this study is an explicit algorithm with a Velocity-Verlet time integration scheme. It is worth noting that this scheme is

commonly used in molecular dynamics. On the basis of studies conducted in [72], it has been demonstrated that Velocity-Verlet has a good numerical stability and it is similar to the leapfrog method [73]. This similarity originates from the fact that velocity is computed not only at the full step size but also at half step size. Calculation of step size has been subject of different studies in the literature [74].

Having known the displacement, velocity, and acceleration of each node at t^n, $(\mathbf{u}_i^n, \dot{\mathbf{u}}_i^n, \ddot{\mathbf{u}}_i^n)$, the simulation can proceed in time at $t^{n+1} = t^n + \Delta t$ as follows:

- calculate $\dot{\mathbf{u}}_i^{n+\frac{1}{2}} = \dot{\mathbf{u}}_i^n + \ddot{\mathbf{u}}_i^n \Delta t$
- calculate $\mathbf{u}_i^{n+1} = \mathbf{u}_i^n + \dot{\mathbf{u}}_i^{n+\frac{1}{2}} \Delta t$
- calculate $\ddot{\mathbf{u}}_i^{n+1}$ from to governing equation of the system Eq (2.75)
- calculate $\dot{\mathbf{u}}_i^{n+1} = \dot{\mathbf{u}}_i^{n+\frac{1}{2}} + \frac{1}{2}\ddot{\mathbf{u}}_i^{n+1} \Delta t$

A critical time step for the PMB models was first recommended in [32] as follows:

$$\Delta t_{crit} = \sqrt{\frac{2\rho}{\sum_j V_j c}} \tag{2.78}$$

where j varies over all the family nodes of a given node. Another option commonly found in the literature is the maximum critical step given by Courant-Friedrichs-Lewy (CFL) approach [74]:

$$\Delta t_{crit} = \frac{\Delta x}{c_w} \tag{2.79}$$

where c_w is the wave speed as:

$$c_w = \sqrt{\frac{K}{\rho}} \tag{2.80}$$

and thus the critical time step can be found:

$$\Delta t_{crit} = \Delta x \sqrt{\frac{\rho}{K}} \tag{2.81}$$

2.10 Loading and boundary conditions

Another important issue concerns the application of boundary conditions in peridynamics which is different from the classical continuum theory. Such a difference originates form the nonlocal nature of peridynamics. As the peridynamic equilibrium equations are based on integral operators, rather than partial differential operators, the traction boundary conditions should be applied over a volume similarly to body forces.

It should be remarked here that all the calculations done in the above sections are under the assumption that a node of interest is located inside an infinite body. That assumption is not valid for nodes close to the boundary of the body. This problem contributes to an undesirable effect called *soft boundary effect* [56], [75] for peridynamic models. This problem will be discussed further in Section 3.3. The prescribed boundary condition, similar to traction boundaries, should be imposed over a layer of nodes across the corresponding boundaries. The thickness of the layer most often is taken to be equal to the horizon value δ.

3. A switching technique to couple a 2D discretized peridynamic model with other meshless methods

3.1 Introduction

As discussed in Chapter 1, many meshless methods have so far been proposed and gained remarkable reputation over the past decades, and one can find a variety of studies in the literature regarding the coupling of meshless methods with FEM [5]. In this chapter, we aim at proposing a simple technique to couple peridynamics with the Meshless Local Exponential Basis Functions (MLEBF) method studied by Shojaei et al. [67], [76] which is a simplified version of the meshless method developed in [77]. Both of these studies originate from a method, the so called EBF (Exponential Basis Functions method) proposed by Boroomand et al. [78]. EBF falls within the category of boundary meshless methods and shares some similarities with Trefftz type methods [79]. The application of EBF to different engineering problems can be found in different studies as in [9], [80]–[87], and the generalized format of EBF for dealing with nonlinear problems is investigated in [88].

MLEBF falls within the category of truly meshless methods since it is free of any type of mesh. As the method uses residual free basis functions, which satisfy the strong form of the governing partial differential equation, no integration scheme appears in the solution procedure. MLEBF is not sensitive to the pattern of domain discretization, and it is capable of yielding highly accurate results with a high convergence rate for both uniform and non-uniform distribution of nodes in the solution domain. MLEBF uses a small

number of nodes in the approximation of unknown field variables within subdomains, so called *clouds*, compared with other meshless methods [67]. In this study, we shall use clouds with an average number of 9 nodes. This feature generates a sparse matrix with a narrow band width for the stiffness matrix of the final system of equations.

In this chapter, a simple switching technique to couple MLEBF with peridynamics is developed to take full advantage of both methods. The proposed technique efficiently introduces a transition region between the nonlocal and local discretized zones. In this sense, the method possesses desired characteristics such as proper satisfaction of Newton's third law and hence it does not exhibit ghost forces; moreover, we shall show that the method is patch test consistent. These features are regarded as essential factors for concurrent coupling schemes [50]. We shall show, in the section of numerical examples, that one can apply these coupling technique to overcome the surface effect for the satisfaction of boundary conditions which is a controversial issue in peridynamics [46], [54], [75].

In the current chapter we consider only static problems; however, this study paves the way to extend the strategy to wider classes of problems, such as those involving crack propagation, as well as to dynamic problems in the following chapters.

3.2 Problem description

The present chapter is about the solution of equilibrium problems in two-dimensional linear elastic bodies. Let us consider a 2D elastic body occupying a domain Ω bounded by Γ (see Figure 3.1). The boundary consists of a part Γ_D where Dirichlet boundary conditions are prescribed (imposed displacements $\mathbf{u}^*$), and a part Γ_N where

Neumann boundary conditions are prescribed (imposed tractions $\mathbf{t}^*$); the following conditions apply too: $\Gamma_D \cup \Gamma_N = \Gamma$ and $\Gamma_D \cap \Gamma_N = \varnothing$.

In the classical continuum mechanics the problem is described by the well-known equations that, in this case for linear isotropic homogenous materials, assume the following form for every point $\mathbf{X}$ of the domain:

$$\mathbf{S}^T\mathbf{DSu}(\mathbf{X}) + \mathbf{b}(\mathbf{X}) = \mathbf{0} \tag{3.1}$$

where, similarly to Eq (2.1), $\mathbf{u}$ and $\mathbf{b}$ are the displacement and the body force vectors, respectively. $\mathbf{S}$ is the well-known differential operator linking strains to displacement variables, and $\mathbf{D}$ is the matrix of material constants:

$$D = \begin{bmatrix} D_1 & D_2 & 0 \\ D_2 & D_1 & 0 \\ 0 & 0 & D_3 \end{bmatrix}, \quad \mathrm{S} = \begin{bmatrix} \partial/\partial X & 0 & \partial/\partial Y \\ 0 & \partial/\partial Y & \partial/\partial X \end{bmatrix}^T \tag{3.2}$$

in which:

$$\begin{aligned} &\text{Plane stress:} \quad D_1 = \frac{E}{1-\nu^2},\ D_2 = \frac{\nu E}{1-\nu^2},\ D_3 = \frac{E}{2(1+\nu)} \\ &\text{Plane strain:} \quad D_1 = \frac{E(1-\nu)}{(1+\nu)(1-2\nu)},\ D_2 = \frac{\nu E}{(1+\nu)(1-2\nu)},\ D_3 = \frac{E}{2(1+\nu)} \end{aligned} \tag{3.3}$$

Eqs (3.1)-(3.3) have been devised to deal with continuum mechanics and are difficult to apply whenever a discontinuity arises in the domain Ω since the spatial derivatives in Eq (3.2) are not well defined.

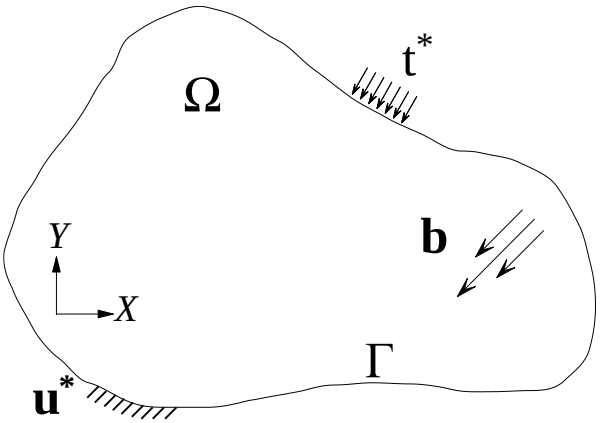

Figure 3.1. A general 2D equilibrium problem.

As discussed earlier, the main advantage of peridynamics is that the governing integral equation, Eq (2.1), is defined even if discontinuities are present in the domain Ω and thus peridynamics can be easily applied to problems affected by crack propagation. The main idea of the present chapter is to couple a discretized form of the bond-based peridynamics with a meshless method to solve equilibrium equations, in a way that exploits the strengths of both computational approaches and avoids at the same time their limitations.

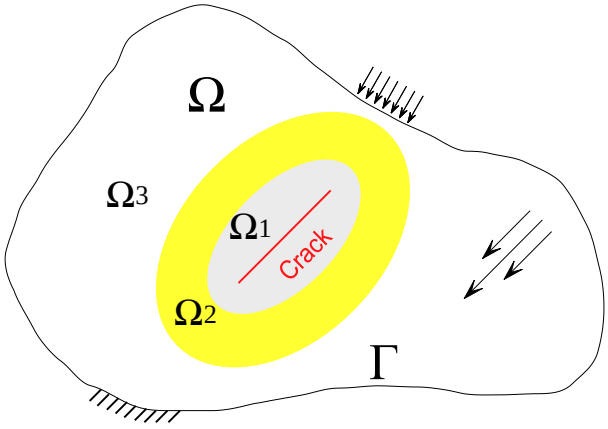

Figure 3.2. A general coupled 2D problem domain.

In the present work the solution domain will be split in three non-overlapping regions Ω_1, Ω_2 and Ω_3 such that $\Omega = \Omega_1 \cup \Omega_2 \cup \Omega_3$ (see Figure 3.2). Ω_1 is the nonlocal region

where the presence of cracks are of concern and will be discretized using bond-based peridynamics. Ω_3 denotes the local region where displacements are smooth and thus can be described within the framework of classical continuum mechanics; it will be discretized by means of the MLEBF. Ω_2 is the coupling region which provides a transition zone between both the nonlocal and local regions; a meshless scheme is introduced to make the transition feasible. In ordinary applications Ω_2 will cover a small portion of the domain. However, since it constitutes the most critical part of the coupling, in the examples of Section 3.7 the examined field will be just slightly larger than the transition zone.

3.3 Surface effect

In the subsequent section, we shall briefly recall the *surface* effect in peridynamics. It leads to some spurious unwilling effects in the numerical solution of a peridynamic model close to boundaries which is known as *soft boundary effect* or *skin effect* [46], [56]. Basically peridynamic material parameters, such as the micromodulus of the bonds (see Eqs (2.66)-(2.68)) are derived by assuming that the neighborhood H_X of the material point is fully embedded in the solution domain.

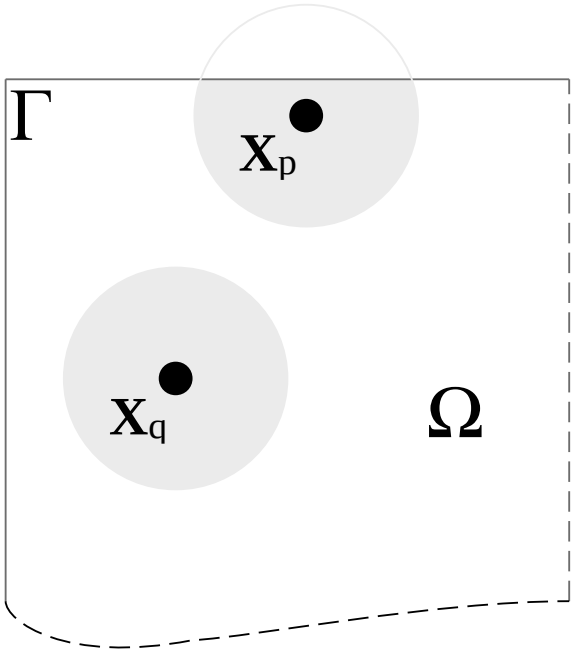

Figure 3.3. Surface effect in a peridynamic domain.

However, this assumption breaks down when the material point is close to any boundary. In this case, a portion of the neighbourhood associated with the material point falls outside the body; thus the horizon takes a truncated shape, as shown in Figure 3.3, and it does not contribute to its deformation energy. For instance, if the domain shown in Figure 3.3 is stretched with a constant strain, the potential energy density, see Eq (2.57), of a material point near an external surface is lower than in the bulk. As a consequence, a narrow zone close to the boundary of a body described by the peridynamic theory appears to be artificially softer than the rest of the body, the so called surface effect. Addressing of this effect has been the subject of some studies in the literature; to exemplify [54], [75], [89]. In the study conducted in [75] a way to apply a correction factor to the micromodulus of the bonds connected to points close to boundaries has been suggested. This correction factor, so called *force normalization*, is obtained considering the potential energy deformation of the corresponding material point under a homogenous loading

condition. However, it cannot cope with boundaries imposed by nonhomogeneous conditions, and hence a complete solution of the problem is not available yet [90], [91]. We shall show that the present coupling approach can also be considered as a way to imposed boundary conditions in a peridynamic model perfectly and to reduce many problems associated to the surface effect.

3.4 The meshless local exponential basis functions method (MLEBF)

This section presents a brief survey on MLEBF applied to the solution of problems based on the classical continuum theory as presented in Eqs (3.1)-(3.3). The reader interested in more details should refer to [67] on which the present section is based. The solution domain is represented by a set of randomly distributed nodes. Every node $\mathbf{X}_i$ is associated to a subdomain C_i, the so called *cloud* in the terminology of meshless methods. Indeed, C_i contains all the neighboring nodes on which the unknown vector of displacement $\mathbf{u}$ is to be approximated locally. Hereinafter, for the sake of consistency with the peridynamic terminology, we refer to neighboring nodes within the cloud C_i as the family nodes of node $\mathbf{X}_i$. For each cloud a local coordinate system is considered, and for the sake of simplicity, the axes of the local coordinate system are taken to be parallel to the global one (see Figure 3.4). There is no shape limitations for the clouds however their union should cover the whole domain.

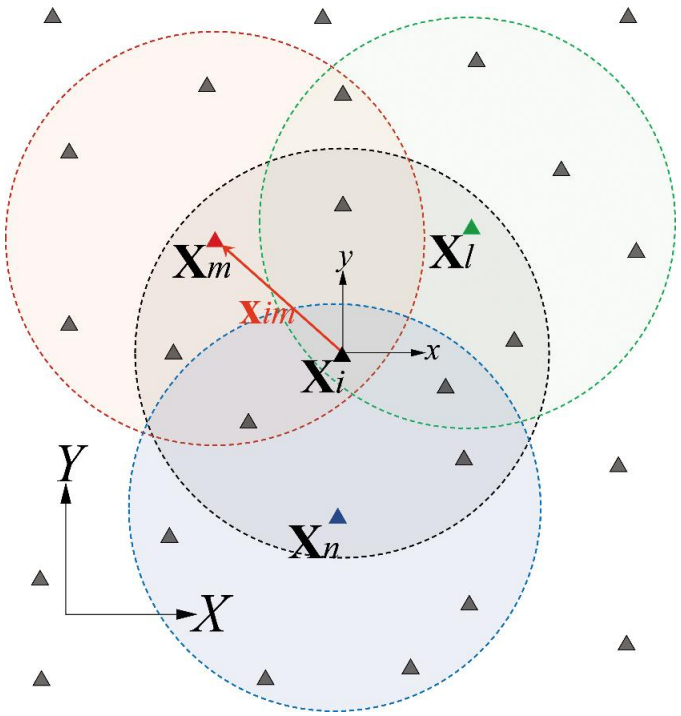

Figure 3.4. Schematic definitions of cloud, cloud center, family node, local coordinate system. Clouds are shown as circles in the figure, but this is not a requirement of MLEBF.

According to the linearity of Eq (3.1), the solution domain should be decomposed as:

$$\mathbf{u} = \mathbf{u}^h + \mathbf{u}^p \tag{3.4}$$

where p and h denote the homogenous and particular parts of the solution, respectively. Neglecting the body forces at this stage and focusing on the homogenous part of the solution, Eq (3.1) becomes:

$$\mathbf{S}^T \mathbf{D}\mathbf{S}\mathbf{u}^h(\mathbf{X}) = \mathbf{0} \tag{3.5}$$

In the MLEBF strategy the homogenous part of the solution is approximately constructed by a series of base functions as follows:

$$\mathbf{u}^h(\mathbf{x}) \cong \sum_{k=1}^{n_b} c'_k \boldsymbol{\psi}_k(\mathbf{x}) = \boldsymbol{\psi}(\mathbf{x})\mathbf{C}', \quad \mathbf{x} = (x, y) \tag{3.6}$$

where n_b denotes the number of basis functions, c_k' represents a series of unknown coefficients which are to be found in terms of DOFs; moreover, x and y are the components of local coordinate system. For 2D elasticity problems the bases in Eq (3.6) take the following form:

$$\boldsymbol{\psi}_k(\mathbf{x}) = \boldsymbol{\gamma}_k(\alpha_k, \beta_k)\exp(\alpha_k x + \beta_k y) \tag{3.7}$$

in which $\boldsymbol{\gamma}_k$ is a vector with a size equal to 2 due to the number of field variables. α_k and β_k are the exponents of the bases which are to be found in terms of each other. The relation between exponents in Eq (3.7) should be found so that the basis function can satisfy the strong form of the equilibrium equation in Eq (3.5). The strategy to derive the final format of the exponential basis functions (EBFs) has been comprehensively addressed in [78], and the strategy is summarized in Appendix A.

Inspired by the strategy given in [67], choosing a value for α_k results in finding two values for β_k and this can be repeated by choosing a value for β_k and finding two values for α_k. Likewise, by selecting both α_k and β_k from an identical set, i.e. $\boldsymbol{\mu} = \{\mu_1, \mu_2, \ldots\}$, and considering all possible combinations, the series expansion of EBFs can be found for a plane stress case as below:

$$\mathbf{u}^h \cong \sum_{j=1}^{b/8} c'_{j1}\exp(\mathrm{i}\mu_j x+\mu_j y)\begin{pmatrix}\mathrm{i}\\1\end{pmatrix}+c'_{j2}\exp(\text{-}\mathrm{i}\mu_j x+\mu_j y)\begin{pmatrix}-\mathrm{i}\\1\end{pmatrix}+$$
$$c'_{j3}\exp(\mathrm{i}\mu_j x+\mu_j y)\begin{pmatrix}\eta_3+(1-\mathrm{i})\eta_1/\mu_j\\\eta_2\end{pmatrix}+c'_{j4}\exp(-\mathrm{i}\mu_j x+\mu_j y)\begin{pmatrix}-\eta_3+(1+\mathrm{i})\eta_1/\mu_j\\\eta_2\end{pmatrix}+$$
$$c'_{j5}\exp(\mu_j x+\mathrm{i}\mu_j y)\begin{pmatrix}-\mathrm{i}\\1\end{pmatrix}+c'_{j6}\exp(\mu_j x-\mathrm{i}\mu_j y)\begin{pmatrix}\mathrm{i}\\1\end{pmatrix}+c'_{j7}\exp(\mu_j x-\mathrm{i}\mu_j y)\begin{pmatrix}\eta_3+(1+\mathrm{i})\eta_1/\mu_j\\\eta_2\end{pmatrix}+$$
$$c'_{j8}(\mu_j x+\mathrm{i}\mu_j y)\begin{pmatrix}-\eta_3+(1-\mathrm{i})\eta_1/\mu_j\\\eta_2\end{pmatrix}$$
(3.8)

where $\eta_1=(1-\mathrm{i})(-3+\nu)/(1+\nu)$, $\eta_2=1+x+y$, $\eta_3=\mathrm{i}+\mathrm{i}x+\mathrm{i}y$, $\mathrm{i}=\sqrt{-1}$. As a consequence the total number of EBFs in the expansion series of bases will be a multiple of eight.

The unknown coefficients $c'_k(\mathrm{k}=1,\ldots,b)$ in Eq (3.6) are to be determined in terms of the nodal values. A vector that collects the local coordinates of all the family nodes associated to $\mathbf{X}_i$ (see Figure 3.4) is defined as:

$$\mathbf{x}_i^R=\begin{pmatrix}\vdots\\\mathbf{x}_{il}\\\mathbf{x}_{im}\\\mathbf{x}_{in}\\\vdots\end{pmatrix},\quad (\mathbf{x}_{ij}=\mathbf{X}_j-\mathbf{X}_i)\ \&\ (\mathbf{X}_j\in C_i)\ \&\ (j\neq i) \tag{3.9}$$

Inserting the above collected local coordinates into Eq (3.6) and rewriting the equation in a matrix form leads to:

$$\bar{\mathbf{U}}_i^h=\mathbf{M}_i\mathbf{C}'_i,\quad \bar{\mathbf{U}}_i^h=\begin{pmatrix}\vdots\\\bar{\mathbf{u}}_l^h\\\bar{\mathbf{u}}_m^h\\\bar{\mathbf{u}}_n^h\\\vdots\end{pmatrix},\quad \mathbf{M}_i=\begin{bmatrix}\vdots\\\boldsymbol{\psi}(\mathbf{x}_{il})\\\boldsymbol{\psi}(\mathbf{x}_{im})\\\boldsymbol{\psi}(\mathbf{x}_{in})\\\vdots\end{bmatrix} \tag{3.10}$$

where $\bar{\mathbf{U}}_i^h$ and $\mathbf{M}_i$ are respectively the nodal values of the family nodes and the moment matrix associated to $\mathbf{x}_i$. As a result, based on the relation given in Eq (3.10), $\mathbf{C}_i'$ can be found as:

$$\mathbf{C}_i' = \mathbf{M}_i^+ \bar{\mathbf{U}}_i^h \tag{3.11}$$

where the superscript "+" stands for the Moor-Penrose generalized inverse. Substitution of $\mathbf{C}_i'$ from Eq (3.11) into Eq (3.6) results in:

$$\mathbf{u}_i^h(\mathbf{x}) = \boldsymbol{\varphi}_i(\mathbf{x})\bar{\mathbf{U}}_i^h, \quad \boldsymbol{\varphi}_i(\mathbf{x}) = \boldsymbol{\psi}(\mathbf{x})\mathbf{M}_i^+, \quad \text{in } C_i \tag{3.12}$$

where $\boldsymbol{\varphi}_i$ is a matrix containing all the shape functions associated to the family nodes. At this stage, one can suppose a situation in which a particular solution as $\mathbf{u}^p$ is a priory known. This function may not be unique, and it is capable of constructing the non-homogenous part of Eq (3.1) after being imposed to the governing PDE. According to the relation given in Eq (3.4), one can conclude:

$$\bar{\mathbf{U}}_i = \bar{\mathbf{U}}_i^h + \bar{\mathbf{U}}_i^p, \quad \bar{\mathbf{U}}_i = \begin{pmatrix} \vdots \\ \bar{\mathbf{u}}_l \\ \bar{\mathbf{u}}_m \\ \bar{\mathbf{u}}_n \\ \vdots \end{pmatrix}, \quad \bar{\mathbf{U}}_i^P = \begin{pmatrix} \vdots \\ \bar{\mathbf{u}}_l^p \\ \bar{\mathbf{u}}_m^p \\ \bar{\mathbf{u}}_n^p \\ \vdots \end{pmatrix} \tag{3.13}$$

As the relation between general nodal values is of concern, one can replace the above equation into Eq (3.12) and obtain:

$$\mathbf{u}_i(\mathbf{x}) = \mathbf{u}^p - \boldsymbol{\varphi}_i(\mathbf{x})(\bar{\mathbf{U}}_i - \bar{\mathbf{U}}_i^p), \quad \text{in } C_i \tag{3.14}$$

The above relation defines the approximated displacement field in terms of the nodal values of the family nodes.

In the case where the particular solution is not a priory known, it can be approximated through a collocation approach using again exponential basis functions. This is discussed in detail in Appendix A.

3.5 Bond-based peridynamic discrete form

In this section we recall the discretized formulation developed for a PMB model discussed in Section 2.9. It should be remarked here that the relation in Eq (2.53) is taking the assumption of small displacements. In this way, such an interaction between $\mathbf{X}_i$ and $\mathbf{X}_j$ can be considered as a spring (or truss element), and for a 2D problem it is obtained as:

$$\mathbf{k}_{ij} = \frac{c}{\|\boldsymbol{\xi}\|}\beta_j V_i V_j \begin{bmatrix} \xi_1^2 & \xi_1\xi_2 & -\xi_1^2 & -\xi_1\xi_2 \\ & \xi_2^2 & -\xi_1\xi_2 & -\xi_2^2 \\ & & \xi_1^2 & \xi_1\xi_2 \\ & & & \xi_2^2 \end{bmatrix} = \begin{bmatrix} \mathbf{k}_{ij}^{11} & \mathbf{k}_{ij}^{12} \\ \mathbf{k}_{ij}^{21} & \mathbf{k}_{ij}^{22} \end{bmatrix}, \quad \boldsymbol{\xi}=(\xi_1,\xi_2) \tag{3.15}$$

Figure 2.7 illustrates a horizon and bond interactions in a linearized discrete peridynamic model. The above equation is valid as long as the linearized formulation is used.

3.6 Forming the system of equations

3.6.1 The coupling scheme (switching technique)

Taking full advantage of both peridynamic and MLEBF computational techniques requires a suitable coupling scheme. As illustrated in Figure 3.2 Ω_1 is the region of the domain where only peridynamics is used, whereas only MLEBF is used in Ω_3. Ω_1 covers the parts of domain where damage or fracture are expected and nonlocal interaction is of concern; Ω_3 involves the parts where the deformation is smooth enough

to use the local model. The main novelty of the present work actually arises in the local/nonlocal transition part Ω_2. The thickness of this region depends on the horizon length of the peridynamic discretization and on the size of the clouds of the meshless part of the domain. The meshless parts stand for the parts solved by the MLEBF.

Figure 3.5 shows any possible position of the nodes in the solution domain with respect to the various layers of the grid. Four possible cases, A, B, C, and D can be considered for the position of the central node (source node) either of the peridynamic neighborhood or of the meshless cloud. We define four layers as shown in Figure 3.5.

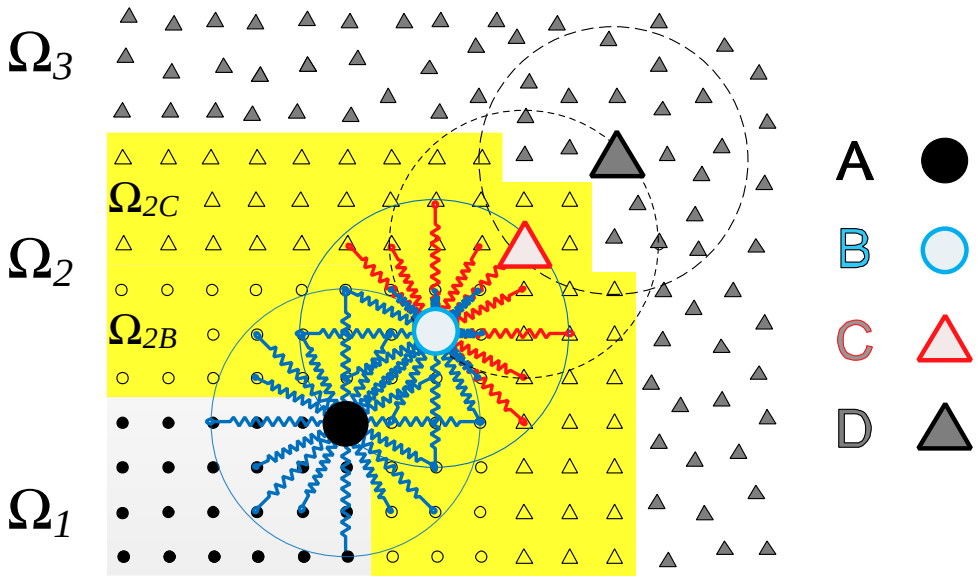

Figure 3.5. Coupling scheme used in the proposed strategy in the transition region.

Layer Ω_1: its nodes behave in all cases as peridynamic nodes, both as central nodes or family nodes of their neighbors (node A is a *pure* peridynamic node).

Layer Ω_{2B}: its nodes are switching nodes, but mainly of peridynamic type. They behave as peridynamic nodes if they are central nodes or family nodes for the nodes of layers Ω_1

and Ω_{2B}, but they behave as meshless nodes when they belong to the cloud of layers Ω_{2C} or Ω_3 (node B is a *switching* node).

Layer Ω_{2C}: its nodes are switching nodes, but mainly of meshless type. They behave as meshless nodes if they are central nodes or belong to the cloud of nodes of layers Ω_{2C} and Ω_3, but they behave as peridynamic nodes when they are within the horizon of nodes of layers Ω_1 or Ω_{2B} (node C is a switching node). The union of layers Ω_{2B} and Ω_{2C} is called Ω_2 in Figure 3.5 and constitutes the transition region.

Layer Ω_3: its nodes behave in all cases as meshless nodes, both as central nodes or when they belong to the cloud of their neighbors (node D is a *pure* meshless node). Therefore, the behavior of the family nodes is governed by the position of the relevant central node.

The size of Ω_{2B} has to be such that no meshless central node in Ω_{2C} or Ω_3 has any node belonging to Ω_1 in their cloud. In a similar way the size of Ω_{2C} has to be such that no peridynamic central node in Ω_1 and Ω_{2B} has any node belonging to Ω_3 within their neighborhood.

Remark I: The nodes in the transition region are split in two main sets: meshless nodes, in layer Ω_{2C}, and peridynamic nodes in layer Ω_{2B}. For the meshless nodes the governing equation and the material properties are identical to those of pure meshless nodes, those in layer Ω_3, and hence the state of stress at these nodes can be calculated based on classical strain-stress relationships. For the peridynamic nodes the governing equation and the material properties are identical to those of the pure peridynamic nodes, those in

layer Ω_1. Therefore, for these nodes, the internal forces (as well as stresses) can be calculated as shown at page 31 of reference [46]. ■

In the previous sections the formulations of bond-based peridynamics and MLEBF were discussed. In the peridynamic model, the relation between forces and displacements is obtained based on the nonlocal force interactions of any node with its family nodes within the neighborhood; which leads to the concept of equilibrium of the spring network. However, in MLEBF this relation is constructed, through the interpolation of the solution within clouds, by enforcing the local approximation to pass through the data at nodal values of the family nodes and imposing the displacement compatibility. Now let $\mathbf{K}$, $\mathbf{U}$ and $\mathbf{F}$ be the coefficient matrix, the unknown nodal displacement values and the vector of known values for the global system of equation. The final system of equations can be written as follows:

$$\mathbf{KU} = \mathbf{F} \tag{3.16}$$

Each element of the final system of equations should be determined appropriately with respect to the position of the nodes. Based on the connectivity between the nodes and the body forces exerted on the central node, the corresponding rows of the nodal values in $\mathbf{K}$ and $\mathbf{F}$ can be found by an assembly procedure.

If the central node $\mathbf{X}_i$ is a meshless node, the corresponding rows of the final system of equations can be obtained by inserting the local coordinates of node $\mathbf{X}_i$ defined as $\mathbf{x}_{i0}$ in Eq (3.14). Then we have:

$$\bar{\mathbf{u}}_i - \begin{bmatrix} \cdots & \boldsymbol{\varphi}_{il}(\mathbf{x}_{i0}) & \boldsymbol{\varphi}_{im}(\mathbf{x}_{i0}) & \boldsymbol{\varphi}_{in}(\mathbf{x}_{i0}) & \cdots \end{bmatrix} \begin{pmatrix} \vdots \\ \bar{\mathbf{u}}_l \\ \bar{\mathbf{u}}_m \\ \bar{\mathbf{u}}_n \\ \vdots \end{pmatrix} = \mathbf{u}^p \Big|_{\mathbf{x}_i} - \boldsymbol{\varphi}_i(\mathbf{x}_{i0}) \bar{\mathbf{U}}_i^p, \tag{3.17}$$

$$\boldsymbol{\varphi}_{ij} = \begin{bmatrix} \varphi_{ij}^{11} & \varphi_{ij}^{12} \\ \varphi_{ij}^{21} & \varphi_{ij}^{22} \end{bmatrix}$$

Now the coefficients of the nodal values should be simply replaced into the corresponding rows in $\mathbf{K}$. In this sense, the left hand side of Eq (3.17) indicates the coefficients associated to the $2i-1$-th and $2i$-th rows of $\mathbf{K}$; consequently, the right hand side should be placed into the corresponding rows in $\mathbf{F}$. It is worthwhile to mention that we benefit from one of the most important features of MLEBF regarding the elimination of the assembly process which is involved in many other conventional methods like peridynamics or FEM. If the central node is positioned on the borders the relation should be modified as discussed in more details later.

In order to get more insight into the way the matrix $\mathbf{K}$ is formed, we provide in the following equation the contributions to Eq (3.16) from nodes A, B, C, D, shown in Figure 3.5:

$$\mathbf{K} = \begin{bmatrix} \ddots & \vdots & \vdots & \vdots & \vdots & \vdots & \vdots & \vdots & \vdots \\ \cdots & \boxed{(\ldots + \mathbf{k}_{AB}^{11} + \ldots)} & \cdots & \boxed{(\ldots + \mathbf{k}_{AB}^{12} + \ldots)} & \cdots & \boxed{\mathbf{0}} & \cdots & \boxed{\mathbf{0}} & \cdots \\ \vdots & \vdots & \ddots & \vdots & \vdots & \vdots & \vdots & \vdots & \vdots \\ \cdots & \boxed{(\ldots + \mathbf{k}_{AB}^{21} + \ldots)} & \cdots & \boxed{(\ldots + \mathbf{k}_{AB}^{22} + \mathbf{k}_{BC}^{11} \ldots)} & \cdots & \boxed{(\ldots + \mathbf{k}_{BC}^{12} + \ldots)} & \cdots & \boxed{\mathbf{0}} & \cdots \\ \vdots & \vdots & \vdots & \vdots & \ddots & \vdots & \vdots & \vdots & \vdots \\ \cdots & \boxed{\mathbf{0}} & \cdots & \boxed{-\boldsymbol{\varphi}_{CB}(\mathbf{x}_{C0})} & \cdots & \boxed{\mathbf{I}} & \cdots & \boxed{-\boldsymbol{\varphi}_{CD}(\mathbf{x}_{C0})} & \cdots \\ \vdots & \vdots & \vdots & \vdots & \vdots & \vdots & \ddots & \vdots & \vdots \\ \cdots & \boxed{\mathbf{0}} & \cdots & \boxed{\mathbf{0}} & \cdots & \boxed{-\boldsymbol{\varphi}_{DC}(\mathbf{x}_{D0})} & \cdots & \boxed{\mathbf{I}} & \cdots \\ \vdots & \vdots & \vdots & \vdots & \vdots & \vdots & \vdots & \vdots & \ddots \end{bmatrix} \tag{3.18}$$

, and:

$$\mathbf{U}=\begin{pmatrix}\vdots\\ \bar{\mathbf{u}}_A\\ \vdots\\ \bar{\mathbf{u}}_B\\ \vdots\\ \bar{\mathbf{u}}_C\\ \vdots\\ \bar{\mathbf{u}}_D\\ \vdots\end{pmatrix},\quad \mathbf{F}=\begin{pmatrix}\vdots\\ \mathbf{b}(\mathbf{X}_A)\mathrm{V}_A\\ \vdots\\ \mathbf{b}(\mathbf{X}_B)\mathrm{V}_B\\ \vdots\\ \mathbf{u}^p\big|_{\mathbf{x}_C}-\boldsymbol{\varphi}(\mathbf{x}_{C0})\bar{\mathbf{U}}_C^p\\ \vdots\\ \mathbf{u}^p\big|_{\mathbf{x}_D}-\boldsymbol{\varphi}(\mathbf{x}_{D0})\bar{\mathbf{U}}_D^p\\ \vdots\end{pmatrix} \tag{3.19}$$

where the terms $\mathbf{k}$ are defined in Eq (3.15) and the terms $\boldsymbol{\varphi}$ are defined in Eq (3.17)

Remark II: The rows of the stiffness matrix in Eq (3.18) are filled out by coefficients derived either form the MLEBF formulation or from the peridynamic one. In the case of problems with large values of E, there might be an accumulation of large numbers for the rows related to peridynamic nodes while having smaller numbers for those of MLEBF nodes. This may result in an ill-conditioning for the system of equations, yet such a problem can be solved easily. It suffices to normalize the rows related to the peridynamic nodes with a simple factorization. No equation of system (3.19) contains terms coming from both formulations. ■

In this way, Ω_2 provides a suitable transition region for the analysis to switch the governing equations in different parts of the solution domain from a nonlocal to a local approach. This switching behavior somehow resembles the idea of the morphing strategy proposed in [51], [52] to couple nonlocal and local continuum mechanics. In the morphing strategy, a morphing function is employed to affect the constitutive parameters in the transition zone. This function varies from 0 to 1 and identifies the portion of the

constitutive parameters to be derived from the two different nonlocal and local theories. In this strategy, a suitable selection of the morphing function plays an important role in the analysis to eliminate the presence of ghost forces in the transition region. We shall examine the suitability of the strategy proposed in the present work against ghost forces in the section about numerical examples. The proposed switching strategy is simple and offers many advantages in terms of implementation. It contributes to a complete meshless approach, and preserves the advantages of the formulations of both models without introducing any morphing or blending functions into the formulation of the system.

We believe that the switching technique can be used in the case of static crack propagation adaptively. At the beginning of the solution procedure, the domain can be represented by MLEBF nodes. Then where cracks are likely to nucleate, MLEBF nodes can be adaptively changed into peridynamic nodes. In such a framework, the peridynamic part is forced to follow the propagation of cracks. When a crack reaches a boundary, peridynamic nodes have an inevitable projection on it. In such a case a very small portion of the boundary can be affected by the softening effect; yet the remaining parts are free from it. These issues will be addressed in future studies and are mentioned in the last chapter.

Eq (3.19) shows that the resulting system matrix is not symmetric. This type of coupling can be applied also to other meshless methods; however, here it was adopted for the MLEBF due to its efficiency.

3.6.2 Boundary condition satisfaction in MLEBF

For the satisfaction of Dirichlet boundary conditions, one can directly constrain the DOFs, yet for Neumann boundary conditions the procedure is more complicated. Let $\mathbf{L}_N$ be the operator defined on the traction boundary nodes as:

$$\mathbf{L}_N\mathbf{u}=\mathbf{t}^*,\quad \mathbf{L}_N\equiv\tilde{\mathbf{n}}\mathbf{D}\mathbf{S},\quad \tilde{\mathbf{n}}=\begin{bmatrix}0 & n_y & n_x\\ n_x & 0 & n_y\end{bmatrix} \tag{3.20}$$

in which n_x and n_y are the components of the outward unit vector normal to the boundary. For the nodes on which traction is imposed, in view of Eqs (3.4) and (3.20), by the appropriate introduction of coordinates of node $\mathbf{X}_i$, one can obtain:

$$\mathbf{L}_N\mathbf{u}^h\Big|_{\mathbf{x}_{i0}}=\mathbf{t}^*-\mathbf{L}_N\mathbf{u}^p\Big|_{\mathbf{x}_i} \tag{3.21}$$

Coupling the relations given in Eqs (3.21), (3.10) and (3.11) leads to:

$$\begin{pmatrix}\bar{\mathbf{U}}_i^h\\ \mathbf{t}^*-\mathbf{L}_N\mathbf{u}^p\Big|_{\mathbf{x}_i}\end{pmatrix}=\begin{bmatrix}\mathbf{M}_i\\ \mathbf{L}_N\boldsymbol{\psi}\Big|_{\mathbf{x}_{i0}}\end{bmatrix}\mathbf{C}_i' \tag{3.22}$$

By calculating $\mathbf{C}_i'$ from Eq (3.22) and substituting it in Eq (3.6), one can conclude:

$$\mathbf{u}_i^h(\mathbf{x})=\boldsymbol{\psi}(\mathbf{x})\begin{bmatrix}\mathbf{M}_i\\ \mathbf{L}_N\boldsymbol{\psi}\Big|_{\mathbf{x}_{i0}}\end{bmatrix}^+\begin{pmatrix}\bar{\mathbf{U}}_i^h\\ \mathbf{t}^*-\mathbf{L}_N\mathbf{u}^p\Big|_{\mathbf{x}_i}\end{pmatrix} \tag{3.23}$$

Inputting the local coordinates of the central node and again stating the nodal values, which correspond to the homogeneous part of the solution, in terms of general nodal values results in:

$$\bar{\mathbf{u}}_i-\bar{\mathbf{u}}_i^p=\boldsymbol{\psi}(\mathbf{x}_{i0})\begin{bmatrix}\mathbf{M}_i\\ \mathbf{L}_N\boldsymbol{\psi}\Big|_{\mathbf{x}_{i0}}\end{bmatrix}^+\begin{pmatrix}\bar{\mathbf{U}}_i-\bar{\mathbf{U}}_i^p\\ \mathbf{t}^*-\mathbf{L}_N\mathbf{u}^p\Big|_{\mathbf{x}_i}\end{pmatrix} \tag{3.24}$$

For the sake of simplicity we define $\boldsymbol{\chi}_N^L$ and $\boldsymbol{\chi}_N^R$ as two matrices whose dimensions are equal to $(2n_b \times 2n_R)$ and $(2 \times 2n_b)$, respectively. Where n_R stands for the number of family nodes in the cloud, and we have:

$$\begin{bmatrix} \mathbf{M}_i \\ \mathbf{L}_N \boldsymbol{\psi}\big|_{\mathbf{x}_{i0}} \end{bmatrix}^+ = \begin{bmatrix} \boldsymbol{\chi}_N^L & \boldsymbol{\chi}_N^R \end{bmatrix} \tag{3.25}$$

Finally the relation given in Eq (3.24) with respect to Eq (3.25) can be rewritten as:

$$\bar{\mathbf{u}}_i - \boldsymbol{\psi}(\mathbf{x}_{i0})\boldsymbol{\chi}_N^L \bar{\mathbf{U}}_i = \mathbf{u}^p\big|_{\mathbf{x}_i} - \boldsymbol{\psi}(\mathbf{x}_{i0})\boldsymbol{\chi}_N^L \bar{\mathbf{U}}_i^P + \boldsymbol{\psi}(\mathbf{x}_0)\boldsymbol{\chi}_N^R (\mathbf{t}^* - \mathbf{L}_N \mathbf{u}^p\big|_{\mathbf{x}_i}) \tag{3.26}$$

Similar to the description given for Eq (3.17), Eq (3.26) indicates the relation between the DOFs associated to the central node and those of the family nodes.

Remark III: One can proceed with satisfaction of the traction boundary condition by direct imposition of the traction operator on the approximated function given in Eq (3.14) and find the relation between the family nodes of the cloud, as follows:

$$\mathbf{t}^* = \mathbf{L}_N \boldsymbol{\varphi}\big|_{\mathbf{x}_{i0}} \bar{\mathbf{U}}_i + \mathbf{L}_N \mathbf{u}^p\big|_{\mathbf{x}_{i0}} - \mathbf{L}_N \boldsymbol{\varphi}\big|_{\mathbf{x}_{i0}} \bar{\mathbf{U}}_i^p \tag{3.27}$$

This approach is suggested by the studies presented in [67]. However, since in the fitting process (see Eq (3.10)) the central node is excluded, it results in emerging zero values for some diagonal elements, associated to the traction boundary nodes, in the stiffness matrix of the final system of equations. In other words, Eq (3.27) establishes an algebraic relation between family nodal values in the cloud, and it disregards the central nodal values. On the other hand, utilizing the coupled relation given in Eq (3.24) which leads to Eq (3.26), involves the central nodal values in the algebraic relation, as well. Our experience shows that this new implementation (Eq (3.26)), not only presents better

results in term of accuracy but also makes the condition number of the final system of equation lower. ■

3.6.3 Numerical implementation

Generally, the discretization in peridynamics does not need to be uniform [71], [92]; however, in the case of a non-uniform discretization, especially when the difference between the volumes is large, complicated integration techniques must be used to reduce the integration error which may be computationally costly. In the implementation of peridynamics, the horizon size is commonly taken to be constant to avoid spurious wave reflections and ghost forces between nodes [36]. To this end, using uniform discretization with identical horizon sizes is more convenient from an implementation point of view and for the accuracy of the solution. These limitations could require additional computational tests in the case of problems with complex geometries. However, applying peridynamics only in particular sub-regions where the nonlocal interactions are of concern could be a remedy to address these possible drawbacks.

In the meshless part of the solution since we use the exponential residual free basis functions the method is completely free of any integration. However, proper interpolation of the field variable within a cloud entails considering suitable number of family nodes and efficient selection of the exponent parameters; i.e. $\boldsymbol{\mu}$ in Eq (3.8). This matter is studied comprehensively and addressed in the study done by the author and co-workers recently in [67], and we shall use the same strategy for selecting suitable clouds in the section of numerical examples. In the subsequent section we use 9 nodes for the meshless clouds.

3.7 Numerical examples

In this section, the performance of the proposed approach is examined by considering various 2D examples. For all the examples we choose $E=1$ and $\nu=1/3$; moreover, for the sake of comparison with exact solutions, whenever needed, we shall use the following L^2 relative norms:

$$e_u=\sqrt{\frac{\sum_{i=1}^{N}\left|\mathbf{u}_i^{ex}-\overline{\mathbf{u}}_i\right|^2}{\sum_{i=1}^{N}\left|\mathbf{u}_i^{ex}\right|^2}},\qquad e_\varepsilon=\sqrt{\frac{\sum_{i=1}^{N}\left|\boldsymbol{\varepsilon}_i^{ex}-\overline{\boldsymbol{\varepsilon}}_i\right|^2}{\sum_{i=1}^{N}\left|\boldsymbol{\varepsilon}_i^{ex}\right|^2}} \tag{3.28}$$

in which $\mathbf{u}^{ex}$ and $\boldsymbol{\varepsilon}^{ex}$ stand for the vector of exact displacement and its derivatives, respectively, and N is the total number of nodes in the whole domain. It should be remarked here that the derivatives of the numerically computed displacement fields can be calculated by using a standard finite difference approach.

3.7.1 Example I

This example is devoted to examine in detail the effectiveness of the coupled model through three different parts. A plane stress condition for the problem is assumed. One of the main goals here is to find an optimal value for the ratio $m=\delta/\Delta$; in which Δ is the average nodal spacing of the discretized domain and coincides with the grid spacing in the peridynamic portion of the domain. This ratio plays a crucial role in the quality and accuracy of the numerical solution [33], [91], [93] It should be pointed out that one can find a comprehensive study in [57] for different types of convergence in peridynamics. Choosing a fixed horizon value as δ, one can consider $m=(\delta/\Delta)\to\infty$ by

refining the discretized domain. This convergence is called *m*-convergence in which the numerical solution converges to the exact nonlocal solution for a given δ.

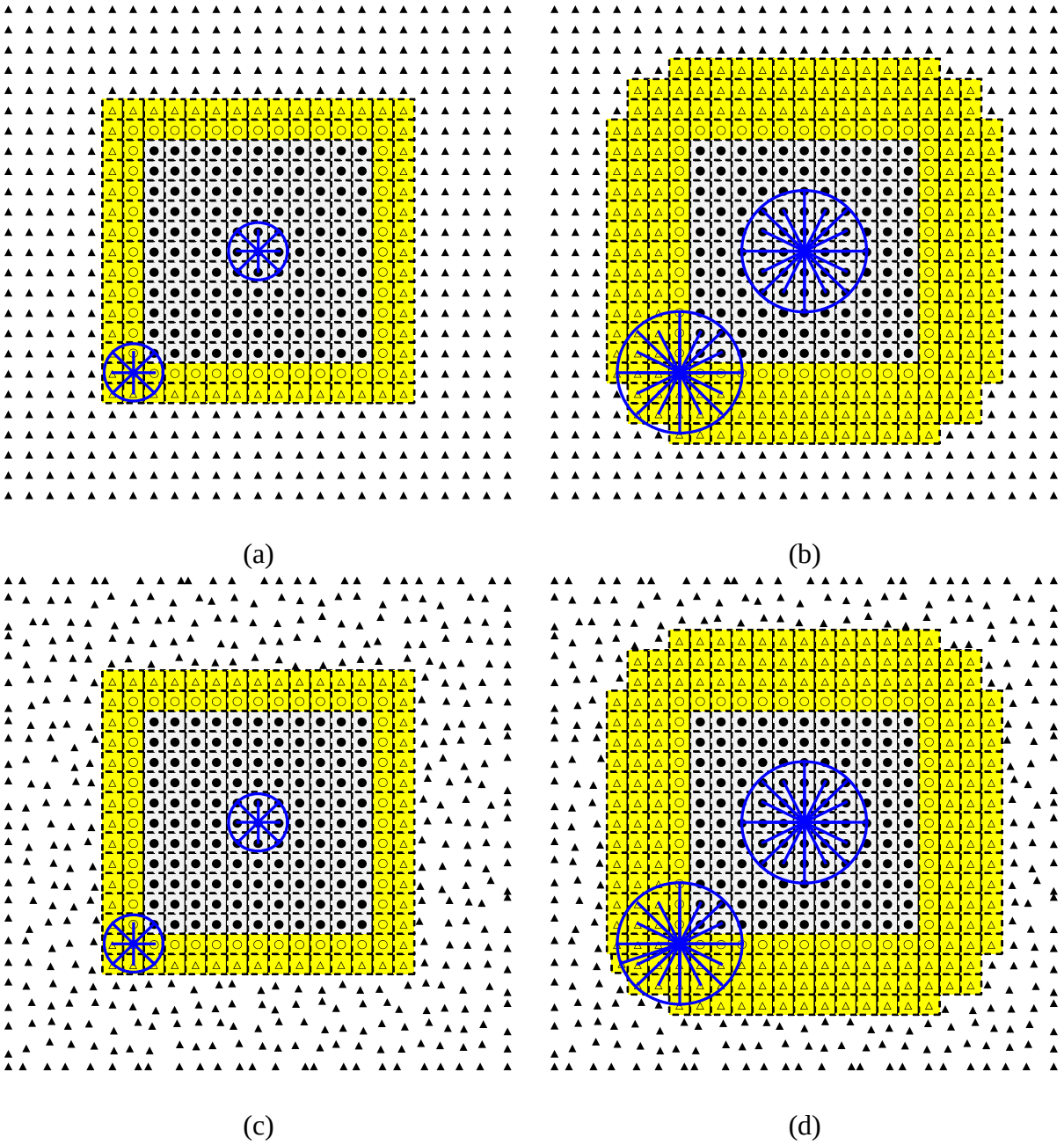

Figure 3.6. Examples of domain discretization used in Example I, regular discretization m equal to (a) $\sqrt{2}$, (b) 3, and irregular discretization m equal to (c) $\sqrt{2}$ and (d) 3.

Another convergence type can be defined, the δ-convergence, by keeping m fixed and again refining the discretized domain which leads to $\delta \to 0$ so that the numerical solution converges to the local classical solution. In this example we use the δ-convergence type to find an optimal value for the m ratio in the coupled approach based on the accuracy and efficiency of the solution.

A square domain $\Omega = (-0.5, 0.5) \times (-0.5, 0.5)$ is the solution domain. Ω_1 the peridynamic region is taken to be the central square of $(-0.25, 0.25) \times (-0.25, 0.25)$. The performance of the proposed method is examined for two different cases of regular and irregular distributions of nodes in the meshless zone, as shown in Figure 3.6, and different values of *m* ratio as $\sqrt{2}$, 2, 3, 4 and 5 as specified in Table 3-1.

Part I. Ghost force test

We begin by testing the coupled approach against ghost forces. In this case we assume $\mathbf{b} \equiv \mathbf{0}$, and Dirichlet boundary conditions are imposed on the boundaries derived from the given rigid body translation:

$$\mathbf{u}_{ex} = (1,1)^T \tag{3.29}$$

We use 625 nodes in total for all the cases. The obtained norms of error for the ghost force test [50] are reported in Table 3-1. The very small norm of the overall error e_u means that even if the displacement conditions are only applied to the boundary of the square domain, all internal points correctly follow the same displacement with a negligible deformation of the translated grid.

Table 3-1. The results obtained for e_u in the ghost force test, rigid body translation, for regular and irregular discretization cases and different values of m ratio.

m	$\sqrt{2}$	2	3	4	5
Irregular discretization	8.54E-09	8.46E-09	8.27E-0.9	7.93E-0.9	7.41E-09
Regular discretization	1.52E-07	3.38E-08	2.20E-08	6.69E-09	6.32E-09

The test can be repeated by considering a rotational rigid body motion as follows:

$$\mathbf{u}_{ex} = \left(x(\cos\theta_d - 1) - y\sin\theta_d, x\sin\theta_d + y(\cos\theta_d - 1) \right)^T, \quad \theta_d = \pi/4 \tag{3.30}$$

The results obtained for the rotational rigid body motion are reported in Table 3-2. The proposed method passes the test properly since the obtained errors are negligible. Therefore, we can state that no ghost forces appear in the proposed coupling scheme.

Table 3-2. The results obtained for e_u in the ghost force test, rigid body rotation, for regular and irregular discretization cases and different values of m ratio.

m	$\sqrt{2}$	2	3	4	5
Irregular discretization	1.72E-08	1.72E-08	1.71E-08	1.68E-08	1.64E-08
Regular discretization	1.56E-08	8.41E-09	1.57E-08	8.08E-09	2.07E-08

Part II. Patch test consistency

In the second part, we test the proposed method for patch test consistency; inspired by the work in [50]. Again $\mathbf{b} \equiv \mathbf{0}$ is assumed, while Dirichlet boundary conditions are imposed on boundaries according to Eq (3.31):

$$\mathbf{u}_{ex} = (x + \frac{1}{2}, \nu\, \mathrm{y} + \frac{1}{2})^T \tag{3.31}$$

The displacements of the inner parts are computed with the coupling approach. The norms of errors for e_u and e_ε in the patch consistency test are reported in Table 3-3.

The results demonstrate that a linear solution is obtained in all cases and hence the model is patch test consistent. The coupled approach performs well to capture the field of derivatives for all the cases with different values of *m* ratio.

Table 3-3. The results obtained for e_u and e_ε in the patch test consistency for regular and irregular discretization cases and different values of m ratio.

m		$\sqrt{2}$	2	3	4	5
Irregular discretization	e_u	5.35E-07	5.35E-07	1.03E-08	8.68E-09	8.44E-09
	e_ε	1.49E-06	1.49E-06	6.92E-07	1.19E-08	1.13E-08
Regular discretization	e_u	8.5E-07	8.05E-09	3.55E-07	1.45E-06	1.3E-08
	e_ε	5.2E-06	4.8E-07	9.45E-07	3.99E-06	1.88E-06

The convergence behavior of the approach must be checked through a δ-convergence study, as well; this is the case for the next part.

Part III. δ-convergence test

The main purpose of this section is to get more insight into the numerical stability of the present approach choosing different values of *m* ratio. In this regard, we consider again a plane stress problem with Dirichlet boundary conditions derived from an exact solution, with higher order of polynomials, as:

$$\mathbf{u}_{ex} = \left(\frac{-1}{3}x^3 y\left(1+\nu\right), \frac{1}{12}[12x^2y^2 + y^4\left(\nu-1\right) - x^4\left(3+\nu\right)]\right)^T \tag{3.32}$$

The monotony and stability of the solution for different values of *m* ratio are reported in Figure 3.7 and Figure 3.8.

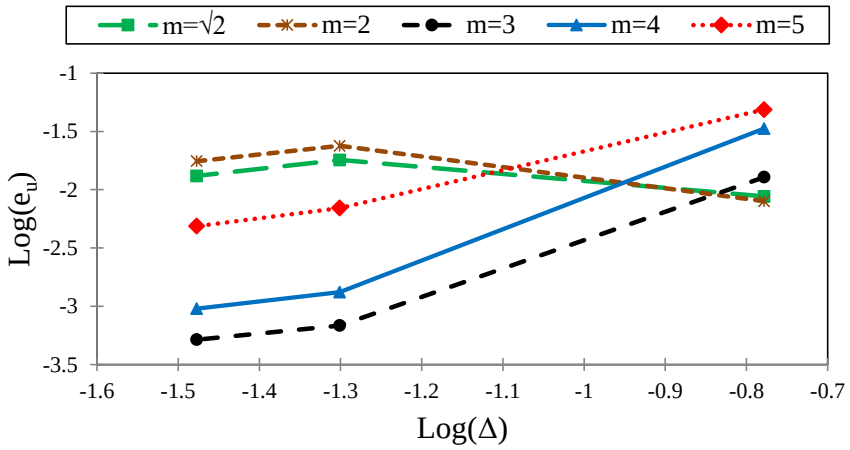

Figure 3.7. δ-convergence test in Example 3.7.1 with different values of m ratio obtained for regular discretization.

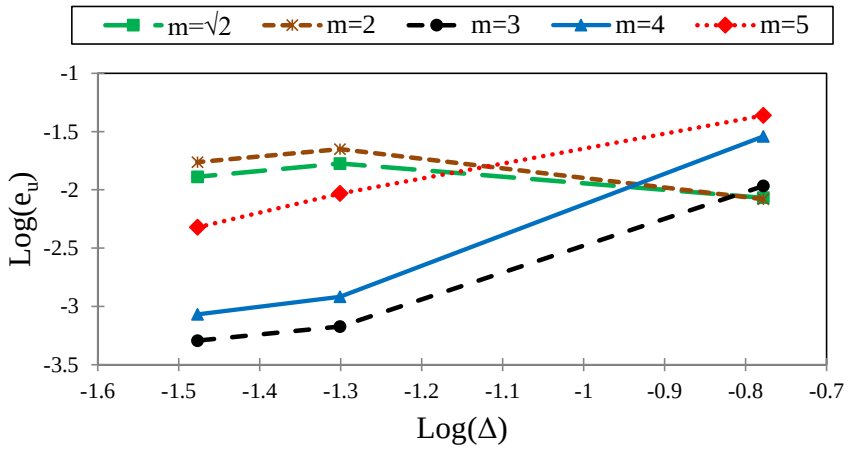

Figure 3.8. δ-convergence test in Example 3.7.1 with different values of m ratio obtained for irregular discretization.

The obtained results reveal that adopting *m* ratios equal to 3, 4 and 5 ($m \geq 3$) contributes to a stable and monotonic solution for the method and refining the discretized domain (δ-convergence) results in more accurate numerical solution whereas adopting the other two *m* ratios, $\sqrt{2}$ and 2, does not guarantee the stability of the numerical solution even though the method performed well with them in the former tests.

In the majority of the studies in peridynamics, the researchers adopt $m \geq 3$ [32], [36], [39], [56], [94]. Furthermore, based on the investigations in [32], [36] values less than 3 for the *m* ratio result in undesirable pollution of error in the dynamic fracture problems [95], [96], and larger values may result in larger computational time and cost. Taking into account the results obtained in the three parts of this example we take *m*=3 for the remaining examples.

3.7.2 Example II

In this example we aim at demonstrating one of the most important advantages of the proposed approach which corresponds to the elimination of the surface effect

described in Section 3.3. In this regard, we consider a 2D plane stress problem as shown in Figure 3.9. Both Dirichlet (clamped vertical edges) and Neumann (normal tractions of $q = 1$ on the horizontal edges) boundary conditions are applied to the domain.

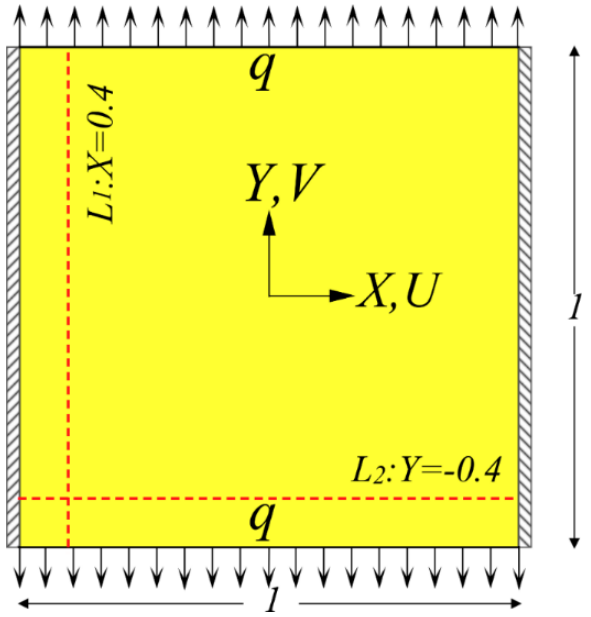

Figure 3.9. The problem domain in Example II.

The problem is solved with two types of discretizations named Coupled I and Coupled II shown in Figure 3.10. In the case of Coupled I, the transition zone is smaller than the optimal size proposed earlier. The horizon of some peridynamic nodes are not entirely contained in the transition zone. In this case the largest possible area is discretized with the peridynamic model and MLEBF is used only for the purpose of boundary condition satisfaction. In the Coupled II case, we widen the transition part so that all the horizons of the peridynamic nodes are completely embedded inside the transition region. In the case of Coupled I, as the thickness of the transition region is narrow and it consists only of two rows of meshless nodes, considering m=3, no pure meshless node appears in the solution.

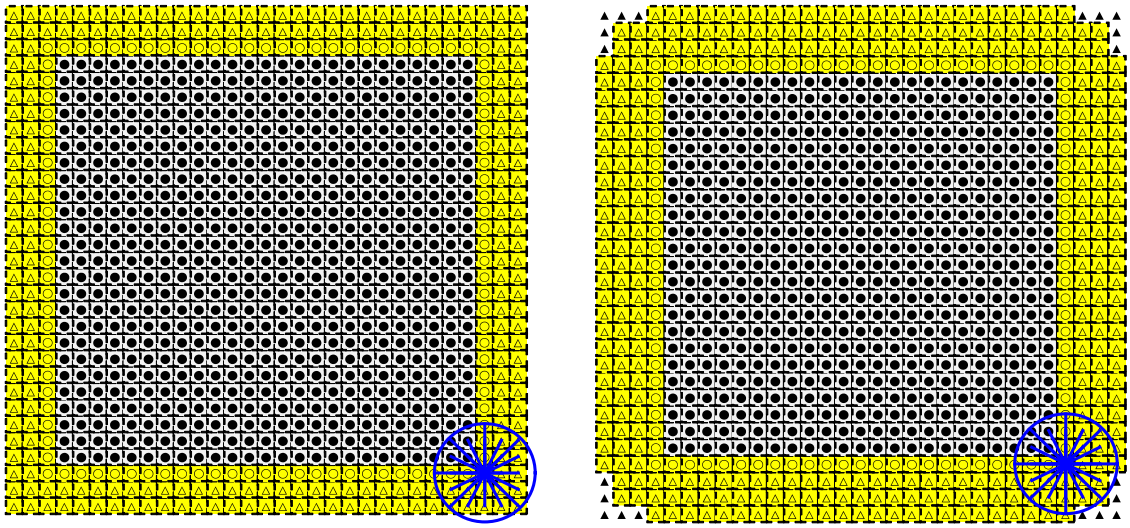

(a) (b)

Figure 3.10. Two different types of discretization for the present method using 961 nodes (a) Coupled I and (b) Coupled II in Example II.

The problem is solved as well by using a peridynamic grid with two different discretizations named as Peridynamic I and Peridynamic II. In Peridynamic I we use again 961 nodes and in Peridynamic II we use 14641 nodes which is approximately 15 times more than in the other case.

All solutions are finally compared with a FEM plane stress solution using 100 equal linear rectangular elements which is considered the reference solution.

In Figure 3.11 and Figure 3.12 the displacement components and their derivatives along the two lines L_1 and L_2, shown in Figure 3.9, are presented.

As can be seen the surface effect is more pronounced for Peridynamic I which uses a much coarser grid of nodes compared to Peridynamic II. It can be concluded that the convergence of the solution to FEM is achieved slowly in the peridynamic case and this problem originates mainly from the surface effect. However, in the Coupled I case with

the same coarse distribution of nodes as in Peridynamic I, the surface effect is virtually eliminated and the solution converges to that of FEM more quickly. Moreover, the solution of Coupled II, still using only 961 nodes but satisfying the 'transition region criterion' is in complete agreement with that of FEM.

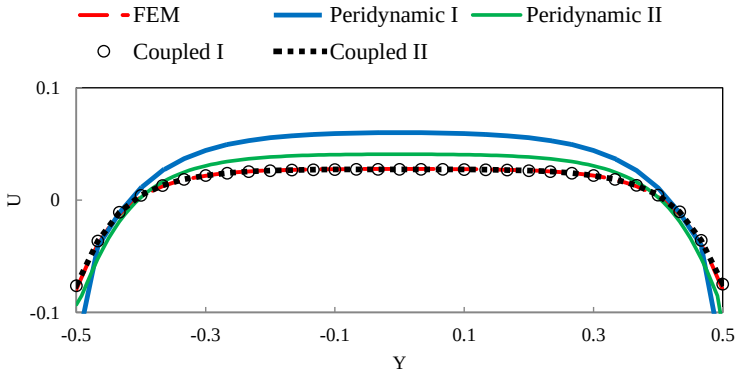

(a)

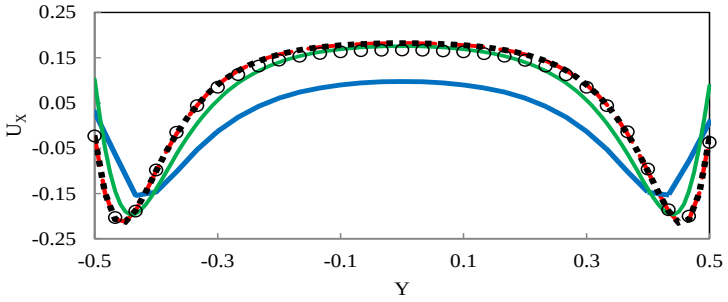

(b)

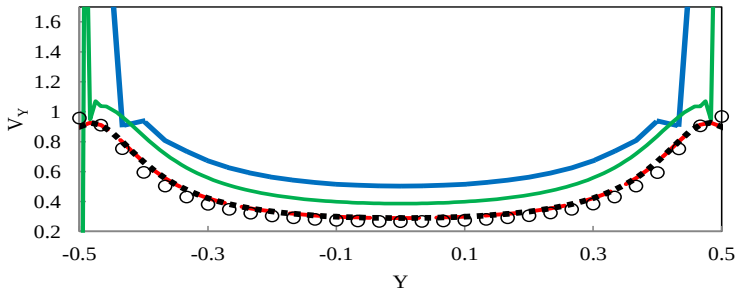

(c)

Figure 3.11. Comparison of results obtained by different approaches along L_1 in Example II (a) U , (b) $\partial U/\partial X$ and (c) $\partial V/\partial Y$ in Example II.

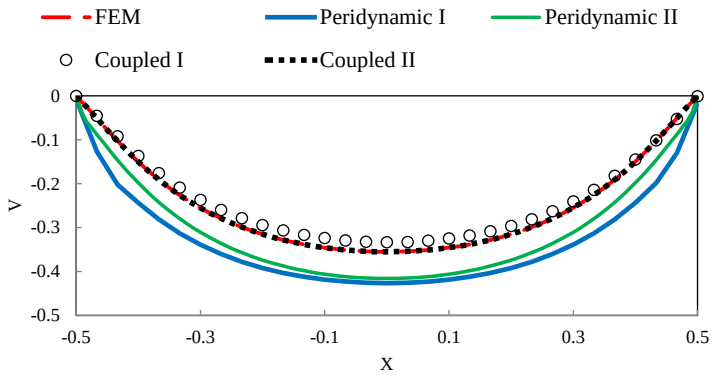

(a)

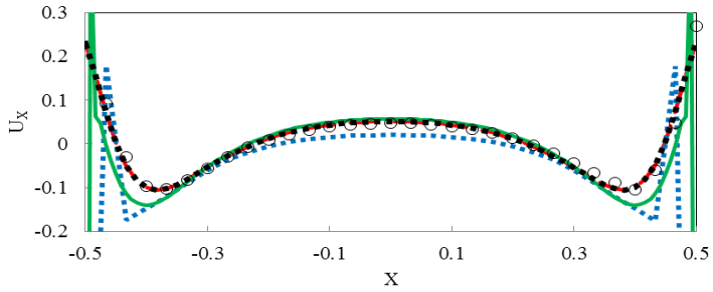

(b)

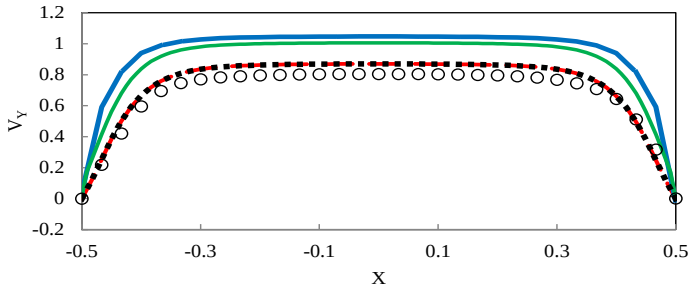

(c)

Figure 3.12. Comparison of results obtained by different approaches along L_2 in Example II (a) U , (b) $\partial U/\partial X$ and (c) $\partial V/\partial Y$ in Example II.

3.7.3 Example III

The main objective in this example is to show that the present method can be applied to problems with discontinuities (such as cracks), taking full advantage of

peridynamics. This example is a preliminary study in which a crack is present, but it does not propagate. However, the possibility to apply the present approach to static and dynamic crack propagation will be investigated later. In this example we use the peridynamic discretization around the discontinuous parts of the domain and where the existing crack could propagate. Where the solution remains smooth, classical elasticity in the framework of MLEBF is employed to exploit the full advantages of both models.

A cracked plate is considered which is subjected to an opening tension as shown in Figure 3.13. The plate is part of a semi-infinite domain subject to a traction in the Y direction at infinity. In this example, we have applied the exact displacement components to the boundary of the truncated domain and the current method is used to evaluate the displacements of the inner part. The corresponding analytical solution is as follows [97]:

$$\mathbf{u}_{ex} = \frac{K_I(1+\nu)}{E}\sqrt{\frac{r}{2\pi}}\left(\cos\frac{\theta}{2}(\kappa-1+2\sin^2\frac{\theta}{2}),\sin(\frac{\theta}{2})(\kappa+1-2\cos^2\frac{\theta}{2})\right)^T \tag{3.33}$$

where K_I is the stress intensity factor and κ is the bulk modulus.

Figure 3.14 shows that the problem is solved with two different approaches: the domain is fully discretized with a peridynamic grid or with the coupled approach proposed in the present work. As shown in Figure 3.14(b), representing the crack in peridynamics is convenient as it suffices to break the bonds that intersect the crack line.

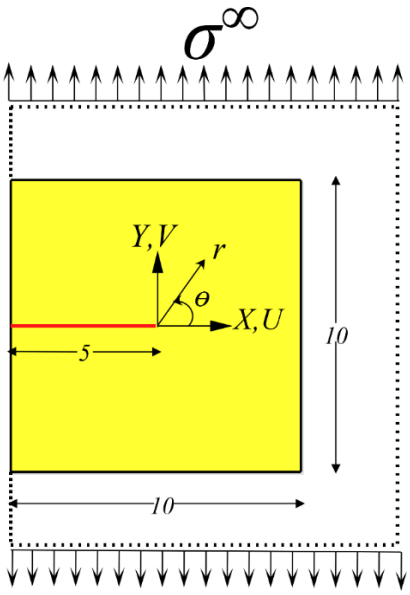

Figure 3.13. Cracked square plate subjected to opening tension boundary condition in Example III.

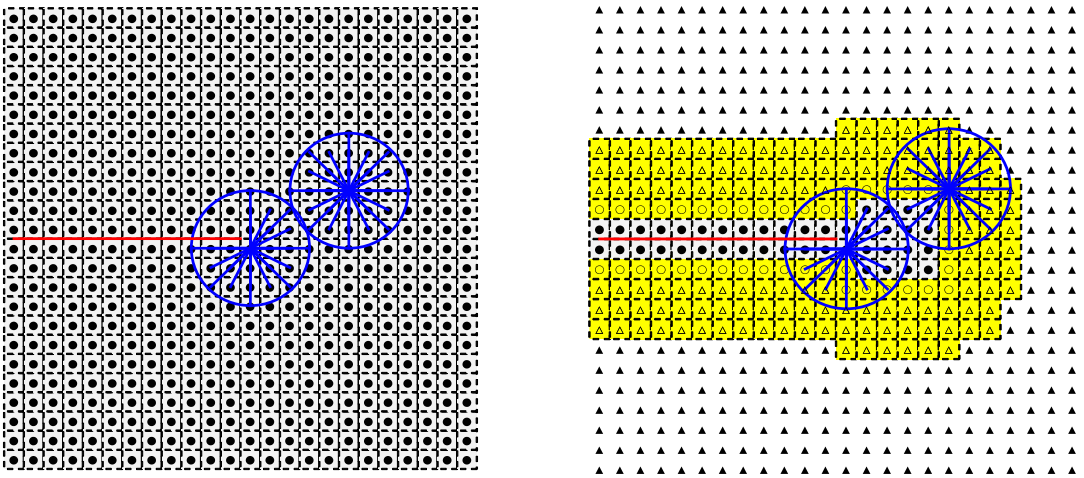

(a) (b)

Figure 3.14. Samples of domain discretization for (a) peridynamic and (b) coupling method in Example III.

Figure 3.15 shows the contour plots of the displacement field components in the vertical and horizontal directions obtained by the exact solution; moreover, in the same figure the

results obtained by the present method using 1156 nodes are included. The agreement between the two figures is excellent in the whole domain, even close to the crack tip.

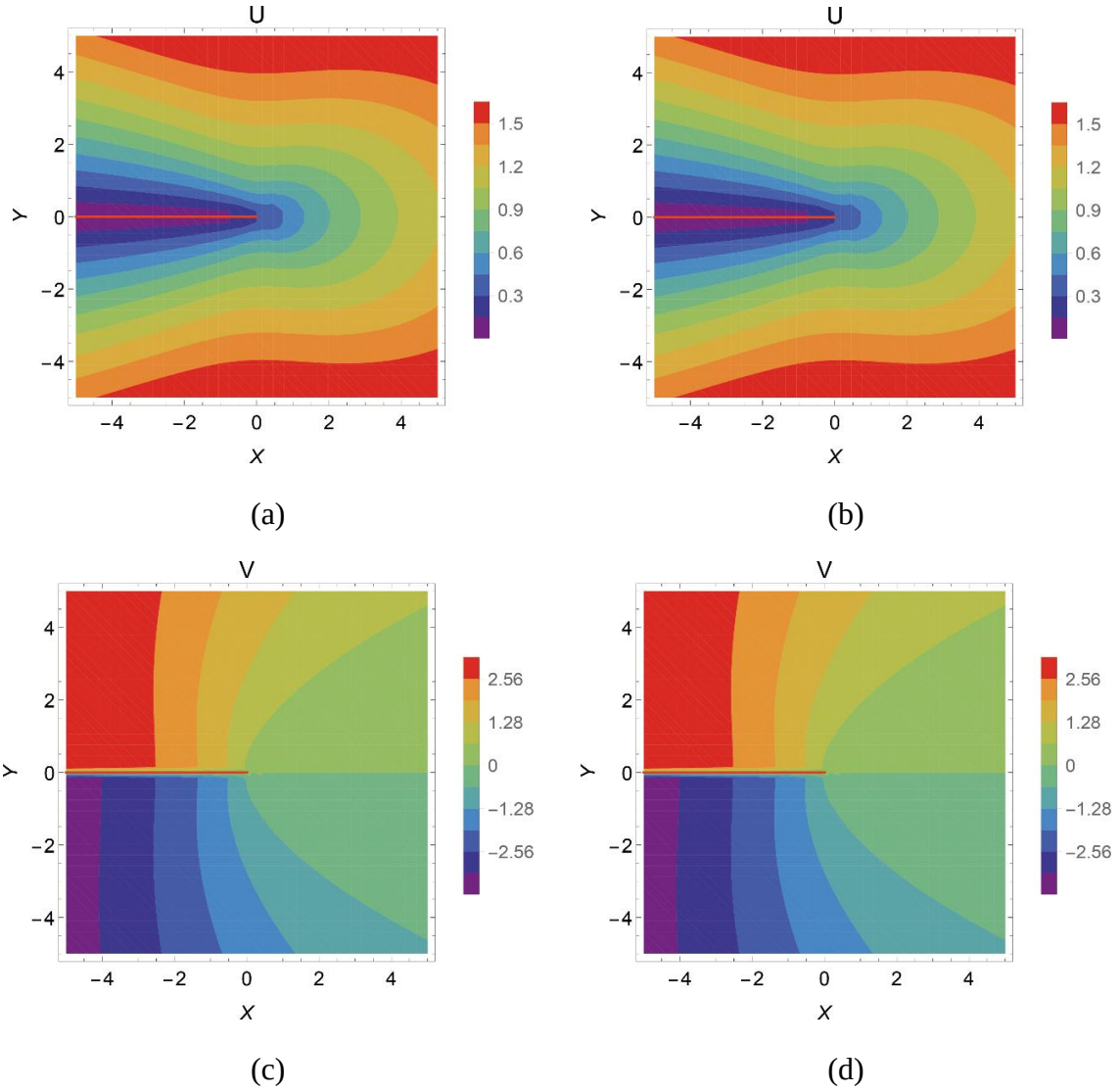

Figure 3.15. Contour plots of the solution for U obtained by (a) the exact solution, (b) present method, and for V obtained by (c) the exact solution and (d) present method in Example 3.

For a comparative study we use 7056 nodes for the peridynamic model. For both the implemented strategies the contour plots of the difference between the numerical solution

and the exact solution are shown in Figure 3.16. It is apparent that the results obtained by the present approach outperforms those of the pure peridynamic model in terms of accuracy by using a much smaller number of nodes in the solution domain. The present approach takes advantage of the positive features of both computational techniques; the cracked region is conveniently simulated with peridynamics.

For further investigation, we repeat the simulation by using the same number of 7056 nodes for the coupled approach same as the pure peridynamic model. The counter plots of the absolute difference of the numerical solutions with respect to the exact solution are presented in Figure 3.17.

It should be remarked here that using the same number of nodes in the present method produces highly accurate results with lower distribution of error in the computational domain compared to a peridynamic model. To elucidate more, e_u is obtained as 0.0057, and it is 3.2 times less than the error obtained by peridynamics which is 0.0182.

Figure 18 shows how the numerical solution converges to the exact solution for both strategies. The present method yields more accurate results in comparison to the peridynamic model and converges to the exact solution monotonically and more quickly.

Figure 3.18 shows how the numerical solution converges to the exact solution for both strategies. Finally it is right to observe as well that the application of the MLEBF only in the form presented here would not provide good results because its application to the region affected by the singularity at the crack tip would be inaccurate.

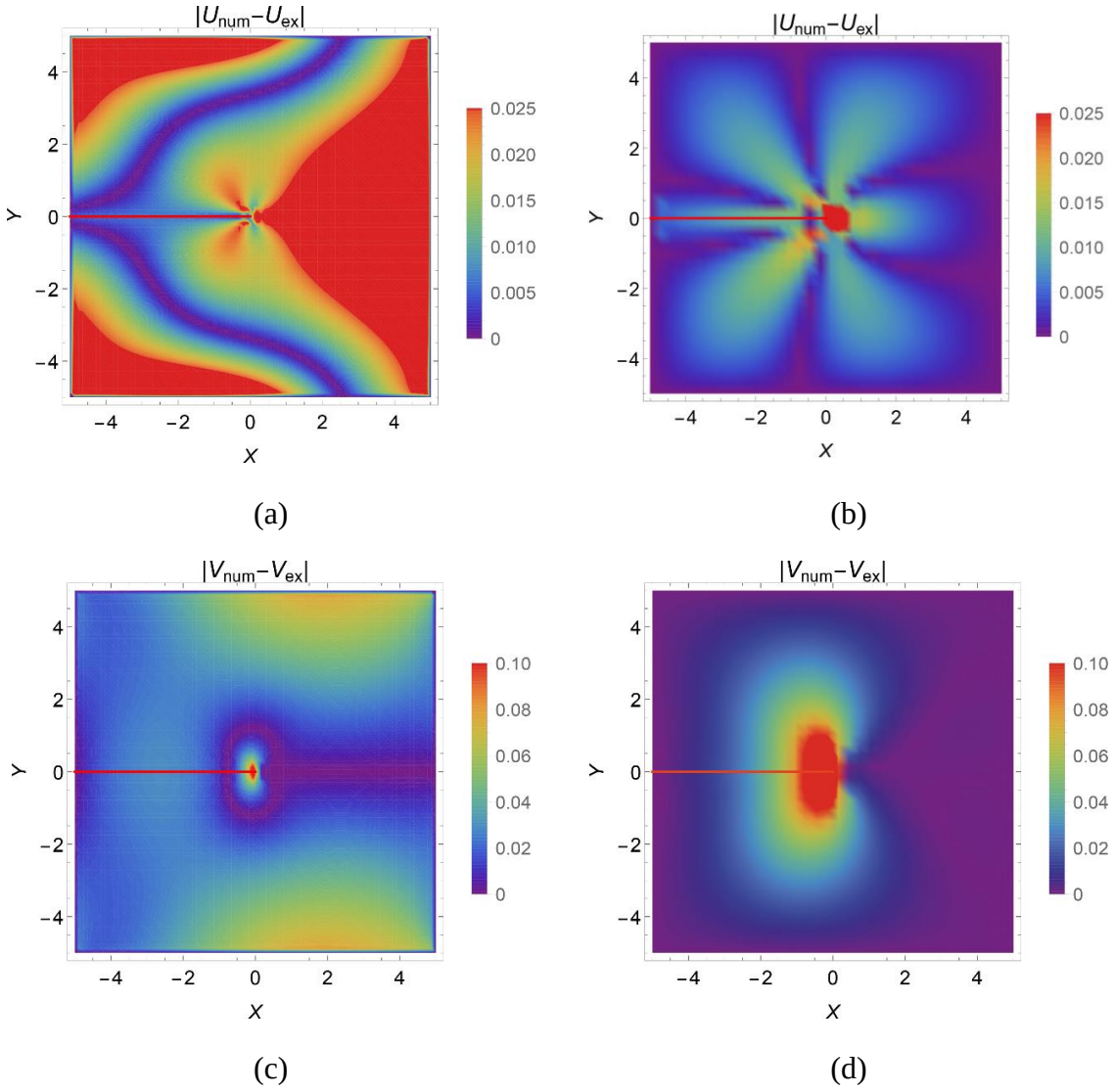

Figure 3.16. Contour plots of absolute difference between numerical results and exact solution (a) and (c) are obtained by peridynamic using 7056 nodes, (b) and (d) are obtained by the present method using 1156 nodes in Example III.

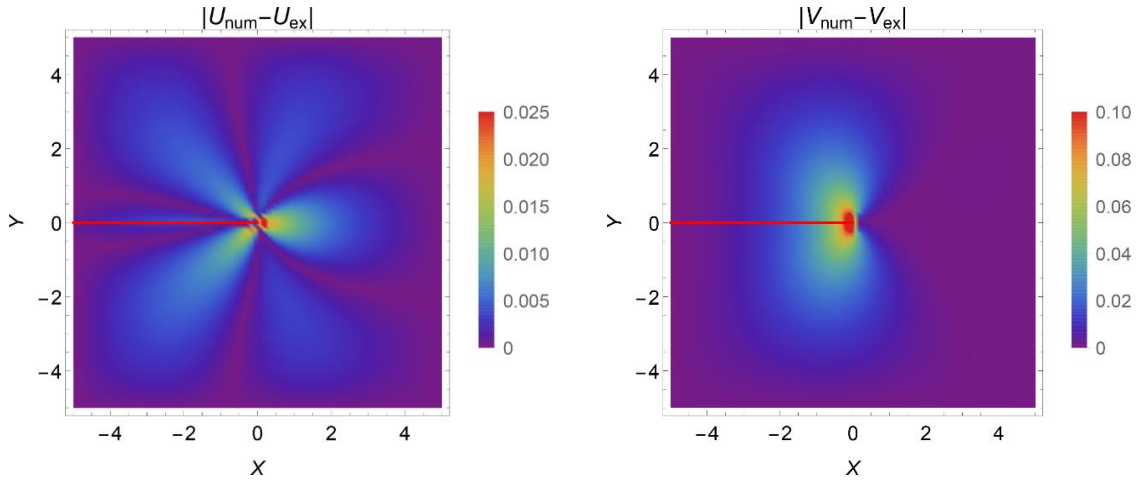

Figure 3.17. Contour plots of absolute difference between numerical results and exact solution in (a) horizontal and (b) vertical directions obtained by the present method using 7056 in Example III.

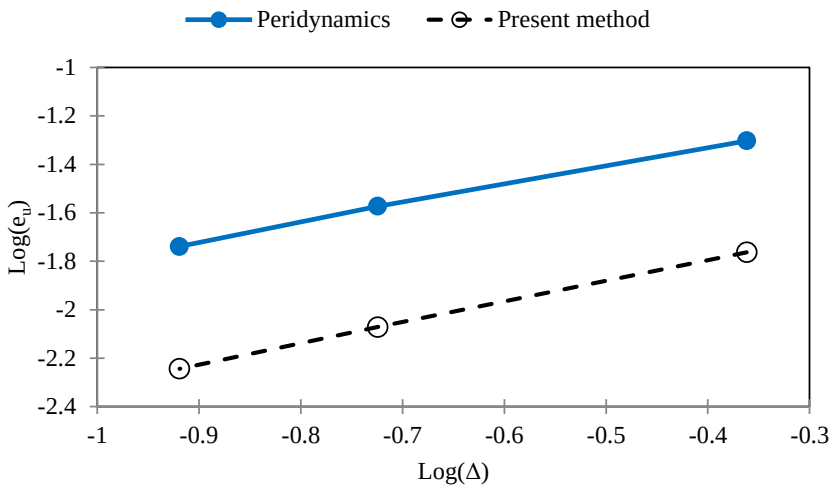

Figure 3.18. Convergence of the numerical solution to the exact solution in Example III.

4. The meshless finite point method for transient elastodynamic problems

4.1 Introduction

Depending on how equations are discretized, meshless methods can be classified into two major categories. The first category constitutes meshless methods based on weak forms such as the element-free Galerkin method [98]. Most of them are only meshless in terms of the numerical approximation of field variables, and they are involved with numerical integration using a background mesh over the problem domain; which makes them computationally expensive and not '*truly*' meshless.

The second category are meshless methods based on the strong-form such as the finite point method (FPM) [99]. These methods often use the point collocation method to satisfy the governing differential equations, or they do the approximation using basis functions which satisfy the governing differential equation as in [76]. Since they do not need any background mesh, they are truly meshless, simpler to implement, and computationally less expensive than meshless methods based on weak forms.

The meshless finite point method (FPM) proposed by Oñate et al.[99] is a notable method within the context of truly meshless methods. The application of the method to the solution of static elasticity problems can be found in [68]. FPM uses a weighted least squares (WLS) scheme for approximating the unknown field function. The approximation can be easily constructed to have a consistency of a desired order, and by

adopting the point collocation method the discrete equations can be obtained. FPM has received considerable attention in different studies and applications; see for example [100]–[106].

However, strong form-based methods such as FPM, in comparison with weak form-based methods, are most often less stable and accurate for problems governed by partial differential equations with Neumann (derivative) boundary conditions such as solid mechanics problems with stress (natural) boundary conditions. These methods fall within a category of methods called direct meshless collocation methods [107]. In such type of methods, Neumann boundary conditions should be imposed directly through a series of independent equations, which are different from the governing equations in the problem domain. This contributes to a poor accuracy on Neumann boundaries, and it may be taken as the main source of instability for collocation methods [108], [109]. In this regard, several studies by different researchers have been proposed to circumvent this deficiency. Oñate [110] and Oñate et al. [68] proposed a stabilized version of FPM using finite calculus (FIC). A simple modification to stabilize FPM using FIC was proposed by Boroomand et al. [111]. Shu et al. [112] used several layers of orthogonal grids near and on the boundaries for proper satisfaction of Neumann conditions. La Rocca and Power [113] introduced a double-boundary collocation Hermitian technique in which at the boundary collocation points the governing differential equations and the boundary conditions are coupled and satisfied simultaneously. Liu and Gu [114] and Liu et al. [115] proposed a combined formulation that benefits from both the local weak form and strong form equations. In this sense, the strong form formulation is applied to all nodes whose local support domains do not intersect with Neumann boundaries, while the

application of weak form formulation is restricted to nodes on or near the Neumann boundaries. Pursuing such an idea, Sadeghirad and Mohammadi [107], [116] proposed the equilibrium on line method (ELM) for imposition of Neumann boundary conditions in FPM using straight line integration domains.

Dynamic analysis of elastic structures is an important issue in various areas of engineering. The solution of such problems with meshless methods is still the subject of different studies in the literature as in [117]. In this chapter, the application of FPM to elastodynamic problems is investigated. Here the main attempt is to extend the solution of FPM in time for elasticity problems while keeping all its main advantages in terms of efficiency and simplicity of implementation. In this way, for the nodes in the body the time marching is performed by using an explicit velocity–Verlet time integration method. Moreover, for the nodes located on Neumann boundaries a simple technique is introduced to update the nodal displacements of the boundary nodes by the solution of a set of linear equations in time. This system of equations includes Neumann boundary nodes as well as all the adjacent nodes that fall within their support domains. The displacements of the nodes on Neumann boundaries are updated at each time step, simultaneously, by a set of equilibrated equations that correspond to body nodes that are consistent with the governing equation of the body itself. This strategy makes the solution to proceed in time appropriately. The formulation is thoroughly explained; moreover, a short technical description on implementation of the work in an Open Multi-Processing application programming interface (OpenMP) is discussed. We shall show that the proposed technique preserves the appealing features of FPM from the implementation point of view. We shall assess the accuracy of the method through some benchmark

examples including some 3D dynamic problems. To the best of the author knowledge, reference [118] (on which this chapter is based) is the first study on the application of FPM to the solution of 3D elastodynamic problems.

4.2 Problem description

Consider a linear elastic body in a three dimensional domain Ω bounded by a boundary Γ consisting of a Dirichlet part Γ_D constrained by prescribed displacements $\mathbf{u}^*$ and a Neumann part Γ_N where prescribed tractions $\mathbf{t}^*$ are imposed (see Figure 4.1).

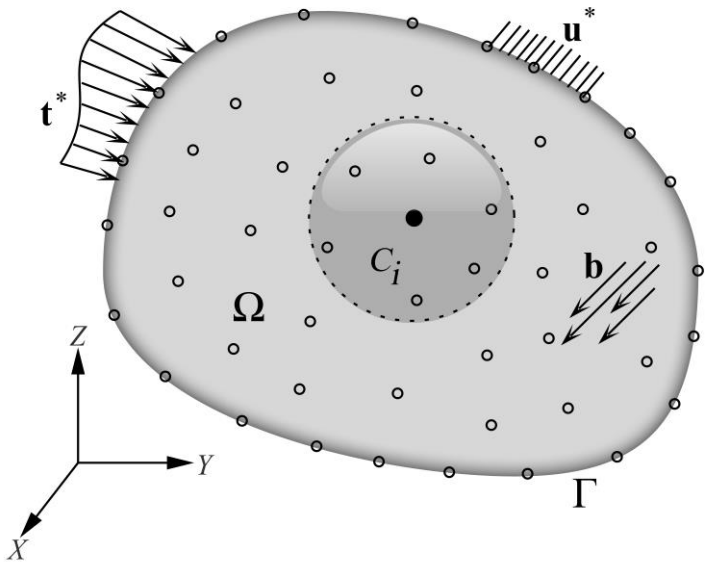

Figure 4.1. Domain representation of a general three-dimensional problem in a meshless style.

In an isotropic homogenous medium for any point of the domain Ω the governing equations of motion, at time t, can be written in the following form:

$$\mathbf{S}^T\mathbf{DSu}(\mathbf{X},t)+\mathbf{b}(\mathbf{X},t)=c_d\dot{\mathbf{u}}(\mathbf{X},t)+\rho\ddot{\mathbf{u}}(\mathbf{X},t),\qquad \mathbf{X}\in\Omega \tag{4.1}$$

with prescribed boundary conditions:

$$\tilde{\mathbf{n}}\mathbf{DSu}(\mathbf{X},t)+\mathbf{b}=\mathbf{t}^*(\mathbf{X},t),\qquad \mathbf{X}\in\Gamma_N \tag{4.2}$$

$$\mathbf{u}(\mathbf{X},t) = \mathbf{u}^{*}(\mathbf{X},t), \qquad \mathbf{X} \in \Gamma_D \tag{4.3}$$

and initial displacement and velocity conditions:

$$\mathbf{u}(\mathbf{X},0) = \mathbf{u}_0(\mathbf{X}), \qquad \mathbf{X} \in \Omega \tag{4.4}$$

$$\dot{\mathbf{u}}(\mathbf{X},0) = \mathbf{v}_0(\mathbf{X}), \qquad \mathbf{X} \in \Omega \tag{4.5}$$

where c_d represents the damping coefficient. $\mathbf{S}$ is the well-known elasticity operator defined as:

$$\mathbf{S}^T = \begin{bmatrix} \partial/\partial x & 0 & 0 & \partial/\partial y & 0 & \partial/\partial z \\ 0 & \partial/\partial y & 0 & \partial/\partial x & \partial/\partial z & 0 \\ 0 & 0 & \partial/\partial z & 0 & \partial/\partial y & \partial/\partial x \end{bmatrix} \tag{4.6}$$

and $\mathbf{D}$ is the matrix of material constants defined by:

$$\mathbf{D} = \begin{bmatrix} D_1 & D_2 & D_2 & 0 & 0 & 0 \\ & D_1 & D_2 & 0 & 0 & 0 \\ & & D_1 & 0 & 0 & 0 \\ & & & D_3 & 0 & 0 \\ & & & & D_3 & 0 \\ \text{Sym.} & & & & & D_3 \end{bmatrix} \tag{4.7}$$

the parameters in the above equation are defined as:

$$(D_1, D_2, D_3) = \frac{E}{(1+\nu)(1-2\nu)}(1-\nu, \nu, (1-2\nu)/2) \tag{4.8}$$

$\tilde{\mathbf{n}}$ is a matrix containing n_x, n_x, and n_z which are the components of the outward unit vector normal to the boundary, defined as:

$$\tilde{\mathbf{n}} = \begin{pmatrix} n_x & 0 & 0 & n_y & 0 & n_z \\ 0 & n_y & 0 & n_x & n_z & 0 \\ 0 & 0 & n_z & 0 & n_y & n_x \end{pmatrix} \tag{4.9}$$

4.3 The solution strategy

4.3.1 Approximation scheme

Here, we recall the weighted least square (WLS) approximation scheme employed for FPM, one may consult [68] to get more insight into the details of the formulation. Let $\mathbf{X}_i \in \Omega,\ i = 1,2,\ldots$ be a collection of nodes scattered within the solution domain and on the boundaries (see Figure 4.1). Accordingly, the time is discretized into instants as $t_1, t_2, \ldots t_n, t_{n+1}, \ldots$. Similar to the MLEBF method, around each of the nodes a subdomain C_i, so called cloud, is considered. Each subdomain has a local coordinate system with origin on the node. C_i contains the neighboring nodes of $\mathbf{X}_i$ as $\mathbf{x}_j$, $j = 1,2,\ldots,n_i$ over which a displacement variable, to exemplify u at time step t_n can be approximated by $\hat{u}^n$ locally as:

$$\hat{u}^n(\mathbf{x}) = \sum_{j=1}^{n_b} p_j(\mathbf{x})\alpha_j^n = \mathbf{p}^T(\mathbf{x})\boldsymbol{\alpha}^n, \qquad \mathbf{x} \in C_i \tag{4.10}$$

where $\mathbf{x} = (x, y, z)$ stands for the local coordinate system, $\mathbf{p}(\mathbf{x})$ indicates a vector consisting of n_b number of monomial bases, and $\boldsymbol{\alpha}$ is a vector of unknown coefficients to be found in terms of nodal values.

Considering a complete set of monomials, for a 3D problem one can specify $\mathbf{p}$; for instance, as:

$$\mathbf{p} = (1, x, y, z, x^2, xy, y^2, yz, zx, z^2)^T, \qquad n_b = 10 \tag{4.11}$$

To proceed with the approximation, u can be sampled at the n_i neighboring nodes of C_i as:

$$\bar{\mathbf{u}}^n = \begin{pmatrix} \bar{u}_1^n \\ \bar{u}_2^n \\ \vdots \\ \bar{u}_{n_i}^n \end{pmatrix} \approx \begin{pmatrix} \hat{u}_1^n \\ \hat{u}_2^n \\ \vdots \\ \hat{u}_{n_i}^n \end{pmatrix} = \begin{bmatrix} \mathbf{p}^T(\mathbf{x}_1) \\ \mathbf{p}^T(\mathbf{x}_2) \\ \vdots \\ \mathbf{p}^T(\mathbf{x}_{n_i}) \end{bmatrix} \boldsymbol{\alpha}^n = \mathbf{C}\boldsymbol{\alpha}^n \tag{4.12}$$

$\mathbf{C}$ is regarded as the moment matrix associated to the local approximation within C_i. Assuming $n_i > n_b$, then $\mathbf{C}$ is not a square matrix; in turn, the approximation cannot fit to all the values of $\bar{\mathbf{u}}^n$. Likewise, the approximation entails a WLS procedure that results in a minimization of a norm *J* as follows:

$$J = \sum_{j=1}^{n_i} w(r_j)(\bar{u}_j^n - \hat{u}(x_j^n))^2 = \sum_{j=1}^{n_i} w(r_j)(\bar{u}_j^n - \mathbf{p}^T(\mathbf{x}_j)\boldsymbol{\alpha}^n)^2 \tag{4.13}$$

where $r_j = |\mathbf{x}_j|$ and w is a weight function that should be taken suitably for C_i. In this work, we take as suggested in [111]:

$$w(r_j) = \frac{1 - \exp(64 - 16\, r_j^{\,2} / r_m^{\,2})}{1 - \exp(64)} \tag{4.14}$$

where r_m indicates the distance of the most remote node of the cloud from the central node. Minimization of the norm *J* in Eq (4.13) with respect to $\boldsymbol{\alpha}^n$ yields the following system of equations:

$$\mathbf{A}\boldsymbol{\alpha}^n = \mathbf{B}\bar{\mathbf{u}}^n \tag{4.15}$$

where

$$\mathbf{A} = \sum_{j=1}^{n_i} w(r_j)\mathbf{p}(\mathbf{x}_j)\mathbf{p}^T(\mathbf{x}_j) \tag{4.16}$$

and

$$\mathbf{B} = \begin{bmatrix} w(r_1)\mathbf{p}(\mathbf{x}_1) & w(r_2)\mathbf{p}(\mathbf{x}_2) & \cdots & w(r_{n_i})\mathbf{p}(\mathbf{x}_{n_i}) \end{bmatrix} \tag{4.17}$$

$\boldsymbol{\alpha}^n$ can be found from Eq (4.15) as follows :

$$\boldsymbol{\alpha}^n = \mathbf{A}^{-1}\mathbf{B}\bar{\mathbf{u}}^n \tag{4.18}$$

Finally, $\hat{u}^n(\mathbf{x})$ can be obtained in terms of nodal values, by substitution of $\boldsymbol{\alpha}^n$ from Eq (4.18) into Eq (4.10) which gives:

$$\hat{u}^n(\mathbf{x}) = \mathbf{p}^T(\mathbf{x})\mathbf{A}^{-1}\mathbf{B}\bar{\mathbf{u}}^n = \sum_{j=1}^{n_i} N_j(\mathbf{x})\bar{u}_j^n \tag{4.19}$$

where N_j stands for the j[th] shape function.

4.4 Discretization of governing equations

The discretized system of equations in FPM can be easily obtained by substituting the approximated functions of displacements $\mathbf{u}^n(\mathbf{x}) = (\bar{u}^n(\mathbf{x}), \bar{v}^n(\mathbf{x}), \bar{w}^n(\mathbf{x}))^T$, from Eq (4.19), in Eqs (4.1)-(4.3) which results in:

$$(\mathbf{S^T DSN})\Big|_{\mathbf{X}_i} \mathbf{u}_R^n + \mathbf{b}_i^n = \rho\ddot{\mathbf{u}}_i^n + c_d\dot{\mathbf{u}}_i^n, \quad \mathbf{X}_i \in \Omega \tag{4.20}$$

where $\mathbf{u}_R^n = (\bar{u}_1^n, \bar{v}_1^n, \bar{w}_1^n, \bar{u}_2^n, \bar{v}_2^n, \bar{w}_2^n, \ldots, \bar{u}_{n_i}^n, \bar{v}_{n_i}^n, \bar{w}_{n_i}^n)^T$, is the vector of nodal displacements in the cloud, and $\mathbf{N}$ is the matrix of shape functions as follows:

$$\mathbf{N} = \begin{bmatrix} N_1 & 0 & 0 & N_1 & 0 & 0 & \cdots \\ 0 & N_1 & 0 & 0 & N_2 & 0 & \cdots \\ 0 & 0 & N_1 & 0 & 0 & N_2 & \cdots \end{bmatrix} \tag{4.21}$$

Consequently, for the Neumann boundary nodes one can conclude:

$$\mathbf{t}^*(\mathbf{X}_i, t^n) = (\tilde{\mathbf{n}}\mathbf{DSN}^T)\Big|_{\mathbf{X}_i} \mathbf{u}_R^n, \quad \mathbf{X}_i \in \Gamma_N \tag{4.22}$$

4.5 Time integration and boundary condition satisfaction

In the present work, the time integration in Eq (4.20) is carried out based on an explicit velocity-Verlet scheme described in Section 2.9.2. In this study, we take the constant time step Δt less than the critical time step Δt_{crit} as below:

$$\Delta t_{crit} = \Delta_{\min} / c_k \tag{4.23}$$

where $\Delta_{\min}$ is the minimum nodal distance in the discretized domain, and c_k is the maximum speed of sound in the material. In turn, Δt must be chosen so that:

$$\Delta t \le \Delta_{\min} \sqrt{\frac{3(1-\nu)\rho}{E}} \tag{4.24}$$

Having known the displacement and velocity vectors of each node at time step *n*, the displacement vector at the next time step can be found as:

$$\mathbf{u}^{n+1} = \mathbf{u}^n + \Delta t \dot{\mathbf{u}}^n + \frac{\Delta t^2}{2} \ddot{\mathbf{u}}^n \tag{4.25}$$

and hence for the DOFs inside the domain one may easily determine $\ddot{\mathbf{u}}^{n+1}$ at each time step from Eq (4.20) and find $\mathbf{u}^{n+1}$. However, for nodes exposed to Neumann boundary conditions progression in time cannot be reached by using Eq (4.25). This is due to the fact that for these nodes the acceleration term does not appear directly in Eq (4.22); therefore, a suitable strategy to manage such a problem should be devised.

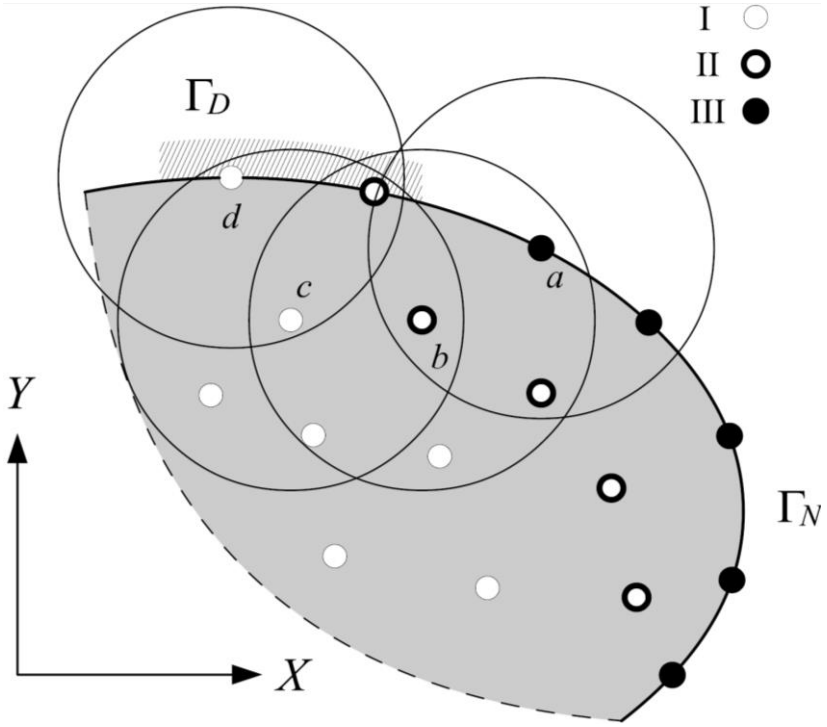

Figure 4.2. The boundary of a generic discretized problem domain.

We explain the solution strategy for a general 2D problem as shown in Figure 4.2. “c” and “b” are two body nodes, “a” and “d” are two boundary nodes with Neumann and Dirichlet condition, respectively. For the sake of brevity, we assume that at each boundary node prescribed boundary conditions are of either Dirichlet or Neumann type; the generalization to 3D problems as well as nodes with mixed boundary condition can be done easily. Figure 4.2 represents a small portion of a generic discretized body close to its boundary. The distributed nodes, based on their position in the solution domain, are classified into three types as I, II and III. Type I stands for the nodes whose cloud do not contain any node with Neumann boundary condition (“c” and “d”). Type II (“b”) represents the nodes whose clouds contain at least a node with Neumann boundary condition, and Type III (node “a”) are the nodes located on Neumann boundaries. It can

be concluded that Type II nodes play the role of an interface layer of nodes between Neumann boundaries and the other parts of the body.

The displacement vectors for types I and II nodes (excluding Dirichlet nodes) at time step $n+1$ can be found explicitly. It suffices to obtain the vector of acceleration at time step *n* by using Eq (4.20) and advancing to the next step using Eq (4.25). To exemplify, for nodes "c" and "b" one can write:

$$\mathbf{u}_b^{n+1} = \mathbf{u}_b^n + \cdots + \boldsymbol{\psi}_{ba}\mathbf{u}_a^n + \boldsymbol{\psi}_{bb}\mathbf{u}_b^n + \boldsymbol{\psi}_{bc}\mathbf{u}_c^n + \cdots + \boldsymbol{\theta}_b^n \tag{4.26}$$

$$\mathbf{u}_c^{n+1} = \mathbf{u}_c^n + \cdots + \boldsymbol{\psi}_{cb}\mathbf{u}_b^n + \boldsymbol{\psi}_{cc}\mathbf{u}_c^n + \boldsymbol{\psi}_{cd}\mathbf{u}_d^n + \cdots + \boldsymbol{\theta}_c^n \tag{4.27}$$

where $\boldsymbol{\psi}_{ij} = \frac{\Delta t^2}{2\rho}(\mathbf{S}^T\mathbf{D}\mathbf{S}\mathbf{N}_k)\Big|_{\mathbf{X}_i}\mathbf{u}_j^n$, and $\boldsymbol{\theta}_i^n = (\Delta t - \frac{c\Delta t^2}{2\rho})\dot{\mathbf{u}}_i^n + \frac{\Delta t^2}{2\rho}\mathbf{b}_i^n$ supposing that $\mathbf{X}_j$ is the k^{th} family node of $\mathbf{X}_i$. Updating the displacement vector of "d", as a node with Dirichlet condition, can be made easily as:

$$\mathbf{u}_d^{n+1} = \mathbf{u}^*(\mathbf{X}_d, t^{n+1}) \tag{4.28}$$

It can be concluded that for Type I and II nodes the solution procedure deals with an uncoupled set of equations which can be assembled in a matrix form as:

$$\mathbf{U}_{\mathrm{I,II}}^{n+1} = \mathbf{K}_{\mathrm{I,II}}\mathbf{U}^n + \mathbf{F}_{\mathrm{I,II}}^n \tag{4.29}$$

in which the above equation, in the view of Figure 4.2, can be derived as:

$$\begin{Bmatrix} \vdots \\ \mathbf{u}_b^{n+1} \\ \vdots \\ \mathbf{u}_c^{n+1} \\ \mathbf{u}_d^{n+1} \\ \vdots \end{Bmatrix} = \begin{bmatrix} \vdots & \vdots & \vdots & \vdots & \vdots & \vdots & \vdots & \vdots \\ \cdots & \boldsymbol{\psi}_{ba} & \cdots & \mathbf{I}+\boldsymbol{\psi}_{bb} & \cdots & \boldsymbol{\psi}_{bc} & \mathbf{0} & \cdots \\ \vdots & \vdots & \vdots & \vdots & \vdots & \vdots & \vdots & \vdots \\ \cdots & \mathbf{0} & \cdots & \boldsymbol{\psi}_{cb} & \mathbf{I}+\boldsymbol{\psi}_{cc} & \boldsymbol{\psi}_{cd} & \cdots & \cdots \\ \cdots & \mathbf{0} & \cdots & \cdots & \cdots & \mathbf{0} & \mathbf{0} & \cdots \\ \vdots & \vdots & \vdots & \vdots & \vdots & \vdots & \vdots & \vdots \end{bmatrix} \begin{Bmatrix} \vdots \\ \mathbf{u}_a^n \\ \vdots \\ \mathbf{u}_b^n \\ \vdots \\ \mathbf{u}_c^n \\ \mathbf{u}_d^n \\ \vdots \end{Bmatrix} + \begin{Bmatrix} \vdots \\ \boldsymbol{\theta}_b^n \\ \vdots \\ \boldsymbol{\theta}_c^n \\ \mathbf{u}^*(\mathbf{X}_d, t^{n+1}) \\ \vdots \end{Bmatrix} \tag{4.30}$$

where $\mathbf{I}$ stands for an identity matrix. According to Eq (4.22), for "a" as a node with Neumann condition one may conclude:

$$\cdots + \bar{\boldsymbol{\psi}}_{aa}\mathbf{u}_a^{n+1} + \bar{\boldsymbol{\psi}}_{ab}\mathbf{u}_b^{n+1} + \cdots = \mathbf{t}^*(\mathbf{X}_a, t^{n+1}) \tag{4.31}$$

where $\bar{\boldsymbol{\psi}}_{ij} = (\tilde{\mathbf{n}}\mathbf{D}\mathbf{S}\mathbf{N}_k)\big|_{\mathbf{X}_i}\mathbf{u}_j^n$ supposing that $\mathbf{X}_j$ is the k^{th} family node $\mathbf{X}_i$. It is clear that for updating the displacements of "d" the updated displacements of all its family nodes are required. Some of these nodes are of Type II and thus they have so far been updated by using Eq (4.29), yet for the remaining family nodes (Type III nodes) their updated displacement are not available. In a nutshell, a coupled system of equations for a narrow layer of nodes close to the Neumann boundaries is obtained. Therefore, at each time step the solution of a linear system of equations is required; which can be written as follows:

$$\mathbf{U}_{\mathrm{II,III}}^{n+1} = \mathbf{K}_{\mathrm{II,III}}^{-1}\mathbf{F}_{\mathrm{II,III}}^{n+1} \tag{4.32}$$

It is noteworthy that as the matrix $\mathbf{K}_{\mathrm{II,III}}$ is constant during the analysis, its factorization can be done once, leading to a huge saving in computational time. In the view of Figure 4.2, the above equation can be expressed as follows:

$$\begin{Bmatrix} \vdots \\ \mathbf{u}_a^{n+1} \\ \vdots \\ \mathbf{u}_b^{n+1} \\ \vdots \end{Bmatrix} = \begin{bmatrix} \vdots & \vdots & \vdots & \vdots & \vdots \\ \cdots & \bar{\boldsymbol{\Psi}}_{aa} & \cdots & \bar{\boldsymbol{\Psi}}_{ab} & \cdots \\ \vdots & \vdots & \vdots & \vdots & \vdots \\ \cdots & \mathbf{0} & \cdots & \mathbf{I} & \cdots \\ \vdots & \vdots & \vdots & \vdots & \vdots \end{bmatrix}^{-1} \begin{Bmatrix} \vdots \\ \mathbf{t}^*(\mathbf{X}_a, t^{n+1}) \\ \vdots \\ \mathbf{u}_b^{n+1} \\ \vdots \end{Bmatrix} \tag{4.33}$$

Having solved the above equation, the displacements of all the nodes with Neumann conditions can be found. It should be pointed out that differently from the direct imposition of Neumann boundary conditions, which is the case for the static solution of conventional FPM, here the discretized Neumann equations, associated to Type III nodes, are satisfied at each time step with a set of *equilibrated* equations, associated to Type II nodes, consistent with equations governing the body itself. In Section 4.7 we shall show the suitability of the proposed approach by means of some benchmark problems.

4.6 Implementation

The formulation presented in the previous section, is implemented in a C++ program. The program was compiled using Microsoft Visual Studio 2015. To take advantage of multi-core CPUs available, all possible parts of the program were parallelized using the open multi-processing (OpenMP) directives. OpenMP is an open standard for shared-memory parallelization adopted by a large number of C, C++ and Fortran compilers. In this parallelization scheme, the blocks of code to be parallelized (usually `for` loops) are marked by special `#pragma omp` directives. The compiler generates the appropriate parallel code for blocks. Special care must be taken to avoid *race conditions*, i.e. where the result of an operation depends on the order execution of different threads. OpenMP uses system threads for its parallel execution model. Each thread is an independent path of execution, which if possible, is scheduled on a separate

core in multicore CPUs by the operating system to leverage full power of such hardware platform.

An important step in the solution procedure is the solution of the linear system of equations in Eq (4.32). To this end, we employed the "AMGCL" library[1]. AMGCL is a light, header-only, templated C++ library for solution of sparse linear systems of equations with several options for solver, pre-conditioner and parallelization strategy. It includes implementation of algebraic multi-grid (AMG) methods which enhances the solution performance. As the coefficient matrix in Eq (4.32) is constant during the solution, setting up the required data structures and factorizing the matrix is done only once to reduce the computational cost.

4.7 Numerical examples

In this section, three numerical examples are described to illustrate the potentialities of the presented approach. In Example I, the results are compared with the exact solution through an L^2 relative error norm defined at node $\mathbf{X}_i$ as:

$$e = \sqrt{\sum_{j=1}^{\eta} (u_{ex}(\mathbf{X}_i, t_j) - u_i^n)^2 \Big/ \sum_{j=1}^{\eta} (u_{ex}(\mathbf{X}_i, t_j))^2} \tag{4.34}$$

where u_{ex} indicates the exact solution, and η stands for the number of time steps based on which the norm is calculated.

[1] AMGCL C++ library. https://github.com/ddemidov/amgcl. Accessed: 2017-02-11

4.7.1 Example I

In this example we consider a rectangular plate fixed rigidly at its base and subjected to an impulsive load at the free edge, as shown in Figure 4.3.

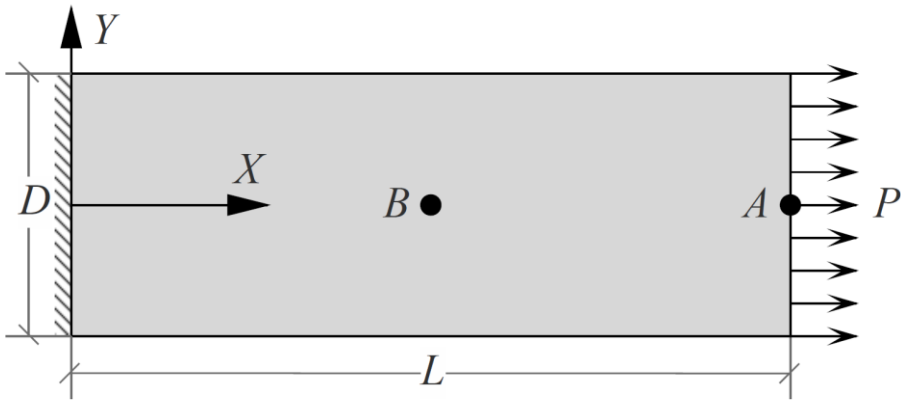

Figure 4.3. The problem domain in Example I.

The geometric, mechanical, and loading parameters are: length $L = 8\text{m}$, height $D = 2\text{m}$, $E = 8\times10^4\,\text{Pa}$, $\nu = 0$, $\rho = 2450\,\text{kg}/\text{m}^3$, $c_d = 0$, and traction $P = 200\text{Pa}$. The exact solution of this example is given by [119]:

$$u(X,t) = \frac{8PL}{\pi^2 E}\sum_{j=1}^{\infty}\frac{(-1)^{j-1}}{(2j-1)^2}\sin\frac{(2j-1)\pi X}{2L}(1-\cos\omega_j t) \tag{4.35}$$

in which $\omega_j = \dfrac{(2j-1)\pi}{2L}\sqrt{E/\rho}$. The solution of this example using the present approach, for a time duration of 7 seconds is considered. The domain is discretized through a Cartesian uniform grid of nodes with equal nodal spacing Δx both in the horizontal and vertical directions. To show the convergence of the solution obtained by the present approach, we solve the problem for three different grid sizes taking Δx equal to 0.5m, 0.125m, and 0.03125m. Meanwhile, in all the cases Δt is taken to be 0.0005s. The horizontal displacements of node A and B, as shown in Figure 4.3, are presented in

Figure 4.4. As a consequence, the results obtained by FPM are in a good agreement with those of the exact solution.

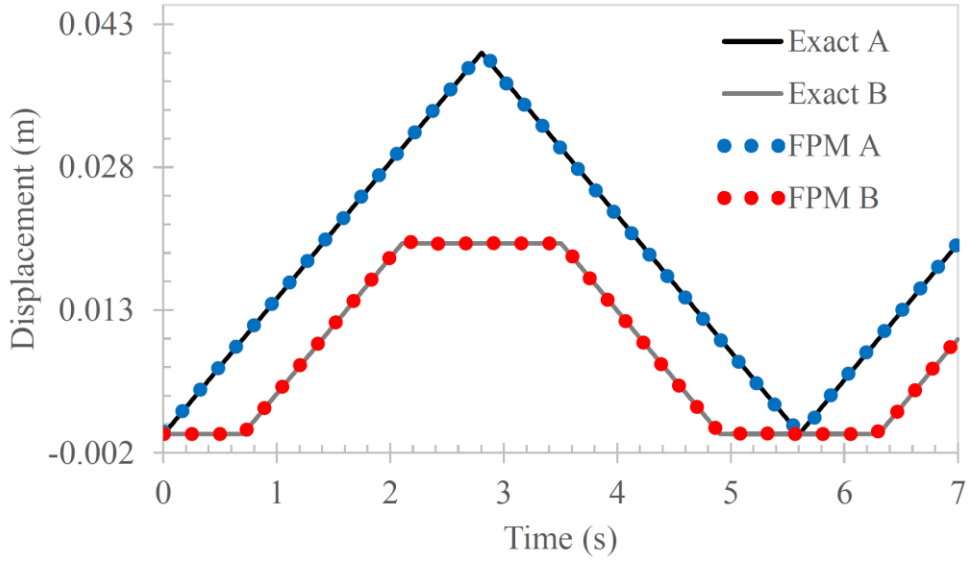

Figure 4.4. The variations of horizontal displacement at points A and B in Example I; $\Delta x = 0.125\text{m}$.

The errors, based on Eq (4.34), for the horizontal displacement of nodes A and B are reported in Table 4-1. The variation of displacement error at points A and B, for different nodal spacing, is shown in Figure 4.5. It can be concluded that the method performs well and its solution converges to the exact solution by refining the solution domain. That is also true for point A where Neumann boundary conditions are applied.

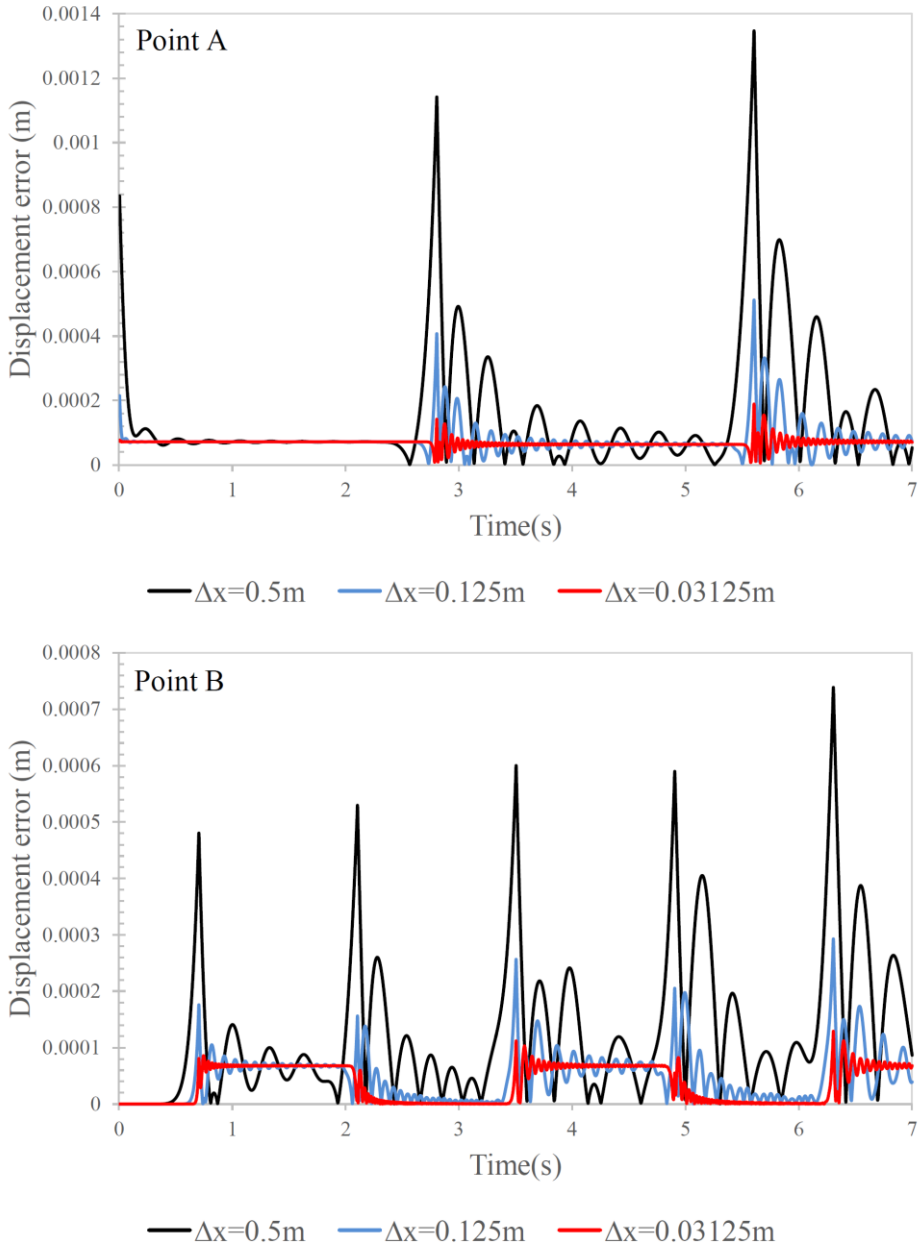

Figure 4.5. The variations of displacement error at points A and B in Example I.

Table 4-1. The obtained norms of error in Example I at nodes A and B.

Δx	0.5m	0.125m	0.03125m
A	0.011934	0.004388	0.003270
B	0.015454	0.005628	0.004152

4.7.2 Example II

In this example, we consider a 3D cantilever beam with a rectangular cross section as shown in Figure 4.6. The beam is subjected to a periodic shear stress distribution $q(t) = \tau \sin(\omega_f t)$ at the free end. The basic parameters are: length $L = 48\text{m}$, depth $D = 12\text{m}$, width $W = 6\text{m}$, $E = 3\times10^4\,\text{Pa}$, $\nu = 1/3$, $\rho = 1\text{kg}/\text{m}^3$, and $c_d = 0$. The magnitude and frequency of the excitation are respectively $\tau = 13.89\,\text{N}/\text{m}^2$ and $\omega_f = 27\,\text{rad}/\text{s}$

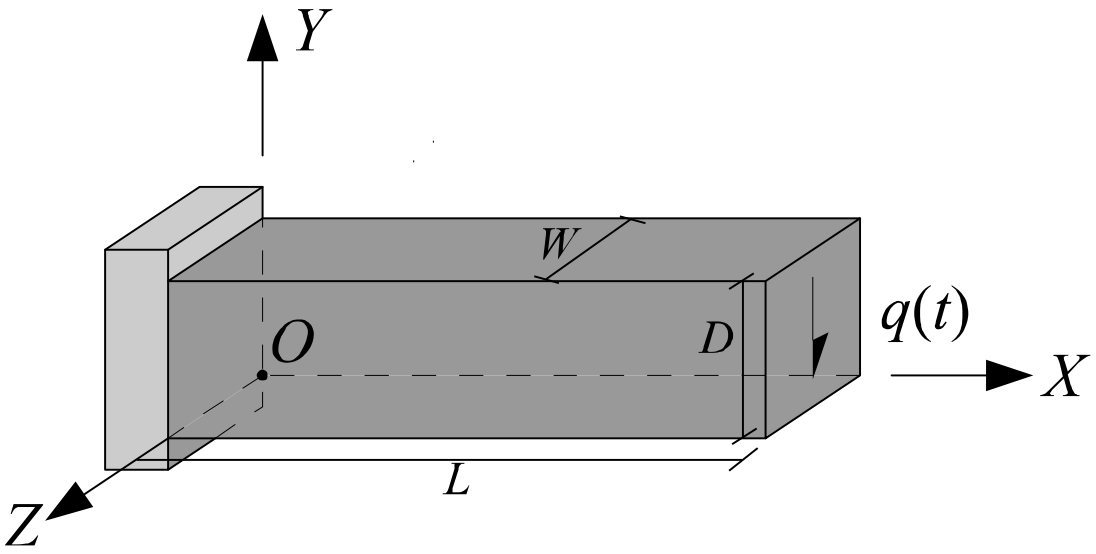

Figure 4.6. The problem domain in Example II.

To proceed with the solution of FPM, the domain is discretized by a Cartesian uniform grid of nodes with a nodal spacing of $\Delta x = 0.6\text{m}$. To check the suitability of the results, the solution of a standard/explicit FEM model using 1600 linear cubic elements is taken into account, as well. The nodal spacing in both models is identical which results in 18711 nodes. We consider the solution for a duration of 0.5 seconds, and in both models Δt is taken to be 0.00002s. The variation of displacements along the Y axis at point A at the free end, $\mathbf{X}_A = (48, 6, 3)$, and point B at the center of the beam, $\mathbf{X}_B = (24, 6, 3)$, are shown in Figure 4.7. The results obtained by FPM are in excellent agreement with those of FEM. The contour plot of displacement along the Y axis (for both models), at $t = 0.44\text{s}$ is reported in Figure 4.8. As can be seen, the solution of FPM resembles that of FEM using the same nodal spacing.

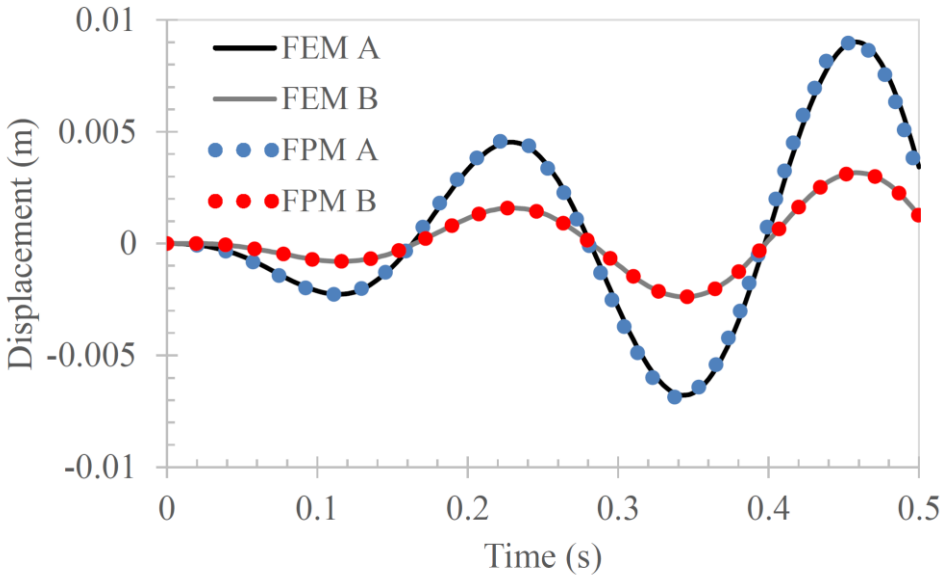

Figure 4.7. The variations of horizontal displacement at points A and B in Example II; $\Delta x = 0.6\text{m}$.

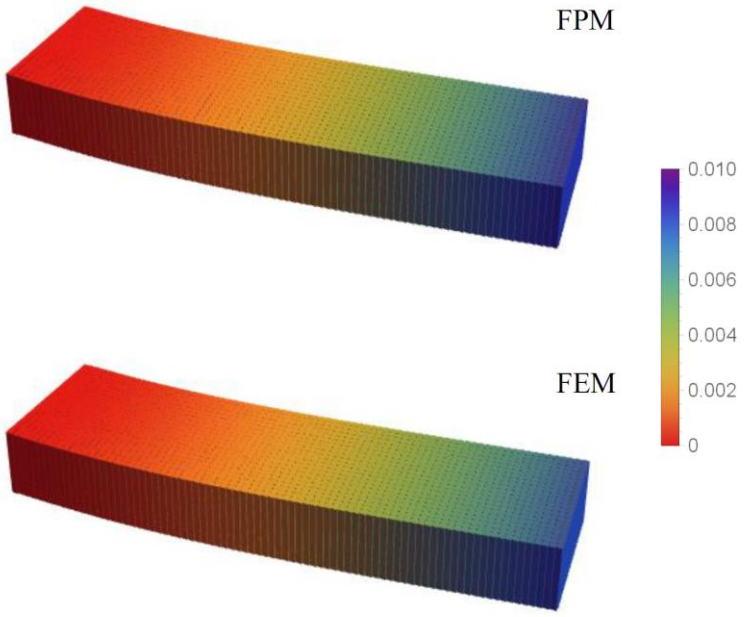

Figure 4.8. The contour plot of displacement (m) along the Y axis obtained by both FPM and FEM methods, at $t = 0.44\text{s}$ *, in Example II.*

4.7.3 Example III

This example concerns the transient behavior of a prismatic body with a rectangular $2\text{m} \times 2\text{m}$ cross section and with a height of 4m as shown in Figure 4.9. The material properties of the body are $E = 105\,\text{N/m}^2$, $\nu = 0.25$, $\rho = 1\text{kg/m}^3$, and $c_d = 0$. The body is fixed at its end and subjected to two different impulsive flexural and torsional loading conditions (see Figure 4.9). For both cases the surface traction is imposed with an identical triangular time variation illustrated in the same figure, and the solution of the problem for a time duration of 0.3 seconds is sought. In this example, the FPM solution is performed taking $\Delta t = 0.00015\text{s}$ using a uniform discretization of the domain with a nodal spacing of $\Delta x = 0.125\text{m}$; which results in 9537 nodes.

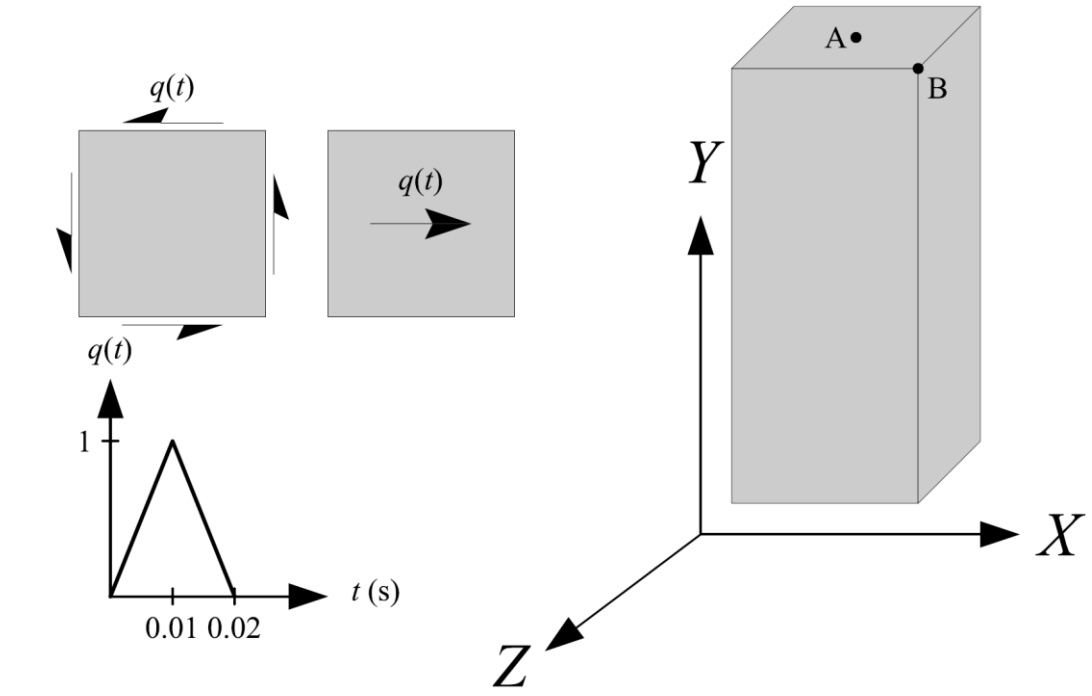

Figure 4.9. The problem domain in Example III; the loads are shown from the top side.

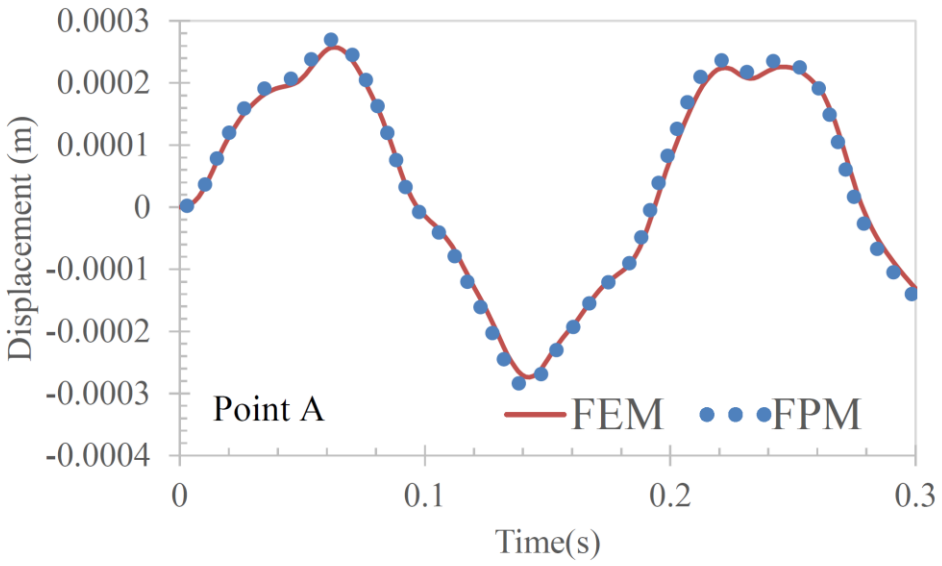

Figure 4.10. The displacement for Point A in Example III.

Again for the sake of verification, the solution of FEM by using linear cubic elements, and the same discretization size which results in 8912 elements, is taken into account. The variation of displacement along X axis for point A, in the flexural loading case, and point B, in the torsional loading case, are shown in Figure 4.10 and 11. Comparing the results with those obtained by FEM, one can conclude that the agreement between the two numerical approaches is very good.

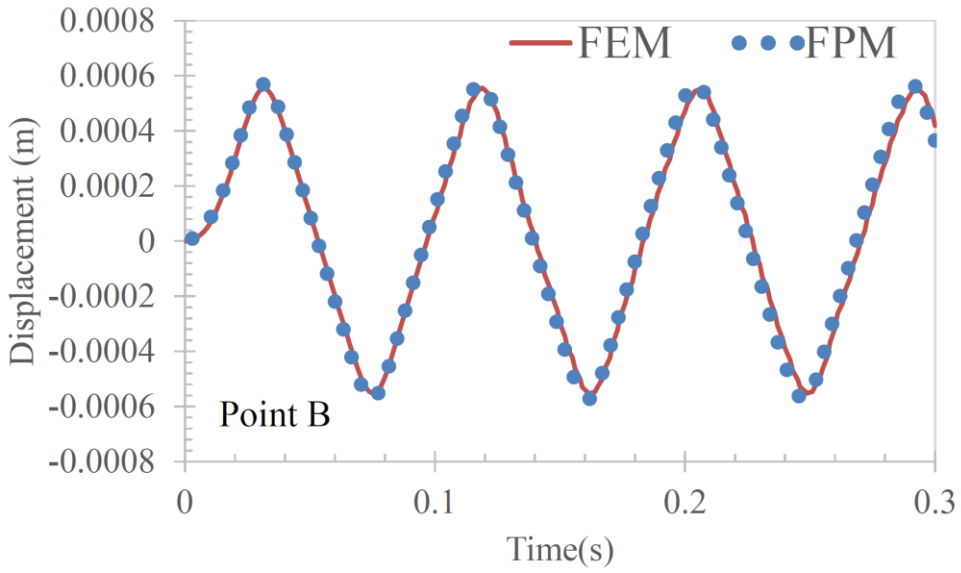

Figure 4.11. The displacement for Point B in Example III.

5. A coupled meshless finite point/peridynamic method for 2D dynamic fracture analysis

5.1 Introduction

The main goal of this chapter is to develop a novel meshless method based on an efficient coupling between FPM and peridynamics for the solution of dynamic crack propagation problems in 2D. In fact, the formulation developed in Chapters 3 and 4 underpins the basis of this work. In this sense, inspired by the switching technique introduced in Chapter 3 a discretized peridynamic model is coupled with FPM, while here the suitability of the approach for the case of dynamic problems is investigated. To perform the simulation in time two different partitioning of the solution domain are introduced which will be discussed in the subsequent sections.

5.2 Adaptivity

In order to minimize the computational resources required by the coupled models, we propose an adaptive method that restricts the use of peridynamics where it is really necessary. We divide the solution domain into three non-overlapping parts Ω_1, Ω_2 and Ω_3 such that $\Omega_1 \cup \Omega_2 \cup \Omega_3 = \Omega$. Ω_1 is the region governed only by peridynamics, for it may contain discontinuities. This region is discretized by means of the meshless bond-based peridynamic method. Ω_3 represents the region where the solution is smooth and hence it can be governed by classical continuum mechanics. This region is discretized by using

the FPM method. Ω_2 corresponds to the transition region that provides the connection between the nonlocal portion Ω_1 and the local zone Ω_3.

In this study, the subdivision of the solution domain is studied through two different approaches. The first approach corresponds to a fixed partitioning in which the parts Ω_1, Ω_2 and Ω_3 are defined once and for all at the beginning of the simulation (see Figure 5.1). In this way, the analyst should predict the path of the cracks properly and situate the peridynamic domain over the regions where there is the possibility of crack propagation. However, prediction of crack paths for practical problems with complex geometries and load conditions is not an easy task. This issue may force the analyst to situate the peridynamic zone even in unnecessary regions.

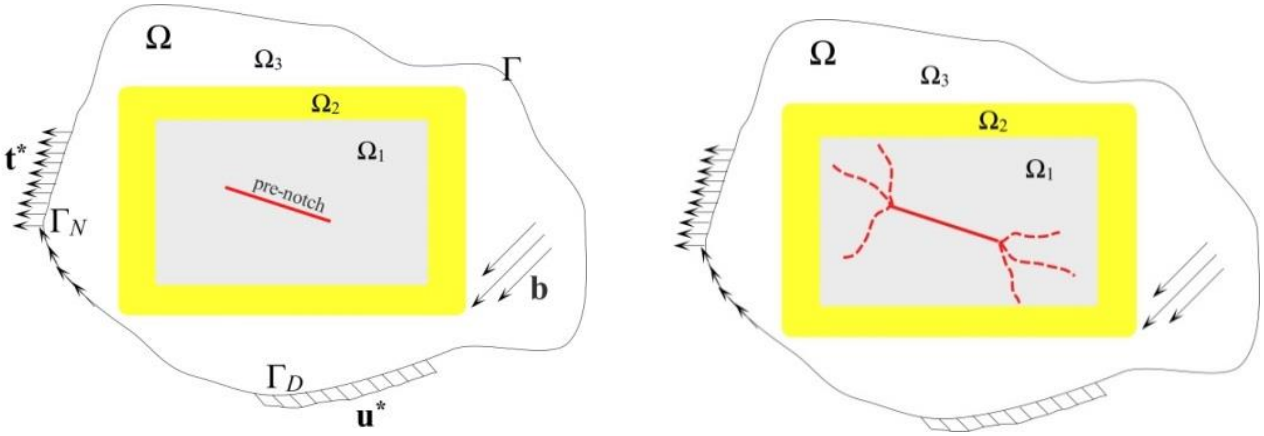

(a) (b)

Figure 5.1. The same subdivision of solution domain is presented: at (a) the initial, and (b) final time step in fixed partitioning.

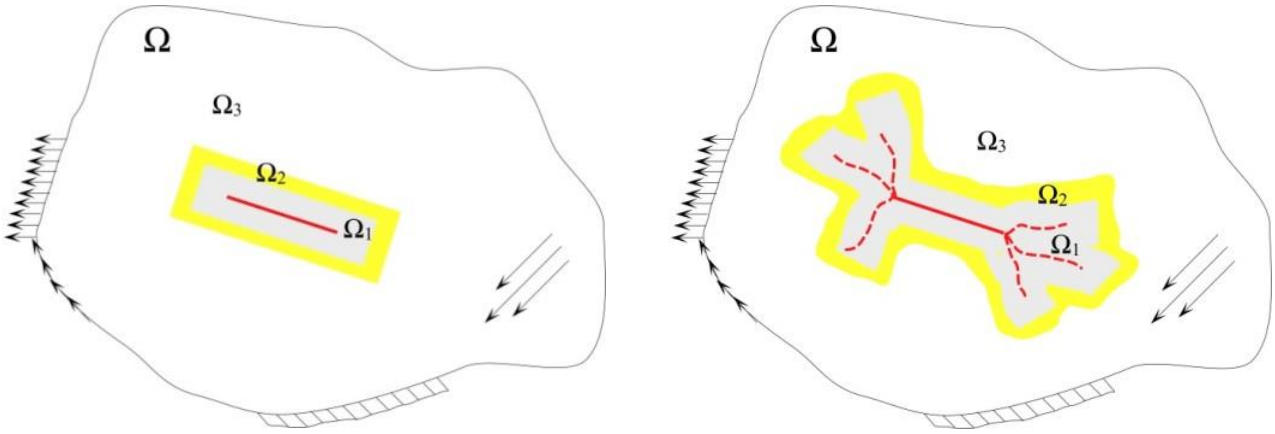

(a) (b)

Figure 5.2. Subdivision of solution domain: at (a) initial, (b) final time step in dynamic partitioning.

The second approach is an adaptive partitioning which is more efficient (see Figure 5.2). In this way, the partitioning can vary due to the propagation of cracks and the peridynamic domain tracks the crack paths. Such an approach limits the peridynamic domain only to necessary parts and reduces the computational cost. However, the possibility to update the partitioning, during propagation of cracks, depends on the applied coupling technique. We shall show in Section 4 that the present coupling approach is capable of being used for such cases in an automatic and convenient way.

5.3 Coupling and adaptive switching for failure analysis

5.3.1 The coupling scheme

As previously stated, the solution domain is divided in three parts Ω_1, Ω_2 and Ω_3. Figure 5.3 shows a portion of a discretized domain. Circles are peridynamic nodes and diamonds are FPM nodes. Cracks can only propagate in the zones discretized with peridynamic nodes. The transition region consists of two layers of nodes; a layer made of

peridynamic nodes (unfilled circles) and another of FPM nodes (unfilled diamonds). The thickness of this layer depends on the horizon and cloud sizes. In conclusion, we consider four representative nodes, shown in Fig. 6, as $\mathbf{X}_a$, $\mathbf{X}_b$, $\mathbf{X}_c$ and $\mathbf{X}_d$ so that each node represents one of the four available types.

Given displacement and velocity vectors of each node at time step *n*, according to Eq (4.25), the vector of displacement at the next step can be found.

Therefore, the value of $\ddot{\mathbf{u}}_n$ at each time step should be determined, based on the position of the nodes.

Node $\mathbf{X}_a$ in Ω_1:

$\mathbf{X}_a$ represents any node in zone Ω_1, the *pure* peridynamic nodes, whose horizon contain only peridynamic nodes. Nodes in zone Ω_1 see all the surrounding nodes as peridynamic nodes; therefore, the acceleration vector of $\mathbf{X}_a$ can be obtained according to Eqs (2.75) and (3.15):

$$\rho\ddot{\mathbf{u}}_a^n = \ldots \mu_{aa_1}^n \hat{\mathbf{f}}_{aa_1}^n + \mu_{aa_2}^n \hat{\mathbf{f}}_{aa_2}^n + \ldots \mu_{ab}^n \hat{\mathbf{f}}_{ab}^n + \mu_{ab_1}^n \hat{\mathbf{f}}_{ab_1}^n + \mu_{ab_2}^n \hat{\mathbf{f}}_{ab_2}^n + \ldots + \mathbf{b}_a^n \tag{5.1}$$

where $\mu_{ij}^n = \mu(\mathbf{X}_j - \mathbf{X}_i, n\Delta t)$, and $\hat{\mathbf{f}}_{ij}^n = \mathbf{k}_{ij}^{11}\mathbf{u}_i^n + \mathbf{k}_{ij}^{21}\mathbf{u}_j^n$.

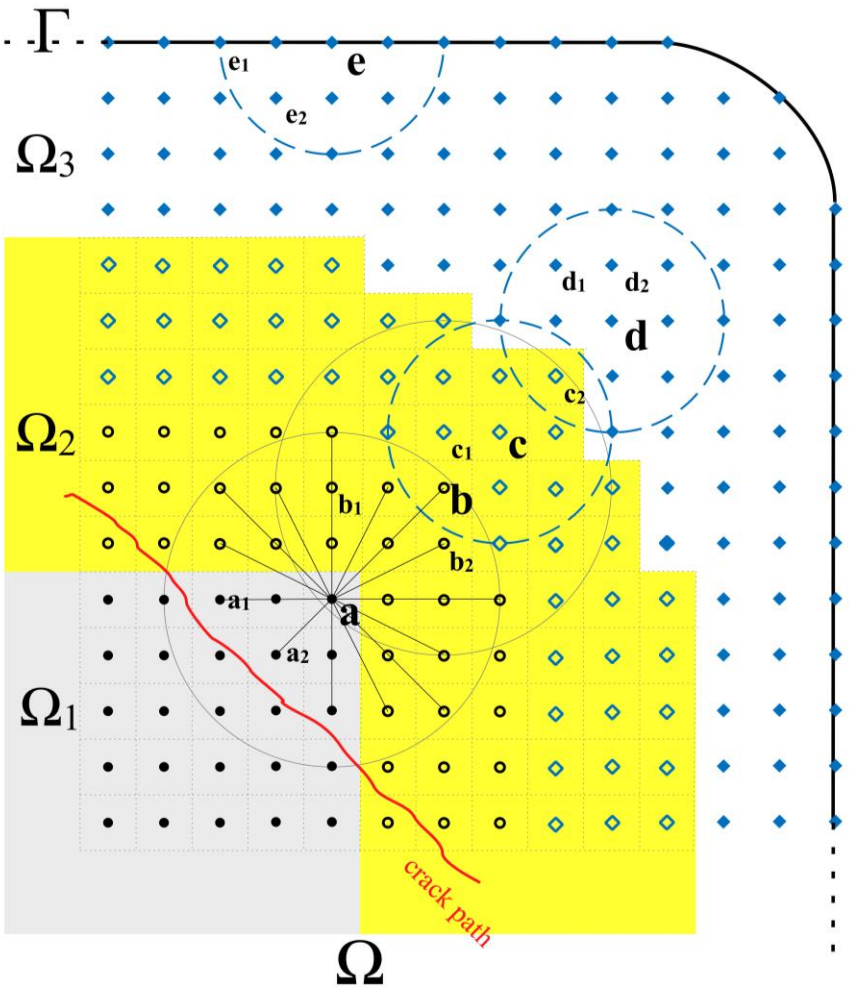

Figure 5.3. The coupling scheme and definition of different layers of solution domain in the present study.

Node $\mathbf{X}_b$ in Ω_2:

$\mathbf{X}_b$ represents any node in the *transition* peridynamic layer. The horizon of $\mathbf{X}_b$ contains some nodes located in Ω_1 and in Ω_2. All family nodes of a source node of this type behave as peridynamic nodes; consequently, the acceleration of $\mathbf{X}_b$ can be calculated as follows:

$$\rho\ddot{\mathbf{u}}_b^n = \ldots \mu_{ba}^n \hat{\mathbf{f}}_{ba}^n + \ldots + \mu_{bb_1}^n \hat{\mathbf{f}}_{bb_1}^n + \mu_{bb_2}^n \hat{\mathbf{f}}_{bb_2}^n + \ldots + \mu_{bc}^n \hat{\mathbf{f}}_{bc}^n + \mu_{bc_1}^n \hat{\mathbf{f}}_{bc_1}^n + \mu_{bc_2}^n \hat{\mathbf{f}}_{bc_2}^n + \ldots + \mathbf{b}_b^n \tag{5.2}$$

Even though nodes $\mathbf{X}_c$, $\mathbf{X}_{c_1}$ and $\mathbf{X}_{c_2}$ in Figure 5.3 are mainly FPM nodes, they play the role of a peridynamic node if $\mathbf{X}_b$ is the source node.

Node $\mathbf{X}_c$ in Ω_2:

$\mathbf{X}_c$ represents any node in the *transition* FPM layer. The cloud of $\mathbf{X}_c$ contains nodes located in Ω_2 and in Ω_3. All nodes in a cloud of a source node of this type behave as FPM nodes; consequently, the acceleration of $\mathbf{X}_c$ can be calculated, according to Eq (4.20), as follows:

$$\rho\ddot{\mathbf{u}}_c^n = \ldots + \bar{\mathbf{f}}_{cb} + \ldots + \bar{\mathbf{f}}_{cc} + \bar{\mathbf{f}}_{cc_1} + \bar{\mathbf{f}}_{cc_2} + \ldots + \mathbf{b}_c^n \tag{5.3}$$

where $\bar{\mathbf{f}}_{ij} = (\mathbf{S}^{\mathbf{T}}\mathbf{D}\mathbf{S}\mathbf{N}_j)\big|_{\mathbf{X}_i} \mathbf{u}_j^n$. The above equation indicates that a transition peridynamic node, of type $\mathbf{X}_b$, plays the role of a FPM node in the local approximation of nodes in this layer.

Node $\mathbf{X}_d$ in Ω_3:

$\mathbf{X}_d$ represents any node in zone Ω_3, the *pure* FPM nodes whose cloud contains only FPM nodes in Ω_3. The acceleration vector of node $\mathbf{X}_d$ can be expanded as:

$$\rho\ddot{\mathbf{u}}_d^n = \ldots + \bar{\mathbf{f}}_{dd} + \bar{\mathbf{f}}_{dd_1} + \bar{\mathbf{f}}_{dd_2} \ldots \mathbf{b}_d^n \tag{5.4}$$

Remark I: A consequence of the proposed coupling method is that all peridynamic source nodes have a complete horizon so that many problems related to soft surface effect and to the approximation of boundary conditions are solved. ■

Remark II: With respect to Eq (4.2), the displacement of a boundary node; for instance $\mathbf{X}_e$ shown in Figure 5.3, at time step n+1 should be determined by:

$$\mathbf{t}^*(\mathbf{X}_e,(n+1)\Delta t)=\ldots+\bar{\mathbf{f}}^*_{ee_1}+\bar{\mathbf{f}}^*_{ee}+\bar{\mathbf{f}}^*_{ee_2}+\ldots \tag{5.5}$$

where $\bar{\mathbf{f}}^*_{ij}=(\tilde{\mathbf{n}}^{\mathrm{T}}\mathbf{D}\mathbf{S}\mathbf{N}_j)\big|_{X_i}\mathbf{u}^{n+1}_j$. Similar to the discussion in Section 4.5, it is clear that to update the displacement of the boundary node it is necessary to have also the displacements of its family nodes at time step $n + 1$; some of the family nodes may also be boundary nodes. As a result, for the nodes located on the Neumann boundaries as well as their family nodes, it is necessary to assemble their relations in a matrix and solve a linear system of equations. This system of equation contains only the DOFs of a layer of nodes along the Neumann boundaries. The relations for the other nodes, are uncoupled and it is not necessary to assemble them in a system of equations. ■

5.3.2 Adaptive partitioning

One of the advantages of the newly proposed coupling is the possibility to adopt with it an adaptive partitioning, as explained in Section 5.2. The main goal is to restrict the peridynamic zone to the cracked parts as well as to the parts which are likely to be affected by cracks within the next few time steps. A simple criterion to decide where cracks are going to develop has to be computationally cheap and automatic. FPM nodes should be changed into peridynamic nodes so that the nonlocal zone follows the crack paths while keeping the local zone sufficiently far away. The distance between any FPM node and the crack path, d_c, must be greater than its cloud size; i.e. $d_c \geq \delta_F$ to preserve the validity of local approximation. Figure 5.4 schematically shows a part of a generic domain represented by FPM and peridynamic nodes at a given time step. For the sake of simplicity, the transition nodes are shown with filled icons. The peridynamic zone covers

thoroughly the cracked zone and the FPM nodes are positioned so that none of their clouds is intersected by the crack path.

In the present study, the adaptivity criterion is defined on the basis of a simple stretch control for each pair of adjacent FPM nodes. For each pair of adjacent FPM nodes, $\mathbf{X}_i$ and $\mathbf{X}_j$, one can define the stretch of the material between them at time *n* as:

$$s'^{n}_{ij} = \frac{\left\| \mathbf{u}_i^n - \mathbf{u}_j^n \right\|}{\left\| \mathbf{X}_i - \mathbf{X}_j \right\|} \tag{5.6}$$

The status of each pair of adjacent FPM nodes can be qualified with the s′ value to identify critical FPM nodes whose region is more likely to be affected by crack propagation.

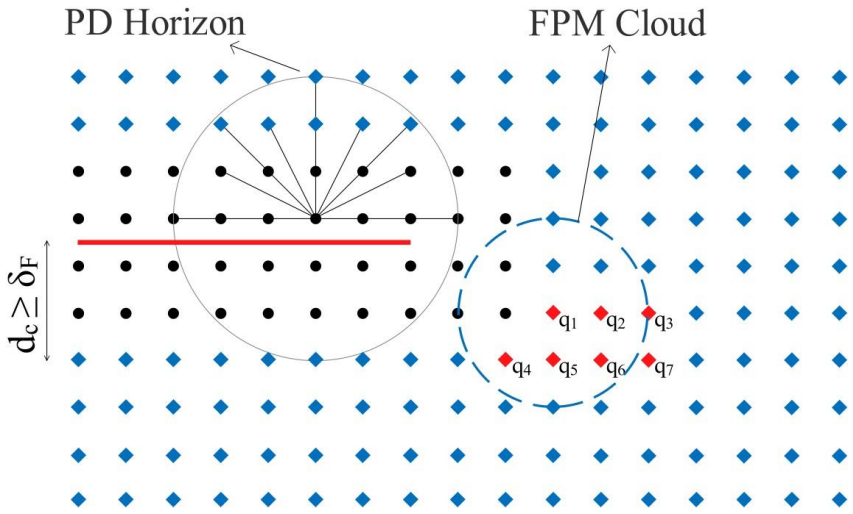

Figure 5.4. Formation of critical FPM nodes before being changed to peridynamic nodes.

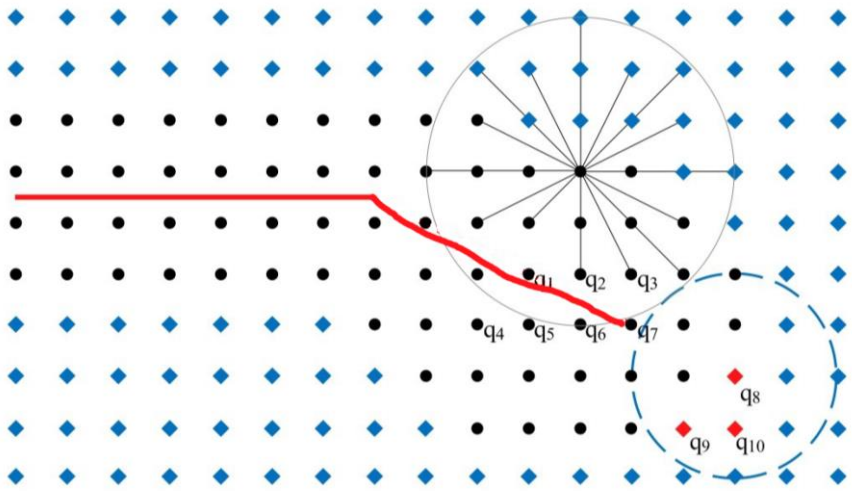

Figure 5.5. Changing of FPM critical nodes to peridynamic nodes and identification of new critical nodes near the crack tip.

A critical pair of nodes, $\mathbf{X}_i$ and $\mathbf{X}_j$, should be identified by an indicator defined by:

$$\chi s_0 \le s_{ij}'^n < s_0, \quad 0 \le \chi \le 1 \tag{5.7}$$

in which χ is a constant that plays the role of a safety factor and s_0 is defined in Eq (2.72). Critical FPM nodes, at time step n, are always identified in pairs by the value of the relevant s' that falls into the interval introduced in Eq (5.7). To exemplify, in Figure 5.4 the red diamond nodes $q_1, q_2, \ldots, q_7$ stand for the critical nodes.

Now, before proceeding with the next steps, all the critical nodes as well as all the family nodes in their clouds should be simply changed to peridynamic nodes as shown in Figure 5.5. In this way a new partitioning of the domain will be obtained and the peridynamic zone will be extended. At the new time step a new critical zone may emerge, represented by q_8, q_9, and q_{10}.

It should be pointed out that such an adaptive partitioning can be implemented simply, and it is computationally cheap. We believe that this technique can be applied to 3D problems as well. In this case, the critical nodes should be changed to peridynamic nodes within a sphere instead of a circle. Extension of the present work to 3D problems might be considered in future studies.

Remark III: Taking larger values for χ keeps the peridynamic zone smaller and, subsequently, it makes the computational cost lower. However, this value should be taken in a conservative range based on the speed of crack propagation; otherwise, the crack may reach the FPM nodes before they are changed into peridynamic nodes. In such a case the simulation should go back to the past and switch the missed FPM nodes to peridynamic nodes to proceed with the solution in time. We heuristically found that taking χ in the range $0.6 \le \chi \le 0.8$ can be a suitable choice.■

5.3.3 Numerical implementation

One may consult [33] for a comprehensive investigation into different values of *m* ratio in the case of dynamic crack propagation. Based on the studies conducted in [33], in the present study $m = 4$ is adopted.

FPM clouds can be taken of various shapes. For the sake of consistency and simplicity, in this study FPM clouds are taken to be circles with a radius of 2Δ. This choice leads to have 13 nodes on average in FPM clouds while there are 49 nodes in peridynamic neighborhood. We shall show in the section on numerical examples that using the adaptive partitioning, and restricting the peridynamic nodes only to necessary parts, one

can significantly reduce the computational cost. Such a reduction would be much more significant in 3D problems.

In all the examples, for the local solution of FPM quadratic polynomial basis functions are used and for the nodes located at the boundaries the size of the clouds is set in such a way that at least 9 nodes are included for the local approximation. In the case of boundary nodes the FPM cloud is not a circle with the relevant node at its center.

Remark IV: In the case of a conical micro-modulus formulation in 2D [33]:

$$c(\boldsymbol{\xi}) = \frac{24E}{\pi\delta^3(1-\nu)}\left(1-\frac{\|\boldsymbol{\xi}\|}{\delta}\right) \tag{5.8}$$

c is decreasing linearly along the distance from the center of H_x. This makes the peridynamic model more localized and thus reduces the quadrature error and the surface effect. This feature results in a faster convergence of peridynamic results to both the classical solution for linear elasticity (see [39]) and also experimental results in the case of dynamic fracture (see [33]). In the case of conical micro-modulus s_0 should be calculated as [33]:

$$s_0 = \sqrt{\frac{5\pi G_0}{9E\delta}} \tag{5.9}$$

5.3.4 Ghost force test

This section is devoted to evaluating the presence of ghost forces. Following the ghost force test described in Section 3.7.1. The test is done through a simple ghost force test again. The static solution can be obtained by setting the acceleration of each node in the equation of motion equal to zero, and then solving a linear system of algebraic

equations as in Eq (3.16). We consider a square solution domain $\Omega = (-0.5, 0.5) \times (-0.5, 0.5)$, as illustrated in Figure 5.6; Also zones Ω_1, Ω_2, and Ω_3 are shown in the figure.

We consider a rigid body translation by imposing Dirichlet boundary conditions to all the boundary nodes:

$$\mathbf{u}^{ex} = (1,1)^T \tag{5.10}$$

The displacements of all internal nodes are computed by solving Eqs (5.1)-(5.4). We compare the exact solution displacement with that computed numerically by means of the error norm defined in Eq (3.28).

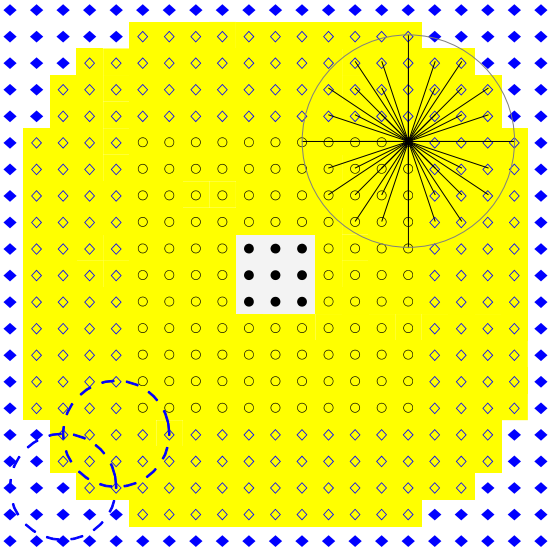

Figure 5.6. Domain discretization used in the ghost force test. The yellow area is the transition region, the central white square zone is Ω_1, the remaining part of the model is Ω_3.

The error norm is computed for all sets of nodes and the relevant results are shown in Table 5-1. All the internal nodes perfectly follow the imposed rigid body motion, and they are translated without producing deformation in the grid. It can be concluded that the method passes the patch test successfully and thus the coupling technique is free from ghost forces in all the portions of the solution domain.

Table 5-1. Norms of error for different layers in the ghost force test.

Layer	a	b	c	d
e_u	7.14×10^{-16}	7.65×10^{-16}	1.10×10^{-15}	5.39×10^{-16}

5.3.5 Example I

In this example, we compare the numerical solution obtained with FPM and the coupled method with that generated by the standard FEM. The cantilever beam shown in Figure 5.7 is loaded by a concentrated periodic force at the free end. The basic parameters are $E = 3\times10^7$ Pa, $\nu = 0.3$ and $\rho = 1$ kg/m^3.

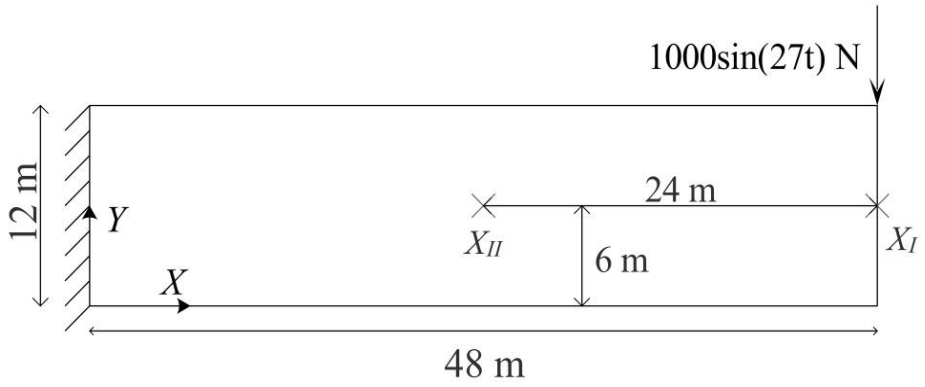

Figure 5.7. Example I: a cantilever beam subjected to a periodic loading.

For the two models the same grid of nodes is adopted; a uniform grid with an average nodal spacing of $\Delta = 1.2$ m which results in 451 nodes. In the FEM model 400 quadrilateral plane stress elements were used.

In Figure 5.8 the solutions obtained by the considered models for the vertical displacement component of the nodes X_I and X_{II}, shown in Figure 5.7, are presented for an interval of 2.0 seconds. The solution obtained by FPM is in a perfect agreement with the FEM solution. The main purpose of this example is to evaluate the results of the coupled method through a fixed partitioning of the solution domain.

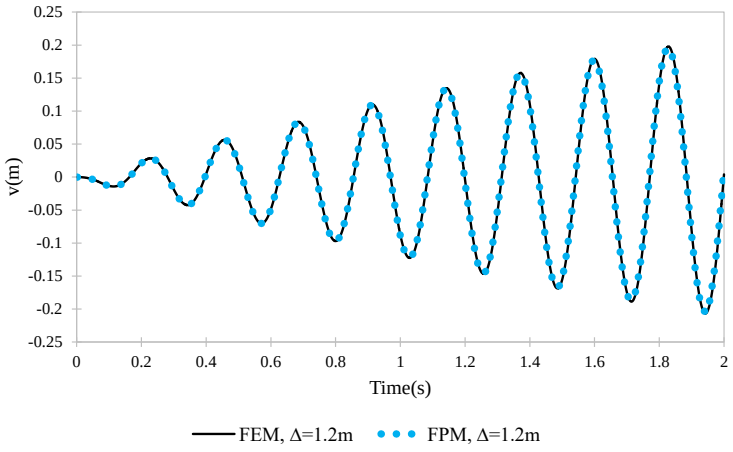

(a)

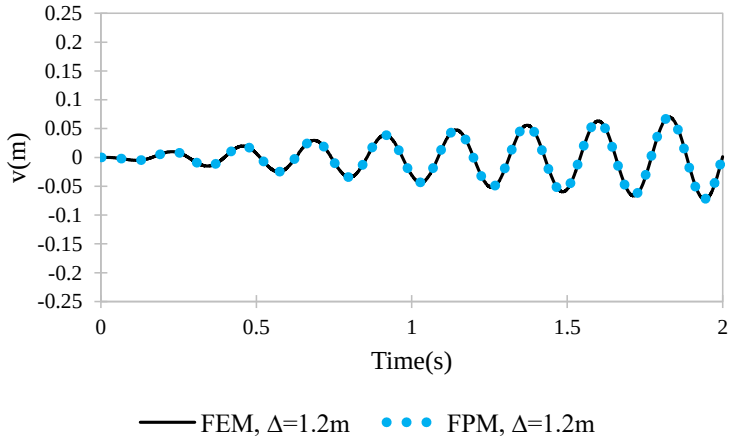

(b)

Figure 5.8. Time history of displacement v at nodes (a) X_I, (b) X_{II} obtained by both FEM and FPM models in Example I.

It should be remarked here on the basis of the studies described in Section 3.7.1, in the linearized version of peridynamics, which is the case of the present study, with the limit

$\delta \to 0$ the peridynamic formulation asymptotically recovers the Navier equation of classical elasticity [50]. In this example, keeping the *m* ratio constant, by refining the solution domain, it is expected that the coupled method should produce a solution similar to that of FEM. In this regard, we consider again a uniform grid for the coupled method with an average nodal spacing of Δ = 0.6 m which results in 1701 nodes; as shown in Figure 5.9. The peridynamic part of the solution domain is considered to be a 8m × 6m rectangle centered at the center of the beam.

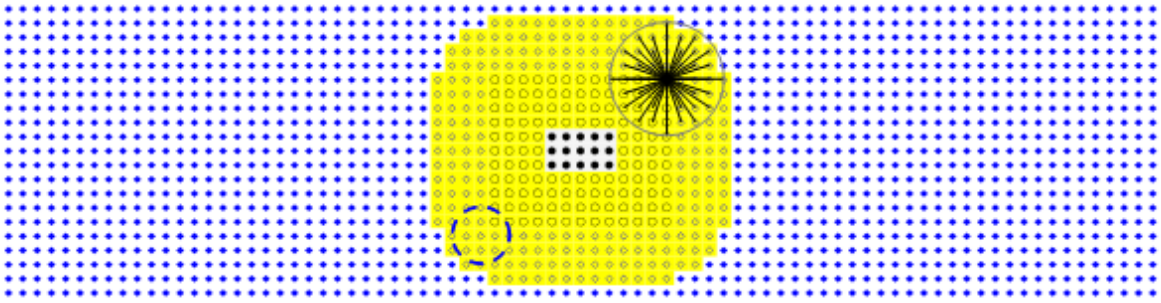

Figure 5.9. Domain discretization used in Example II for the coupled method.

Moreover, to get more insight and for the sake of comparison, we consider the solution of a peridynamic-only model using a nodal spacing of $\Delta = 0.08\,\text{m}$ which results in 90751 nodes; the nodal spacing is almost 7.5 times smaller than that of the coupled method. The results obtained by both models, again at nodes X_I and X_{II}, are reported in Figure 5.10. As can be seen, the solution obtained by the peridynamic model is in a good agreement with that of FEM. Such a small difference between the solutions is due to the wave dispersion properties of peridynamics in wave propagation which can be mitigated by refining the solution domain [120]. The results obtained by the coupled method is in a perfect

agreement with that of FEM using a coarser grid of nodes, and the results converge to the FEM solution quickly.

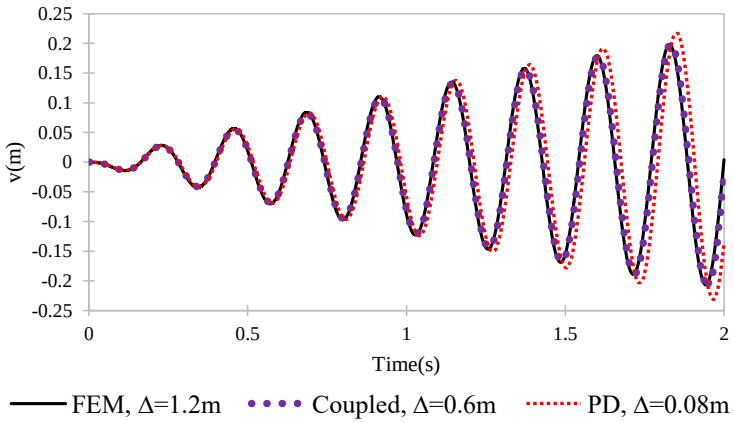

(a)

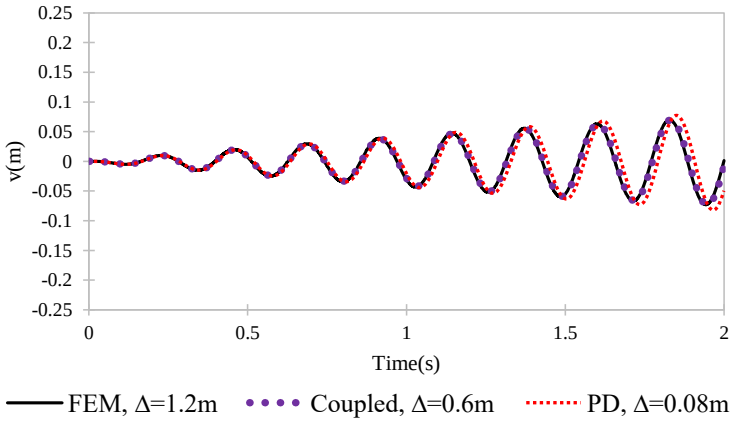

(b)

Figure 5.10. Time history of displacement v at nodes (a) X_I , (b) X_{II} obtained by FEM, the coupled method, and a peridynamic-only model in Example II

It can be concluded, by using the present coupling method and restricting the peridynamic solution only to high strain areas, in the case of failure analysis, the solution of a peridynamic-only model can be reproduced; the coupled method uses a coarser nodal

spacing. This conclusion is valid if there is no significant mismatch between the nonlocal and local dispersion relations[121]. We shall show this feature in the next example.

5.3.6 Example II

This example is devoted to show the capability of the present method in the solution of problems involving dynamic crack propagation. We consider a problem that presents a crack branching in a plate with an initial crack and an applied step load as shown in Figure 5.11. The same case was simulated by a peridynamic-only model in [33].

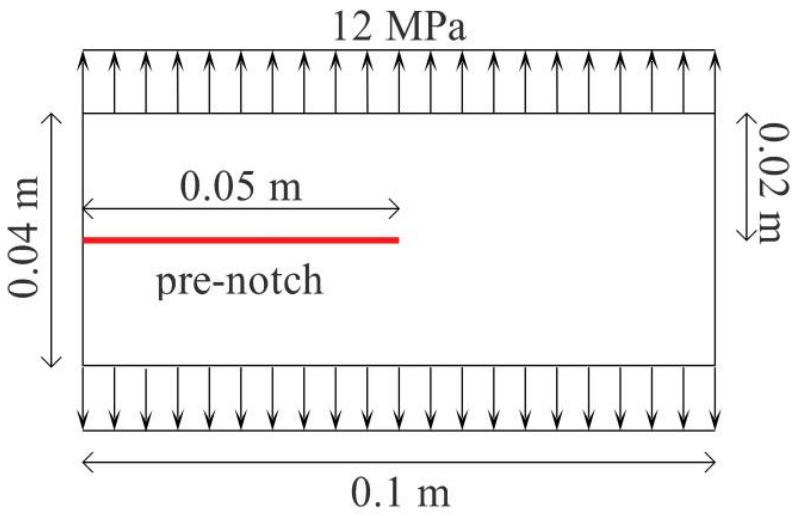

Figure 5.11. Set up description of the pre-cracked plate under traction studied in Example II.

The plate is made of Duran 50 glass and the mechanical properties of the material are $E = 65$ GPa, $\rho = 2,235$ kg/m^3, $\nu = 1/3$, and $G_0 = 204$ J/m^2. In the present study, three different strategies are applied: Model I, Model II and Model III. In Model I, we consider a fixed partitioning to represent the solution domain, and for the other cases, Model II and Model III, we apply the adaptive partitioning. For all cases a time duration of 46 μs is considered and the time step of the numerical integration is 46 ns.

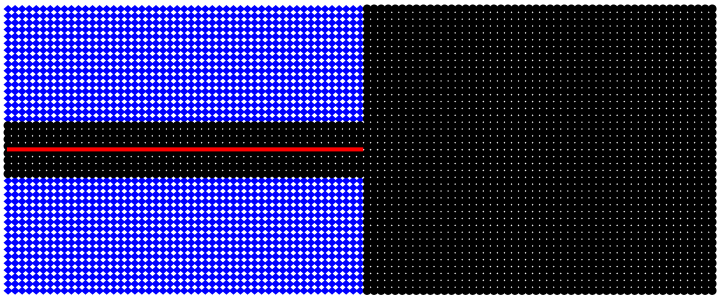

Figure 5.12. The grid used for Model I in solution of the pre-cracked plate in Example II.

For Model I we consider a grid with an average nodal spacing of $\Delta = 1$ mm as shown in Figure 5.12. This configuration is kept constant during the whole simulation. The grid is made of 1734 FPM nodes and 2508 peridynamic nodes. Peridynamic nodes are distributed in the region where the pre-crack is located as well as in the whole region in front of the crack tip where there is the possibility of crack propagation. The remaining part of the solution domain is represented by FPM nodes. The initial crack is conveniently modeled by breaking the corresponding bonds; in addition, the FPM nodes are positioned far enough from the initial crack so that the visibility criterion is observed. In Figure 5.14 six plots of the damage levels at various instants are shown. In this example, for all the plots of damage level we use a unique color code given in Figure 5.13.

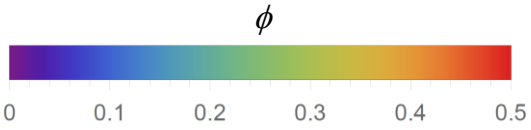

Figure 5.13. The color range bar used for the plots of damage.

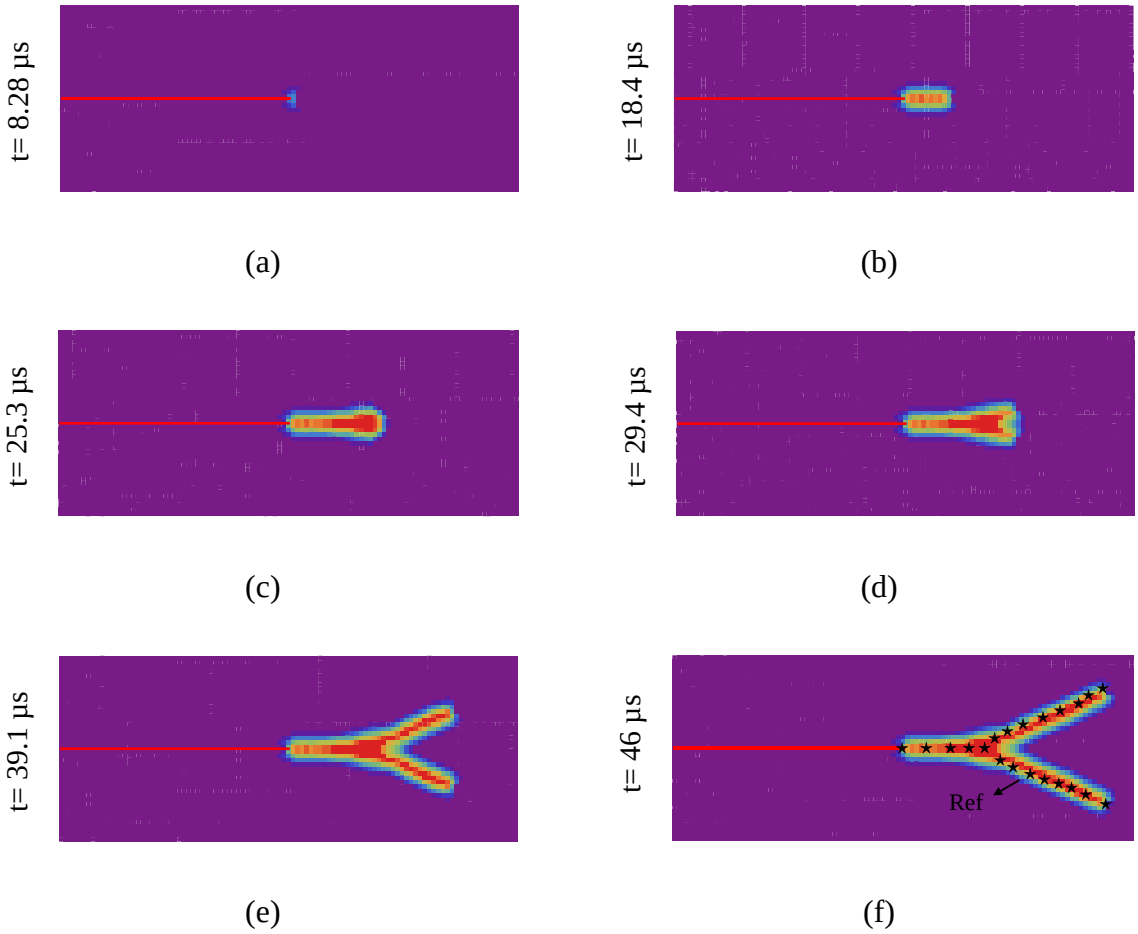

Figure 5.14. . Six snap-shots showing the evolution of damage in Model I. In the last snap-shot the star points illustrate the crack morphology in [33] *using 65,488 nodes.*

In Figure 5.14(f) we compare the crack morphology obtained by the proposed approach with that of [33], where a purely peridynamic model with a very fine nodal spacing of $\Delta = 0.25$ mm (65,488 nodes), was used. The crack morphology obtained in the present study is in excellent agreement with that obtained by a fully nonlocal solution.

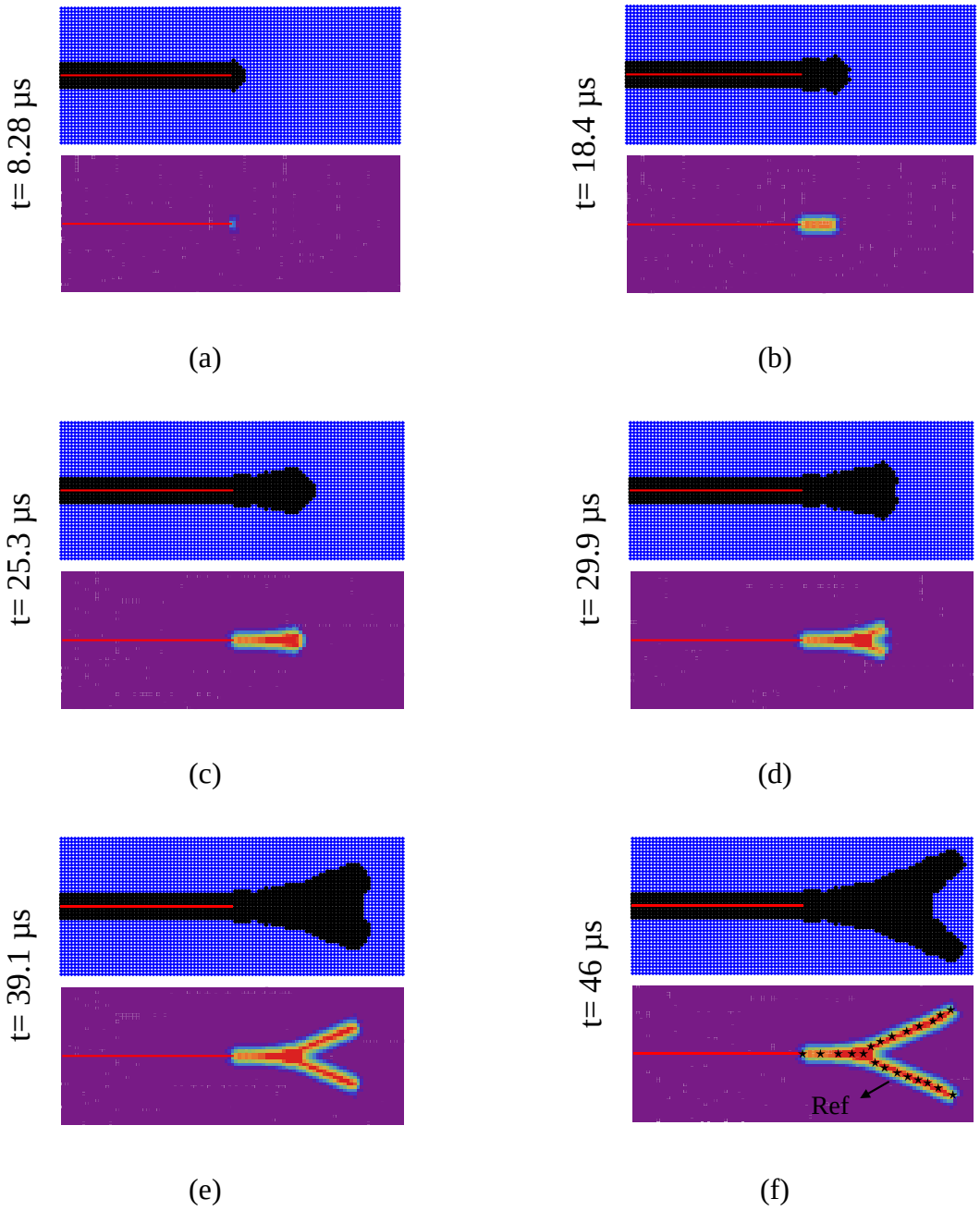

Figure 5.15. Six snap-shots showing the evolution of damage as well as the adaptive partitioning in Model II.

We repeat the simulation with two adaptive partitionings of the solution domain, Model II and Model III. The difference between these two models is in the criterion triggering the adaptive switching. The χ parameter, introduced in Eq (5.7), is taken to be 0.6 in

Model II and 0.8 in Model III. Model II is considered to be more conservative with respect to Model III as the adaptive switching is triggered at a lower level of relative elongation. For both cases, we use a grid with a nodal spacing of 1 mm as in Model I; however, the initial grid is made of only 408 peridynamic nodes, and the remaining part of the solution domain is represented by 3834 FPM nodes. The temporal evolutions of damage as well as the partitioning of the solution domain in six snap-shots are reported in Figure 5.15 and Figure 5.16.

The figures indicate that the performance of the adaptive switching technique is good, the damage distribution in both cases is similar to that of Figure 5.14(f); the nonlocal part precedes the crack morphology keeping the local part far away from the cracked parts. The visibility criterion is satisfied at each time step so that the cracked parts of the solution can not violate the validity of the local approximation of FPM. The obtained crack morphologies in the last snap-shots are compared with the reference fully peridynamic solution. Both models, using a moderate number of nodes and a limited number of peridynamic nodes, provide results in a perfect agreement with the reference solution.

It can be concluded that the conversion of FPM nodes into peridynamic nodes takes place at the right time and in the right zones of the domain. Moreover, all the models provide a result very similar to the reference solution which was obtained with a much larger number of nodes. The plots of Figure 5.16 confirm that choosing a larger χ reduces the size of the zone converted from FPM into peridynamic, so Model III provides an accurate result at a reduced computational cost.

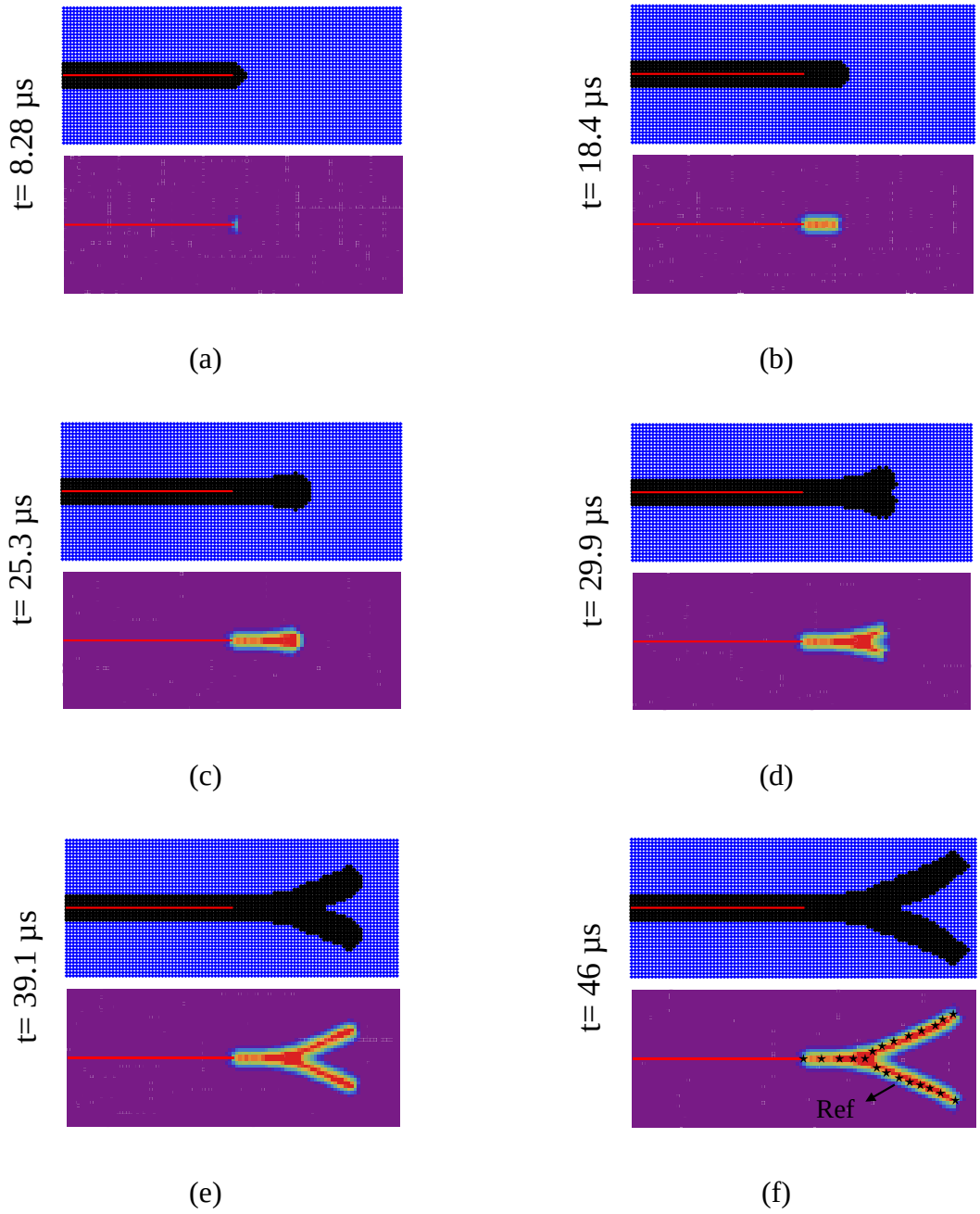

Figure 5.16. Six snap-shots showing the evolution of damage as well as the adaptive partitioning in Model III.

Table 5-2. The portion of peridynamic nodes at the initial and final time steps and the corresponding CPU times for the studied models.

Model	PD nodes portion at at t=0 s	PD nodes portion at t=46 μs	CPU Time (s)
I	59 %	59 %	2362.78
II	9 %	29.4 %	1256.80
III	9 %	25.69 %	1207.52

It should be pointed out that all the simulations are performed with a research code and the hardware features of the computer are:

- Intel(R) Core(TM) i7-3770 CPU @ 3.40GHz
- RAM: 8.00 GB
- OS: Windows 7 Pro 64 bit

The CPU time of the computation for all the models are reported in Table 5-2. The results indicate that the computational times for Model III and Model II are almost half of that of Model I.

5.3.7 Example III

The Kalthoff-Winkler's experiment [122] is a well-known classical benchmark problem for dynamic fracture analysis. The solution of this problem through different approaches has been the object of many researches in the literature; for instance, see [16], [123], [124]. The geometry of the model corresponding to the experimental setup is illustrated in Figure 5.17.

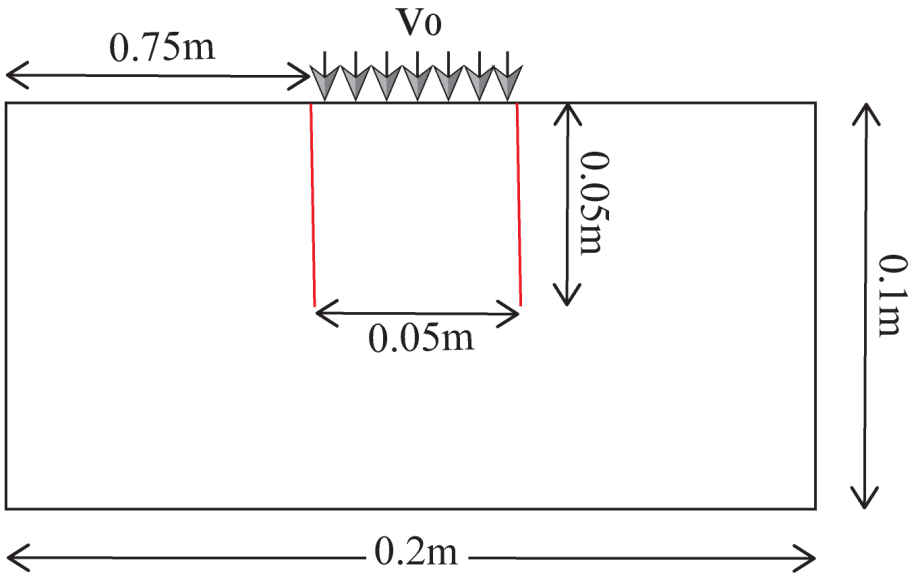

Figure 5.17. Kalthoff-Winkler's experimental setup.

In the experiment, a pre-cracked plate, made of steel 18Ni1900, is hit with an impact loading at the speed of $v_0 = 32\,\mathrm{m/s}$, and based on the study conducted in [122] a brittle fracture mainly in mode I is observed. The impact is simulated by imposing on the border nodes between the notches a constant speed of 16.5 m/s in the horizontal direction. The compressive stress waves propagate in the plate and cracks start propagating at the notches' tips but do not grow parallel to them. Crack propagation instead occurs at an angle of approximately 68° with respect to the direction of the notch. Full peridynamic models [36], [125] already showed to be able to reproduce this angle accurately. In the present study, for the sake of verification, the mechanical parameters and the loading condition are taken to be the same as in [36]; which are: $E = 190\,\mathrm{GPa}$, $\rho = 8000\ \mathrm{kg/m^3}$, $\nu = 0.25$ (plane stress conditions are assumed), and $G_0 = 6.9\times10^4\ \mathrm{J/m^2}$. The impact loading is imposed by applying an initial velocity of $v_0 = 16.5\,\mathrm{m/s}$. We keep this velocity

constant as it is very logical to assume in such a short time the projectile and the plate move together. The considered grid spacing is $\Delta x = 0.0005\text{m}$, and the total number of nodes is 80802 nodes. A time duration of 90 μs for the problem is considered, and hence by taking Δt=20 ns the simulation is discretized in 4500 time steps. In addition, here we assume $\chi = 0.8$.

Figure 5.18 shows the grid nodes applied to the proposed coupling method at the beginning of the simulation.

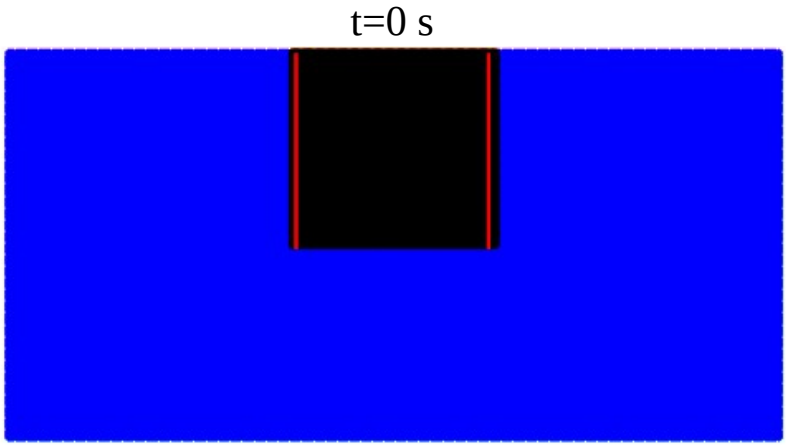

Figure 5.18. Domain discretization at t=0 s in Example III.

As can be seen the peridynamic nodes are initially positioned around the cracked areas as well as places exposed to the impact. At this stage, the domain is discretized by 70096 FPM nodes and 10706 peridynamic nodes. In this example, the adaptive partitioning of the solution domain is carried out. Similar to the former example, the temporal evolutions of damage as well as the partitioning of the solution domain in six snap-shots are reported in Figure 5.19. At the end of the simulation only 4,477 node have been changed to peridynamic nodes and thus a partition of solution domain as shown in Figure 5.19(f) is obtained; it contains 66667 FPM nodes and 14135 peridynamic nodes.

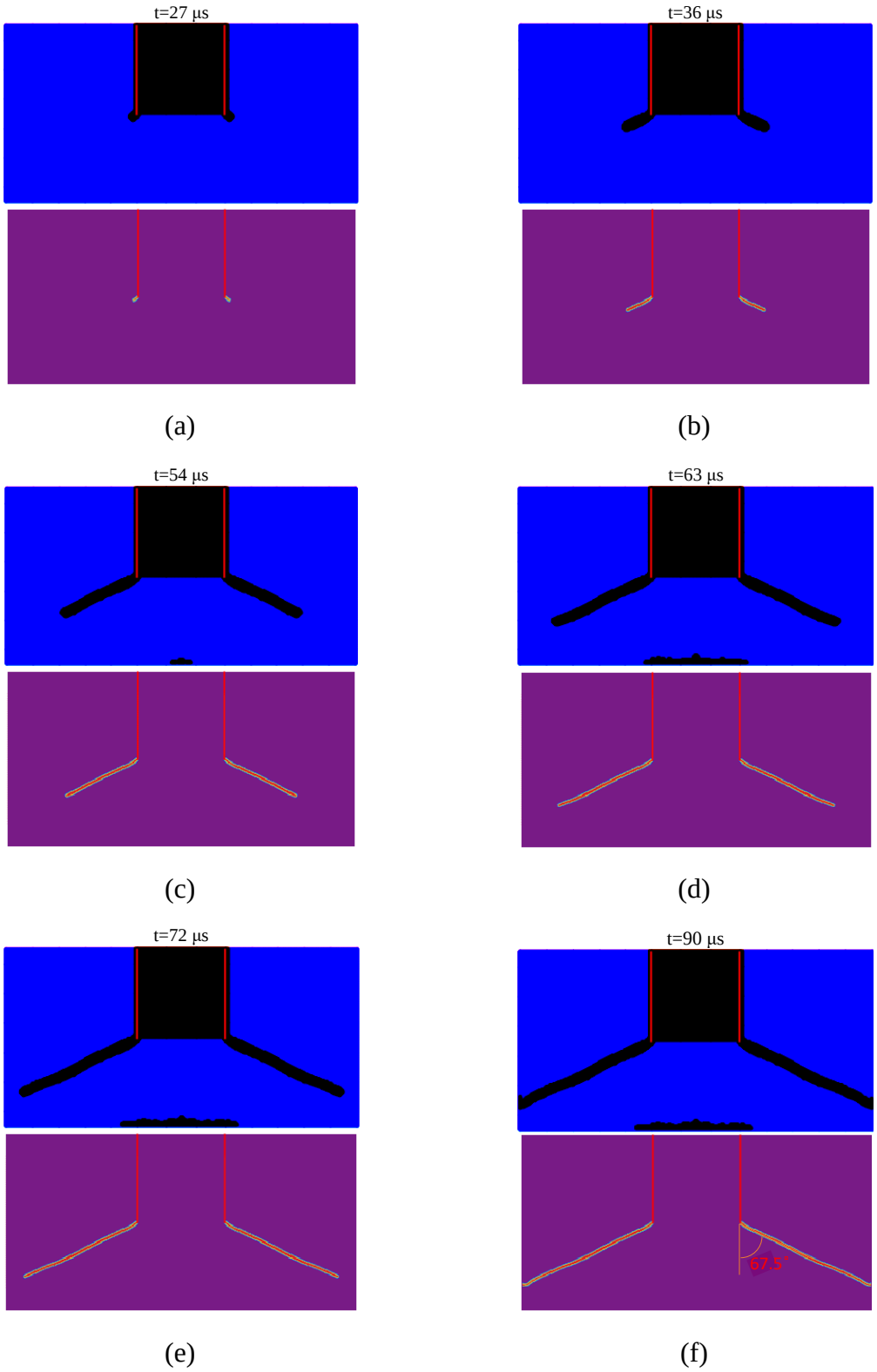

Figure 5.19. Six snap-shots showing the evolution of damage as well as the adaptive partitioning in Example III.

From the last step of the simulation one can conclude that only a small portion of 17.5% is allocated to peridynamic nodes which contributes to a significant computation cost-reduction considering the solution of the same problem with a peridynamic-only model. As shown in Figure 5.19(f) the obtained crack path inclination angle is 67.5° which is in a good agreement with the result of experiment [122].

6. Conclusions

In the present dissertation, a comprehensive study on the coupling of a discretized bond-based peridynamic model with a meshless method based on the classical continuum theory is studied. The main goal is a considerable reduction in the use of computational resources, with respect to using a peridynamic-only model. Moreover, coupling helps to circumvent some important issues in peridynamics; for instance, the surface effect, and the imposition of boundary conditions. The work has been thoroughly explained in the former chapters. In fact, Chapters 1 and 2 have been devoted respectively to the literature review and an overview of the bond-based peridynamic formulation as well as its discretization. The main contribution of the work originates from the works presented in Chapters 3 - 5. The following conclusions can be made for each chapter:

- ***Chapter 3***:

  We have coupled a discretized form of the nonlocal bond-based peridynamics to the method of Meshless Local Exponential Basis Functions (MLEBF), which is based on classical continuum mechanics. The coupling has been achieved by using a simple switching technique in a completely meshless scheme. The proposed approach benefits from the full advantages of both methods while avoiding some of their disadvantages. The performance of the proposed method has been examined comprehensively, and we have shown that:

  - The coupling is achieved in such a way that no appreciable ghost forces are found in the transition zone.

- The coupling scheme is devised in a way that all the peridynamic nodes close to the transition zone have their complete neighborhood and hence the transition part does not suffer from the well-known softening effect.
- The coupling is performed simply so that neither any blending function nor any morphing strategy is required to glue the methods and hence the method is free of introducing any numerical artifact as well as tuning of parameters.
- The presented examples show that the boundary conditions can be imposed in a simple way, and moreover, the method exhibits accurate and stable results in the solution of problems involving singularities such as stationary crack tips.

- ***Chapter 4***:

  In this chapter, the meshless finite point method (FPM) has been extended and applied to elastodynamic problems. The time integration has been performed through an explicit velocity–Verlet approach. A simple technique has been introduced to satisfy Neumann type boundary conditions (tractions) in time. This technique preserves the originality and advantages of the FPM in terms of simplicity and efficiency of the approach. The system of equations has been formed so that the major parts of the solution domain are governed by uncoupled equations; only for a layer of nodes close to Neumann boundaries the equations become coupled. The detailed formulation for advancing in time has been presented, and the accuracy of the approach via several numerical examples, including some 3D problems, has been investigated. The method is capable of yielding proper results with an excellent agreement with those of reference solutions.

Chapter 5:

The formulation developed in Chapters 3 and 4 paved the road to introduce a new meshless computational technique which is suitable for dynamic fracture analysis of brittle materials. In this chapter, we have demonstrated that the switching technique is also workable in the case of dynamic problems. In this way, we coupled the discretized peridynamic model with FPM to benefit from full advantages of both the numerical techniques together. In this chapter, we have shown that the switching technique is capable of being used in an adaptive way so that the application of the nonlocal model can be restricted only to necessary parts of the solution domain where crack is likely to nucleate or propagate. Moreover, to optimize the computational cost as much as possible we introduced a way to change the partitioning of the solution domain during the simulation. In this way, FPM nodes can be easily changed to peridynamic nodes, in the necessary cases, through which the nonlocal region follows the crack morphology. In the numerical examples we have shown that the coupled approach can obtain with good accuracy the results of a peridynamic-only model, while we use a much coarser grid of nodes in the coupled method.

6.1 Future works

It must be pointed out that several future works can be carried out following the outcomes of the present study. Some of them are listed as:

- Extension of the work to 3D problems.
- Dealing with 3D examples entails an efficient and robust software implementation of the code. At this aim some preliminary studies, about parallel implementation

of a peridynamic code on graphic accelerators [126], have been conducted by the authors. However, parallel implementation of the present coupled approach requires a comprehensive study, separately.

- Inspired by the work of this dissertation, the authors have so far developed a new coupling approach to couple a discretized peridynamic model with FEM [45], [127], [128]. The investigations show that all the aforementioned positive features hold in the case of coupling with FEM, as well. However, extending the work to the case of adaptive partitioning of the solution domain is still an open issue.
- In the present study, the coupling approach is developed on the basis of same grid spacing which can be a restriction when application of the work to multiscale problems is sought. To this end, at the moment, inspired by the works in [128], the authors are working to remove this limitation using a fine grid of nodes for the Peridynamic part, while using a coarse grid for the rest.
- Finally our coupling approach can be used as well to have a completely peridynamic model with variable grid size, in a way similar to the one suggested in [69]. This could provide the possibility to develop a multiscale peridynamic approach which is currently being investigated by the author.

REFERENCES

[1] K. Ravi-Chandar, *Dynamic fracture*. Oxford: Elsevier, 2004.

[2] A. A. Griffith, "The phenomena of rupture and flow in solids," *Philos. Trans. R. Soc. london. Ser. A, Contain. Pap. a Math. or Phys. character*, vol. 221, pp. 163–198, 1921.

[3] P. A. Wawrzynek and A. R. Ingraffea, "An interactive approach to local remeshing around a propagating crack," *Finite Elem. Anal. Des.*, vol. 5, no. 1, pp. 87–96, 1989.

[4] L. G. Olson, G. C. Georgiou, and W. W. Schultz, "An efficient finite element method for treating singularities in Laplace's equation," *J. Comput. Phys.*, vol. 96, no. 2, pp. 391–410, 1991.

[5] G. R. Liu, *Mesh Free Methods: Moving Beyond the Finite Element Method*. USA CRC Press: Taylor & Francis, 2010.

[6] B. N. Rao and S. Rahman, "An efficient meshless method for fracture analysis of cracks," *Comput. Mech.*, vol. 26, no. 4, pp. 398–408, 2000.

[7] W. Ai and C. E. Augarde, "An adaptive cracking particle method for 2D crack propagation," *Int. J. Numer. Methods Eng.*, 2016.

[8] H. Gun, "Isotropic damage analysis of frictional contact problems using quadratic meshless boundary element method," *Int. J. Mech. Sci.*, vol. 80, pp. 102–108, Mar. 2014.

[9] F. Mossaiby, M. Bazrpach, and A. Shojaei, "Extending the method of exponential basis functions to problems with singularities," *Eng. Comput. (Swansea, Wales)*, vol. 32, no. 2, pp. 406–423, 2015.

[10] D. S. Dugdale, "Yielding of steel sheets containing slits," *J. Mech. Phys. Solids*, vol. 8, no. 2, pp. 100–104, 1960.

[11] G. I. Barenblatt, "The mathematical theory of equilibrium cracks in brittle fracture," *Adv. Appl. Mech.*, vol. 7, pp. 55–129, 1962.

[12] G. T. Camacho and M. Ortiz, "Adaptive Lagrangian modelling of ballistic penetration of metallic targets," *Comput. Methods Appl. Mech. Eng.*, vol. 142, no. 3–4, pp. 269–301, 1997.

[13] X.-P. Xu and A. Needleman, "Numerical simulations of dynamic crack growth along an interface," *Int. J. Fract.*, vol. 74, no. 4, pp. 289–324, 1996.

[14] P. A. Klein, J. W. Foulk, E. P. Chen, S. A. Wimmer, and H. J. Gao, "Physics-based modeling of brittle fracture: cohesive formulations and the application of meshfree methods," *Theor. Appl. Fract. Mech.*, vol. 37, no. 1, pp. 99–166, 2001.

[15] T. Belytschko and T. Black, "Elastic crack growth in finite elements with minimal remeshing," *Int. J. Numer. Methods Eng.*, vol. 45, no. 5, pp. 601–620, 1999.

[16] T. Belytschko, H. Chen, J. Xu, and G. Zi, "Dynamic crack propagation based on loss of hyperbolicity and a new discontinuous enrichment," *Int. J. Numer. Methods Eng.*, vol. 58, no. 12, pp. 1873–1905, Nov. 2003.

[17] C. L. Richardson, J. Hegemann, E. Sifakis, J. Hellrung, and J. M. Teran, "An XFEM method for modeling geometrically elaborate crack propagation in brittle materials," *Int. J. Numer. Methods Eng.*, vol. 88, no. 10, pp. 1042–1065, 2011.

[18] M. Baydoun and T. P. Fries, "Crack propagation criteria in three dimensions using the XFEM and an explicit--implicit crack description," *Int. J. Fract.*, vol. 178, no.

1, pp. 51–70, Nov. 2012.
[19] G. A. Francfort and J.-J. Marigo, “Revisiting brittle fracture as an energy minimization problem,” *J. Mech. Phys. Solids*, vol. 46, no. 8, pp. 1319–1342, 1998.
[20] P. Roy, A. Pathrikar, S. P. Deepu, and D. Roy, “Peridynamics damage model through phase field theory,” *Int. J. Mech. Sci.*, vol. 128, no. Supplement C, pp. 181–193, 2017.
[21] E. Schlangen and J. G. M. Van Mier, “Simple lattice model for numerical simulation of fracture of concrete materials and structures,” *Mater. Struct.*, vol. 25, no. 9, pp. 534–542, 1992.
[22] W. T. Ashurst and W. G. Hoover, “Microscopic fracture studies in the two-dimensional triangular lattice,” *Phys. Rev. B*, vol. 14, no. 4, p. 1465, 1976.
[23] F. F. Abraham, D. Brodbeck, R. A. Rafey, and W. E. Rudge, “Instability dynamics of fracture: a computer simulation investigation,” *Phys. Rev. Lett.*, vol. 73, no. 2, p. 272, 1994.
[24] F. F. Abraham, D. Brodbeck, W. E. Rudge, and X. Xu, “A molecular dynamics investigation of rapid fracture mechanics,” *J. Mech. Phys. Solids*, vol. 45, no. 9, pp. 15951607–16051619, 1997.
[25] P. Vashishta, R. K. Kalia, and A. Nakano, “Multimillion atom molecular dynamics simulations of nanostructures on parallel computers,” *J. Nanoparticle Res.*, vol. 5, no. 1–2, pp. 119–135, 2003.
[26] A. Sharma, R. K. Kalia, A. Nakano, and P. Vashishta, “Large multidimensional data visualization for materials science,” *Comput. Sci. Eng.*, vol. 5, no. 2, pp. 26–33, 2003.
[27] K. Kadau, T. C. Germann, and P. S. Lomdahl, “Large-scale molecular-dynamics simulation of 19 billion particles,” *Int. J. Mod. Phys. C*, vol. 15, no. 1, pp. 193–201, 2004.
[28] B. N. Cox, H. Gao, D. Gross, and D. Rittel, “Modern topics and challenges in dynamic fracture,” *J. Mech. Phys. Solids*, vol. 53, no. 3, pp. 565–596, 2005.
[29] S. A. Silling, “Reformulation of elasticity theory for discontinuities and long-range forces,” *J. Mech. Phys. Solids*, vol. 48, no. 1, pp. 175–209, Jan. 2000.
[30] S. A. Silling, M. Epton, O. Weckner, J. Xu, and E. Askari, “Peridynamic states and constitutive modeling,” *J. Elast.*, vol. 88, no. 2, pp. 151–184, 2007.
[31] F. Bobaru and W. Hu, “The meaning, selection, and use of the peridynamic horizon and its relation to crack branching in brittle materials,” *Int. J. Fract.*, vol. 176, no. 2, pp. 215–222, 2012.
[32] S. A. Silling and E. Askari, “A meshfree method based on the peridynamic model of solid mechanics,” *Comput. Struct.*, vol. 83, no. 17–18, pp. 1526–1535, Jun. 2005.
[33] Y. D. Ha and F. Bobaru, “Studies of dynamic crack propagation and crack branching with peridynamics,” *Int. J. Fract.*, vol. 162, no. 1–2, pp. 229–244, 2010.
[34] Y. D. Ha and F. Bobaru, “Characteristics of dynamic brittle fracture captured with peridynamics,” *Eng. Fract. Mech.*, vol. 78, no. 6, pp. 1156–1168, 2011.
[35] D. Dipasquale, G. Sarego, M. Zaccariotto, and U. Galvanetto, “Dependence of crack paths on the orientation of regular 2D peridynamic grids,” *Eng. Fract. Mech.*, vol. 160, pp. 248–263, Mar. 2016.

[36] D. Dipasquale, M. Zaccariotto, and U. Galvanetto, “Crack propagation with adaptive grid refinement in 2D peridynamics,” *Int. J. Fract.*, vol. 190, no. 1–2, pp. 1–22, Oct. 2014.

[37] M. Zaccariotto, F. Luongo, G. Sarego, and U. Galvanetto, “Examples of applications of the peridynamic theory to the solution of static equilibrium problems,” *Aeronaut. J.*, vol. 119, no. 1216, pp. 677–700, 2015.

[38] G. Sarego, Q. V Le, F. Bobaru, M. Zaccariotto, and U. Galvanetto, “Linearized State-based Peridynamics for 2D problems,” *Int. J. Numer. Methods Eng.*, vol. 108, no. 10, pp. 1174–1197, 2016.

[39] D. Huang, G. Lu, and P. Qiao, “An improved peridynamic approach for quasi-static elastic deformation and brittle fracture analysis,” *Int. J. Mech. Sci.*, vol. 94–95, pp. 111–122, 2015.

[40] E. Madenci, K. Colavito, and N. Phan, “Peridynamics for unguided crack growth prediction under mixed-mode loading,” *Eng. Fract. Mech.*, pp. 1–11, 2015.

[41] M.-Y. Moon, J.-H. Kim, Y. D. Ha, and S. Cho, “Adjoint design sensitivity analysis of dynamic crack propagation using peridynamic theory,” *Struct. Multidiscip. Optim.*, vol. 51, no. 3, pp. 585–598, 2014.

[42] B. Kilic, A. Agwai, and E. Madenci, “Peridynamic theory for progressive damage prediction in center-cracked composite laminates,” *Compos. Struct.*, vol. 90, no. 2, pp. 141–151, 2009.

[43] S. A. Silling and R. B. Lehoucq, “Peridynamic theory of solid mechanics,” *Adv. Appl. Mech.*, vol. 44, no. 1, pp. 73–166, 2010.

[44] J. O’Grady and J. Foster, “A meshfree method for bending and failure in non-ordinary peridynamic shells,” *Comput. Mech.*, vol. 57, no. 6, pp. 921–929, Jun. 2016.

[45] M. Zaccariotto, T. Mudric, D. Tomasi, A. Shojaei, and U. Galvanetto, “Coupling of FEM meshes with Peridynamic grids,” *Comput. Methods Appl. Mech. Eng.*, vol. 330, 2018.

[46] E. Madenci and E. Oterkus, *Peridynamic theory and its applications*. New York: Springer, 2014.

[47] J. Lee, S. E. Oh, and J.-W. Hong, “Parallel programming of a peridynamics code coupled with finite element method,” *Int. J. Fract.*, Jun. 2016.

[48] F. Han and G. Lubineau, “Coupling of nonlocal and local continuum models by the Arlequin approach,” *Int. J. Numer. Methods Eng.*, vol. 89, no. 6, pp. 671–685, 2012.

[49] P. Seleson, S. Beneddine, and S. Prudhomme, “A force-based coupling scheme for peridynamics and classical elasticity,” *Comput. Mater. Sci.*, vol. 66, pp. 34–49, 2013.

[50] P. Seleson, Y. D. Ha, and S. Beneddine, “Concurrent coupling of bond-based peridynamics and the Navier equation of classical elasticity by blending,” *J. Multiscale Comput. Eng.*, vol. 13, no. 2, pp. 91–113, 2015.

[51] G. Lubineau, Y. Azdoud, F. Han, C. Rey, and A. Askari, “A morphing strategy to couple non-local to local continuum mechanics,” *J. Mech. Phys. Solids*, vol. 60, no. 6, pp. 1088–1102, 2012.

[52] Y. Azdoud, F. Han, and G. Lubineau, “The morphing method as a flexible tool for adaptive local/non-local simulation of static fracture,” *Comput. Mech.*, vol. 54, no.

3, pp. 711–722, 2014.
[53] A. Agwai, I. Guven, and E. Madenci, “Damage prediction for electronic package drop test using finite element method and peridynamic theory,” in *Electronic Components and Technology Conference, 2009. ECTC 2009. 59th*, 2009, pp. 565–569.
[54] R. W. Macek and S. A. Silling, “Peridynamics via finite element analysis,” *Finite Elem. Anal. Des.*, vol. 43, no. 15, pp. 1169–1178, Nov. 2007.
[55] W. Liu and J.-W. Hong, “A coupling approach of discretized peridynamics with finite element method,” *Comput. Methods Appl. Mech. Eng.*, vol. 245–246, pp. 163–175, Oct. 2012.
[56] F. Bobaru and Y. D. Ha, “Adaptive refinement and multiscale modeling in 2D peridynamics,” *Int. J. Multiscale Comput. Eng.*, vol. 9, no. 6, pp. 635–659, 2011.
[57] F. Bobaru, M. Yang, L. F. Alves, S. A. Silling, E. Askari, and J. Xu, “Convergence, adaptive refinement, and scaling in 1D peridynamics,” *Int. J. Numer. Methods Eng.*, vol. 77, no. 6, pp. 852–877, 2009.
[58] B. Ren, H. Fan, G. L. Bergel, R. A. Regueiro, X. Lai, and S. Li, “A peridynamics–SPH coupling approach to simulate soil fragmentation induced by shock waves,” *Comput. Mech.*, vol. 55, no. 2, pp. 287–302, Dec. 2014.
[59] H. Fan, G. L. Bergel, and S. Li, “A hybrid peridynamics-SPH simulation of soil fragmentation by blast loads of buried explosive,” *Int. J. Impact Eng.*, vol. 87, pp. 14–27, 2016.
[60] E. Madenci and S. Oterkus, “Ordinary state-based peridynamics for plastic deformation according to von Mises yield criteria with isotropic hardening,” *J. Mech. Phys. Solids*, vol. 86, pp. 192–219, 2016.
[61] M. A. Bessa, J. T. Foster, T. Belytschko, and W. K. Liu, “A meshfree unification: reproducing kernel peridynamics,” *Comput. Mech.*, vol. 53, no. 6, pp. 1251–1264, Jun. 2014.
[62] W. K. Liu, S. Jun, and Y. F. Zhang, “Reproducing kernel particle methods,” *Int. J. Numer. Methods Fluids*, vol. 20, no. 8–9, pp. 1081–1106, Apr. 1995.
[63] W.-K. Liu, S. Li, and T. Belytschko, “Moving least-square reproducing kernel methods (I) Methodology and convergence,” *Comput. Methods Appl. Mech. Eng.*, vol. 143, no. 1–2, pp. 113–154, Apr. 1997.
[64] T. Rabczuk, S. P. Xiao, and M. Sauer, “Coupling of mesh-free methods with finite elements: basic concepts and test results,” *Commun. Numer. Methods Eng.*, vol. 22, no. 10, pp. 1031–1065, 2006.
[65] E. Erkmen and M. A. Bradford, “Coupling of finite element and meshfree methods for locking-free analysis of shear-deformable beams and plates,” *Eng. Comput.*, vol. 28, no. 8, pp. 1003–1027, Nov. 2011.
[66] H. De’an, L. Chunhan, X. YiHua, and H. Xu, “Analysis of explosion in concrete by axisymmetric FE-SPH adaptive coupling method,” *Eng. Comput.*, vol. 31, no. 4, pp. 758–774, May 2014.
[67] A. Shojaei, B. Boroomand, and F. Mossaiby, “A simple meshless method for challenging engineering problems,” *Eng. Comput.*, vol. 32, no. 6, pp. 1567–1600, Aug. 2015.
[68] E. Oñate, F. Perazzo, and J. Miquel, “A finite point method for elasticity problems,” *Comput. Struct.*, vol. 79, no. 22–25, pp. 2151–2163, Sep. 2001.

[69] S. Silling, D. Littlewood, and P. Seleson, “Variable horizon in a peridynamic medium,” *J. Mech. Mater. Struct.*, vol. 10, no. 5, pp. 591–612, 2015.
[70] E. Emmrich and O. Weckner, “The peridynamic equation and its spatial discretisation,” *Math. Model. Anal.*, vol. 12, no. 1, pp. 17–27, 2007.
[71] K. Yu, X. J. Xin, and K. B. Lease, “A new adaptive integration method for the peridynamic theory,” *Model. Simul. Mater. Sci. Eng.*, vol. 19, no. 4, p. 45003, 2011.
[72] M. L. Parks, S. J. Plimpton, R. B. Lehoucq, and S. A. Silling, “Peridynamics with LAMMPS: A user guide,” *Sandia Natl. Lab. Report, SAND2008-0135, Albuquerque, New Mex.*, 2008.
[73] L. Verlet, “Computer‘ experiments’ on classical fluids. I. Thermodynamical properties of Lennard-Jones molecules,” *Phys. Rev.*, vol. 159, no. 1, p. 98, 1967.
[74] D. J. Littlewood, “Roadmap for peridynamic software implementation,” *SAND Report, Sandia Natl. Lab. Albuquerque, NM Livermore, CA*, 2015.
[75] B. Kilic and E. Madenci, “Coupling of peridynamic theory and the finite element method,” *J. Mech. Mater. Struct.*, vol. 5, no. 5, pp. 707–733, 2010.
[76] A. Shojaei, B. Boroomand, and E. Soleimanifar, “A meshless method for unbounded acoustic problems,” *J. Acoust. Soc. Am.*, vol. 139, no. 5, pp. 2613–2623, May 2016.
[77] E. Soleimanifar, B. Boroomand, and F. Mossaiby, “A meshless method using local exponential basis functions with weak continuity up to a desired order,” *Comput. Mech.*, vol. 53, no. 6, pp. 1355–1374, Feb. 2014.
[78] B. Boroomand, S. Soghrati, and B. Movahedian, “Exponential basis functions in solution of static and time harmonic elastic problems in a meshless style,” *Int. J. Numer. Methods Eng.*, vol. 81, pp. 971–1018, 2010.
[79] J. T. Chen, C. S. Wu, Y. T. Lee, and K. H. Chen, “On the equivalence of the Trefftz method and method of fundamental solutions for Laplace and biharmonic equations,” *Comput. Math. with Appl.*, vol. 53, no. 6, pp. 851–879, Mar. 2007.
[80] B. Movahedian, B. Boroomand, and S. Soghrati, “A Trefftz method in space and time using exponential basis functions: Application to direct and inverse heat conduction problems,” *Eng. Anal. Bound. Elem.*, vol. 37, no. 5, pp. 868–883, May 2013.
[81] B. Movahedian and B. Boroomand, “Non-Fourier Heat Conduction Problems and the Use of Exponential Basis Functions,” *Numer. Heat Transf. Part A Appl.*, vol. 67, no. 3, pp. 357–379, 2015.
[82] S. H. Hashemi, B. Boroomand, and B. Movahedian, “Exponential basis functions in space and time: A meshless method for 2D time dependent problems,” *J. Comput. Phys.*, vol. 241, pp. 526–545, May 2013.
[83] S. M. Zandi, B. Boroomand, and S. Soghrati, “Exponential basis functions in solution of incompressible fluid problems with moving free surfaces,” *J. Comput. Phys.*, vol. 231, no. 2, pp. 505–527, Jan. 2012.
[84] M. Shahbazi, B. Boroomand, and S. Soghrati, “A mesh-free method using exponential basis functions for laminates modeled by CLPT, FSDT and TSDT – Part I: Formulation,” *Compos. Struct.*, vol. 93, no. 12, pp. 3112–3119, Nov. 2011.
[85] R. Abdollahi and B. Boroomand, “Nonlocal elasticity defined by Eringen’s integral model: Introduction of a boundary layer method,” *Int. J. Solids Struct.*,

vol. 51, no. 9, pp. 1758–1780, 2014.
[86] B. Movahedian and B. Boroomand, “The solution of initial-boundary value problems with non-local boundary conditions using exponential basis functions,” *Appl. Math. Model.*, Oct. 2015.
[87] B. Boroomand, S. Bazazzadeh, and S. M. Zandi, “On the use of Laplace’s equation for pressure and a mesh-free method for 3D simulation of nonlinear sloshing in tanks,” *Ocean Eng.*, vol. 122, pp. 54–67, Aug. 2016.
[88] F. Mossaiby, M. Ghaderian, and R. Rossi, “Implementation of a generalized exponential basis functions method for linear and non-linear problems,” *Int. J. Numer. Methods Eng.*, vol. 105, no. 3, pp. 221–240, Aug. 2016.
[89] S. Oterkus, E. Madenci, and A. Agwai, “Fully coupled peridynamic thermomechanics,” *J. Mech. Phys. Solids*, vol. 64, pp. 1–23, 2014.
[90] Q. V Le and F. Bobaru, “Surface corrections for peridynamic models in elasticity and fracture,” *Comput. Mech.*, p. DOI: https://doi.org/10.1007/s0046, Aug. 2017.
[91] F. Bobaru, J. T. Foster, P. H. Geubelle, and S. A. Silling, *Handbook of Peridynamic Modeling*. CRC Press, 2016.
[92] X. Gu, Q. Zhang, and X. Xia, “Voronoi-based peridynamics and cracking analysis with adaptive refinement,” *Int. J. Numer. Methods Eng.*, p. DOI: 10.1002/nme.5596, 2017.
[93] Y. Ferhat and I. Ozkol, “The Effects of Dimension Ratio and Horizon Length in the Micropolar Peridynamic Model,” *Engineering*, vol. 3, no. 6, pp. 594–601, 2011.
[94] Z. Cheng, G. Zhang, Y. Wang, and F. Bobaru, “A peridynamic model for dynamic fracture in functionally graded materials,” *Compos. Struct.*, vol. 133, pp. 529–546, 2015.
[95] M. L. Parks, R. B. Lehoucq, S. J. Plimpton, and S. A. Silling, “Implementing peridynamics within a molecular dynamics code,” *Comput. Phys. Commun.*, vol. 179, no. 11, pp. 777–783, 2008.
[96] P. D. Seleson, “Peridynamic multiscale models for the mechanics of materials: constitutive relations, upscaling from atomistic systems, and interface problems,” The Florida State University, 2010.
[97] S. Mohammadi, *Extended finite element method: for fracture analysis of structures*. John Wiley & Sons, 2008.
[98] T. Belytschko, Y. Y. Lu, and L. Gu, “Element-free Galerkin methods,” *Int. J. Numer. Methods Eng.*, vol. 37, no. 2, pp. 229–256, Jan. 1994.
[99] E. Oñate, S. Idelsohn, O. C. Zienkiewicz, and R. L. Taylor, “A finite point method in computational mechanics. Applications to convective transport and fluid flow,” *Int. J. Numer. Methods Eng.*, vol. 39, no. 22, pp. 3839–3866, Nov. 1996.
[100] J. Bajko, L. Čermák, and M. Jícha, “High order finite point method for the solution to the sound propagation problems,” *Comput. Methods Appl. Mech. Eng.*, vol. 280, pp. 157–175, 2014.
[101] B. Boroomand, M. Najjar, and E. Oñate, “The generalized finite point method,” *Comput. Mech.*, vol. 44, no. 2, pp. 173–190, Jul. 2009.
[102] J. Fang and A. Parriaux, “A regularized Lagrangian finite point method for the simulation of incompressible viscous flows,” *J. Comput. Phys.*, vol. 227, no. 20, pp. 8894–8908, Oct. 2008.

[103] P.-W. Hsieh, Y. Shih, and S.-Y. Yang, “A Tailored Finite Point Method for Solving Steady MHD Duct Flow Problems with Boundary Layers,” *Commun. Comput. Phys.*, vol. 10, no. 1, pp. 161–182, Jul. 2011.
[104] E. Ortega, E. Oñate, and S. Idelsohn, “An improved finite point method for tridimensional potential flows,” *Comput. Mech.*, vol. 40, no. 6, pp. 949–963, Aug. 2007.
[105] M. Tatari, M. Kamranian, and M. Dehghan, “The finite point method for the p-Laplace equation,” *Comput. Mech.*, vol. 48, no. 6, pp. 689–697, Dec. 2011.
[106] N.-J. Wu, B. S. Chen, and T.-K. Tsay, “A Review on the Modified Finite Point Method,” *Math. Probl. Eng.*, vol. 2014, pp. 1–29, 2014.
[107] A. Sadeghirad and S. Mohammadi, “Equilibrium on line method (ELM) for imposition of Neumann boundary conditions in the finite point method (FPM),” *Int. J. Numer. Methods Eng.*, vol. 69, no. 1, pp. 60–86, Jan. 2007.
[108] X. Zhang, K. Z. Song, M. W. Lu, and X. Liu, “Meshless methods based on collocation with radial basis functions,” *Comput. Mech.*, vol. 26, no. 4, pp. 333–343, 2000.
[109] T. J. Liszka, C. A. M. Duarte, and W. W. Tworzydlo, “hp-Meshless cloud method,” *Comput. Methods Appl. Mech. Eng.*, vol. 139, no. 1–4, pp. 263–288, 1996.
[110] E. Oñate, “Derivation of stabilized equations for numerical solution of advective-diffusive transport and fluid flow problems,” *Comput. Methods Appl. Mech. Eng.*, vol. 151, no. 1–2, pp. 233–265, Jan. 1998.
[111] B. Boroomand, A. A. Tabatabaei, and E. Oñate, “Simple modifications for stabilization of the finite point method,” *Int. J. Numer. Methods Eng.*, vol. 63, no. 3, pp. 351–379, May 2005.
[112] C. Shu, H. Ding, and K. S. Yeo, “Local radial basis function-based differential quadrature method and its application to solve two-dimensional incompressible Navier--Stokes equations,” *Comput. Methods Appl. Mech. Eng.*, vol. 192, no. 7, pp. 941–954, 2003.
[113] A. La Rocca and H. Power, “A double boundary collocation Hermitian approach for the solution of steady state convection--diffusion problems,” *Comput. Math. with Appl.*, vol. 55, no. 9, pp. 1950–1960, 2008.
[114] G. R. Liu and Y. T. Gu, “A meshfree method: meshfree weak--strong (MWS) form method, for 2-D solids,” *Comput. Mech.*, vol. 33, no. 1, pp. 2–14, 2003.
[115] G. R. Liu, Y. L. Wu, and H. Ding, “Meshfree weak--strong (MWS) form method and its application to incompressible flow problems,” *Int. J. Numer. Methods Fluids*, vol. 46, no. 10, pp. 1025–1047, 2004.
[116] A. Sadeghirad and I. M. Kani, “Modified equilibrium on line method for imposition of Neumann boundary conditions in meshless collocation methods,” *Int. j. numer. method. biomed. eng.*, vol. 25, no. 2, pp. 147–171, 2009.
[117] D. Mirzaei and K. Hasanpour, “Direct meshless local Petrov-Galerkin method for elastodynamic analysis,” *Acta Mech.*, vol. 227, no. 3, p. 619, 2016.
[118] A. Shojaei, F. Mossaiby, M. Zaccariotto, and U. Galvanetto, “The meshless finite point method for transient elastodynamic problems,” *Acta Mech.*, vol. 228, no. 10, pp. 3581–3593, 2017.
[119] W. Weaver Jr, S. P. Timoshenko, and D. H. Young, *Vibration problems in*

engineering. John Wiley & Sons, 1990.
[120] S. A. Silling, “Reformulation of elasticity theory for discontinuities and long-range forces,” *J. Mech. Phys. Solids*, vol. 48, no. 1, pp. 175–209, Jan. 2000.
[121] R. A. Wildman and G. A. Gazonas, “A finite difference-augmented peridynamics method for reducing wave dispersion,” *Int. J. Fract.*, vol. 190, no. 1–2, pp. 39–52, 2014.
[122] J. F. Kalthoff, “Modes of dynamic shear failure in solids,” *Int. J. Fract.*, vol. 101, no. 1/2, pp. 1–31, 2000.
[123] T. Rabczuk, G. Zi, S. Bordas, and H. Nguyen-Xuan, “A simple and robust three-dimensional cracking-particle method without enrichment,” *Comput. Methods Appl. Mech. Eng.*, vol. 199, no. 37–40, pp. 2437–2455, Aug. 2010.
[124] J.-H. Song, P. M. A. Areias, and T. Belytschko, “A method for dynamic crack and shear band propagation with phantom nodes,” *Int. J. Numer. Methods Eng.*, vol. 67, no. 6, pp. 868–893, Aug. 2006.
[125] H. Ren, X. Zhuang, Y. Cai, and T. Rabczuk, “Dual-horizon peridynamics,” *Int. J. Numer. Methods Eng.*, 2016.
[126] F. Mossaiby, A. Shojaei, M. Zaccariotto, and U. Galvanetto, “OpenCL implementation of a high performance 3D Peridynamic model on graphics accelerators,” *Comput. Math. with Appl.*, vol. 74, no. 8, pp. 1856–1870, 2017.
[127] U. Galvanetto, T. Mudric, A. Shojaei, and M. Zaccariotto, “An effective way to couple FEM meshes and Peridynamics grids for the solution of static equilibrium problems,” *Mech. Res. Commun.*, vol. 76, pp. 41–47, Sep. 2016.
[128] M. Zaccariotto, D. Tomasi, and U. Galvanetto, “An enhanced coupling of PD grids to FE meshes,” *Mech. Res. Commun.*, vol. 84, no. Supplement C, pp. 125–135, 2017.

APPENDIX A

In the case where the particular solution of Eq (3.14) is not a-priori known, it can be approximated locally within C_i through a series of exponential basis functions as:

$$\mathbf{u}^p \cong \sum_{k=1}^{b^p} \mathbf{c}_k'^p \exp(\alpha_l^p x + \beta_l^p y) = \begin{pmatrix} c_k'^{px} \\ c_k'^{py} \end{pmatrix} \exp(\alpha_l^p x + \beta_l^p y) \tag{A.1}$$

where $\mathbf{c}_k'^p$ is a vector containing unknown constant coefficients, and b^p stands for the number of bases.

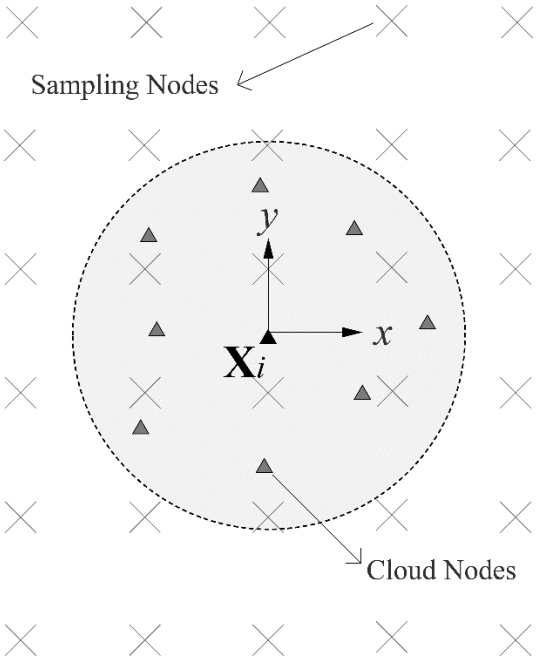

Figure A.1. $\mathbf{X}^G$ grid of sampling nodes for the local approximation of the particular solution

The introduction of the above expression into Eq (3.1) should satisfy the non-homogenous part of Eq (3.1), and we have:

$$\sum_{k=1}^{b^p} \begin{bmatrix} D_1(\alpha_l^p)^2 + D_3(\beta_l^p)^2 & (D_2 + D_3)\alpha_l^p \beta_l^p \\ (D_2 + D_3)\alpha_l^p \beta_l^p & D_3(\alpha_l^p)^2 + D_3(\beta_l^p)^2 \end{bmatrix} \begin{pmatrix} c_k'^{px} \\ c_k'^{py} \end{pmatrix} \exp(\alpha_l^p x + \beta_l^p y) = -\begin{pmatrix} b_x \\ b_y \end{pmatrix} \tag{A.2}$$

The go further with the local approximation, a local grid of nodes $\mathbf{x}^G$, so called sampling nodes as shown in Figure A.1, is needed. Equation (A.2) should be collected at $\mathbf{x}^G$ which results in:

$$\mathbf{M}^p \mathbf{c}^P = \mathbf{h}^p \tag{A.3}$$

where $\mathbf{c}^P = (c_1'^{px}, c_1'^{py}, c_2'^{px}, c_2'^{py}, \ldots, c_{b^p}'^{px}, c_{b^p}'^{py})$, and thus the components of $\mathbf{M}^p$ and $\mathbf{h}^p$ are in the following form:

$$\mathbf{M}^P_{jl} = \begin{bmatrix} D_1(\alpha_l^p)^2 + D_3(\beta_l^p)^2 & (D_2 + D_3)\alpha_l^p \beta_l^p \\ (D_2 + D_3)\alpha_l^p \beta_l^p & D_3(\alpha_l^p)^2 + D_3(\beta_l^p)^2 \end{bmatrix} \exp(\alpha_l^p x_j^G + \beta_l^p y_j^G), \tag{A.4}$$

$$j = 1, 2, \ldots, n^G \quad , \quad l = 1, 2, \ldots, b^p$$

and

$$\mathbf{h}_j^p = -\begin{pmatrix} b_x \\ b_y \end{pmatrix}\Big|_{\mathbf{x}_j^G} \tag{A.5}$$

where n^G denotes the number of the sampling grid nodes. In the final analysis, $\mathbf{c}^P$ can be found as follows:

$$\mathbf{c}^P = (\mathbf{M}^p)^+ \mathbf{h}^p \tag{A.6}$$

It should be remarked here that the particular basis functions must not satisfy the homogeneous governing equation expressed in Eq (3.5). Moreover, Eq (A1) is written locally, and one may adopt other collocation approaches to obtain the particular solution. The reader may consult references [77], [78] to get more insight into the details.